Higher-order Sensors for Fast Detection of Gases

A Thesis
Presented to
The Academic Faculty

by

Isao Sasaki

In Partial Fulfillment
of the Requirements for the Degree
Doctor of Philosophy

School of Chemistry and Biochemistry
Georgia Institute of Technology
December 2005

Higher-order Sensors for Fast Detection of Gases

Approved by:

Dr. Jiří Janata
Chemistry & Biochemistry
Georgia Institute of Technology, Adviser

Dr. Boris Mizaikoff
Chemistry & Biochemistry
Georgia Institute of Technology

Dr. Ari Glezer
Mechanical Engineering
Georgia Institute of Technology

Dr. David M. Collard
Chemistry & Biochemistry
Georgia Institute of Technology

Dr. Mira Josowicz
Chemistry & Biochemistry
Georgia Institute of Technology

Date Approved: November 14th, 2005

To my parents,

ACKNOWLEDGEMENTS

My sincerest thanks go to my advisors Professor Jiří Janata and Dr. Mira Josowicz for their support and guidance through my graduate studies.

I am grateful to Professor Ari Glezer (ME) for his guidance and support during the course of integrating the synthetic jet into the chemical sensing system.

I also would like to express my thanks to Professor Boris Mizaikoff and Professor David M. Collard for serving on my thesis advisory committee.

I am really grateful to Mr. Steven Sheffield (Manufacturing Research Center, Georgia Tech) with the design and fabrication of the stereolithographed modules.

I would like to thank Janata research group members for their friendship and support.

The support by the grant of the National Science Foundation (NSF-EN695874 and CHE0452045) is also gratefully acknowledged.

Finally, I would like to express my special thanks to my parents for their patience and support.

TABLE OF CONTENTS

LIST OF TABLES

LIST OF FIGURES

SUMMARY

The long-term goal of this research is to develop an integrated sensor system such as a "sniffphone", which has the functionality similar to the mammalian olfaction system. The system has an array of sensors equipped with a "brain" to process the data from the sensors in order to obtain meaningful information as well as a "nose" to "sniff" (deliver) analyte gases to the sensors. Therefore, a systematic approach to develop the gas sniffing system is required. Thereby the research is divided into two main parts: the sensing part and the gas delivery part.

The reliable chemical information from the chemical sensor requires that the sensitive layer of the sensor exhibits long-term stability. It was found that polyaniline (PANI) cast from formic acid does not satisfy this requirement. To improve the stability of the sensing layer, CSA (camphorsulfonic acid) was added to the formic acid. The introduction of photo-irradiation at 254 nm as an additional treatment to the sensing layer was necessary. The influence of the UV-treatment on the mechanical properties of the film was investigated using impedance analysis with quartz crystal resonator. The mechanical impedance result suggested that the film became more "viscous" after the UV treatment. This result could be explained by rearrangement of the matrix to a more stable morphological structure.

In order to enhance gas selectivity of PANI matrix, metal or metal oxide clusters were incorporated into the matrix by two different methods (Chapter 2). Both the chemFET and the chemiresistor modified with the Hg_2Cl_2*PANI showed sub ppm detection of HCN (Chapter 2). The composite materials of PANI with silver, copper, iron, nickel, palladium and mercury were also prepared. The sensors with the layers were exposed to seven different gases and some response patterns specific to the gases were obtained.

The second part of the thesis discussed the gas delivery system to the sensors implemented using the synthetic jet technology. The gas delivery cell has an oscillating diaphragm

which generates a synthetic jet field continuously impinging on the sensor surface. The main focus in Chapter 3 was to compare the sensor response times with and without the integrated gas sampling functionality. It was shown that the sensor response time became three times faster with jet than the one without jet for gas mixing in a closed system with Cell 02. This result showed that jet actuation was an effective way to mix and deliver gases in a *closed* system. The sniffing functionality was demonstrated using Cell 05 designed for operation in an *open system*. The gas sniffing experiments showed that in the presence of the jet, the response time of the sensor was faster by about two orders of magnitude (20 compared to 1800 seconds).

The jet sampling system was applied to continuous monitoring of ammonia gas filter performance using the chemFET array (Chapter 4). The jet system collected the gas before and after filtering, and the difference between the two responses was compared over time to observe the break-through of the filter. With different amounts of zeolite filter, different onset times of the break-through of the filter were observed. It was therefore concluded that the gas sensing system integrated with the gas sampling functionality could be applied to monitor a gas filter performance.

Cell 05 was designed so that the impinging jet covers the sensing active area of the array of eight chemFETs. The two-dimensional distribution of the ammonia gas concentrations showed that the jet covered the active sensing area in an effective way so that the sampling volume for sensing was significantly reduced compared with the conventional gas flow through cell system (Chapter 4).

Based on these initial studies, the proposed gas sniffing system was shown to be effective in realizing fast detections of gases for critical applications.

CHAPTER I

PHOTO- AND PROTONATION-INDUCED STABILIZATION OF PANI MATRIX

1.1 Introduction

The solution processability of polyaniline (PANI) [1] has made the PANI coating one of the most applied conducting polymers to chemical sensors or actuators. The PANI film in the emeraldine salt form (PANI-ES), the most conductive form in the PANI family [2], showed improved stability by selecting a proper dopant-acid (camphorsulfonic acid [3], 2-acrylamido-2-methyl-1-propanesulfonic acid [3, 4], or dibutyl phosphate [3]). One million electrochemical redox cycles of a PANI-ES film were achieved without degradation for actuator use [4]. This means that even after a number of the oxidation cycles within a certain potential range, the dopant-acid holds its electrochemical activity. This makes PANI, as a matrix for incorporating gas sensitive sites, one of the potentially most promising conducting polymers.

UV [5] as well as other ionizing radiations—electron [6], γ-ray [5–7], and X-ray [8]—has been utilized to modify the electronic properties of PANI in solid form [5,6,8] and in solution form [7] depending on the nature of generated species from solvents [7], environmental gases [6, 8], or co-existing materials [5, 9]. Furthermore, it has been indicated that morphological changes in PANI including molecular chain conformation, intermolecular chain-to-chain configuration, degree of order, etc. have an effect on the electronic properties of the doped form of PANI [10]. We presume that an unstable PANI film behavior comes from unstable dopant-acids, or gradual evaporation of solvents from the cast film [3]. The purpose of the herein applied UV treatment in the presence of the stable dopant-acid, camphorsulfonic acid (CSA), is to improve the long-term stability of the PANI-ES film cast from formic acid by re-arranging the morphological structure of the PANI chains. PANI·CSA films cast from

m-cresol show one of the highest conductivity due to the stronger interaction between the solvent and PANI [11]. However, the slow evaporation of the solvent and high viscosity of the PANI solution represent a problem in solution-processability of this material in chemical sensors. Therefore, PANI·CSA films were cast from formic acid in this study.

The material was cast on the GT02 sensing platform that accommodate both of the chemically sensitive Field Effect Transistor (chemFET) and chemiresistor [12–14]. Since chemFET signal and chemiresistor signal come from the same PANI·CSA film, discrepancy related to film thickness or its morphology is not an issue. A stable chemFET signal comes from the stable charge density or work function [13] of the layer, which is related to chemical inertness to the exposed environment. On the other hand, the stability of a chemiresistor signal is based on the charge density as well as the charge mobility of the film. To elucidate the effects of UV treatment on PANI·CSA films in detail, FT-IR, Uv-vis, and impedance analysis with QC (quartz crystal) resonator were conducted before and after UV irradiation of the film. PANI in the emeraldine base form (PANI-EB) dissolved in formic acid with and without CSA was also characterized before and after UV irradiation.

1.2 Experimental Section

1.2.1 Materials

Formic acid (88 %, Fisher Scientific), ammonium hydroxide solution (29.3 %, Fisher Scientific,), and (1R)-(-)-10-camphorsulfonic acid (Aldrich) were used as received. Prior to using polyaniline emeraldine base, PANI-EB powder (MW ca. 20000, Aldrich), was suspended in ammonium hydroxide solution for 2 hours, filtered, and then cleaned with deionized water followed by methanol [15].

1.2.2 Preparation of PANI in Formic Acid Solution

The filtered and vacuum dried PANI-EB powder at room temperature was used to prepare a stock solution. The solution was made by dissolving 50 mg of the purified PANI-EB powder in 10 mL of formic acid followed by 10 min sonication and overnight stirring in a closed container. All the concentrations of PANI in formic acid solutions reported here are given as the ratio of the weight of the dry PANI powder (mg) to the volume of the

formic acid (mL). For example the concentration of the stock solution is 5 mg/mL.

1.2.3 Preparation of CSA-doped PANI·HCOOH from Formic Acid Solution

The CSA-doped PANI was prepared by adding a certain amount of CSA powder to a portion of the PANI·HCOOH stock solution (ca. 0.1 mL) followed by 10 min sonication. The certain amount of the added CSA was calculated to be always in the ratio of two CSA molecules per four benzene units of the PANI polymer. The concentrations of PANI and CSA in formic acid solutions are expressed by the weight (mg) of dry PANI-EB powder (without CSA) to the volume (mL) of the formic acid solution.

1.2.4 UV Treatment of PANI in Solution Form

A Spectronics ENF-280C ultraviolet hand-held lamp was used for the broad UV light source centered at 254 nm . The UV treatment of PANI dissolved in formic acid solution (with no added CSA) was conducted in a quartz cuvette (the path length is 0.5 or 0.1 cm) for Uv-vis spectroscopic study in solution form. The concentration of the PANI solution for Uv-vis study is 0.08 mg/mL.

1.2.5 UV Treatment of PANI in Film Form

All the PANI films with and without CSA for FT-IR, Uv-vis, and mechanical impedance analysis were spin-cast using 5 mg/mL solutions on silicon substrate (p-type), quartz plate, and quartz crystal (QC) resonator, respectively. For spin-casting a film, a Laurell WS-400-6NPP spin processor was used at 1500 rpm for 10 min unless otherwise mentioned. After spin-casting the PANI·CSA film on a QC resonator, the excess of the film that deposited over the electrode area was removed with a cotton swab soaked in formic acid. The film thickness was measured using a Dektak3ST surface profiler (Sloan/Veeco Instruments, Inc.).

All the PANI·CSA films were drop-cast with a glass capillary (ca. 0.02 mm^3 of 5 mg/mL PANI and CSA solution) onto each sensing module separated by the micro-well [16] photolithographically formed on the sensing platform, GT02. After casting, all the PANI·CSA films were dried at 60 °C for 24 hours under vacuum followed by cooling down period of ca. 3 hours to room temperature before UV treatment to the films. PANI films

without CSA were spin-cast at 200 rpm on silicon substrate and dried at 60 °C overnight without vacuum.

1.2.6 Uv-vis Spectroscopy

Uv-vis spectroscopy measurements were performed on a Shimadzu UV-3101PC spectrometer. Absorption spectra were measured in the wavelength range 190 to 890 nm with a resolution of 2 nm. The background spectrum was recorded in air.

1.2.7 FT-IR Spectroscopy

FT-IR spectra were collected on a BIORAD FTS-6000 spectrometer in the sample compartment or with a BIORAD UMA 500 IR microscope. All the FT-IR spectra of the cast films were measured using bare silicon substrate as a background with a resolution setting of 4 cm^{-1} and an average of 200 scans.

1.2.8 Impedance Analysis with QC (Quartz Crystal) Resonator

QC resonators (10 MHz) and a QC oscillator (35366-10) were purchased from International Crystal Manufacturing. The QC resonators were unpolished AT-cut quartz (with a diameter of 1.37 cm and gold electrodes of 0.51 cm in diameter). The 100 nm thick gold electrodes were deposited on 10 nm thick Ti-adhesion layers. For impedance analyses, a Solartron SI 1260 Impedance/Gain Phase analyzer was used with an AC voltage amplitude of 100 mV. Data fitting was done with the equivalent circuits in ZVIEW (Solartron Instruments, Inc.).

1.2.9 Stability Test for ChemFETs and Chemiresistors

The stability tests of the PANI·CSA coatings were conducted on the GT02 platforms that consist of eight integrated FET structures [14]. The advantage of this platform is the possibility to measure both the work function and the bulk resistance of the same layer [13]. After casting of the PANI film and UV treatment, the sensing platforms were always stored in a dark place at room temperature. The conducted stability test is: UV treatment (90 min at 254 nm) at a distance of ca. 2 cm from the UV lamp, heat treatment in oven (90

min at 100 °C), or no treatment at all (control). The heat treatment was carried out to evaluate the heating effect by the absorbed UV light.

Threshold voltages of chemFETs and resistances of chemiresistors were measured with an HP 4155A Semiconductor Parameter Analyzer. Threshold voltages of chemFETs were obtained by plotting square root of drain-source current versus gate voltage and extrapolating the line to obtain the intercept (threshold voltage) [13]. The drain voltage was scanned from 0 to 7 V. The resistance measurement was conducted on a film cast between two electrodes integrated within the gate area of the FET [13, 14]. The measurement was initiated by scanning voltage across the film from 0 to 1 V (the distance between the two electrodes is 0.15 mm) and calculating the slope of current versus voltage line. The resistance response of a PANI·CSA film cast on the platform during UV treatment was monitored with a constant current of 3.9 μA by measuring the voltage across the two electrodes.

1.3 Results and Discussion

1.3.1 Uv-vis Spectroscopy

Figure 1.1 shows Uv-vis spectra of PANI-EB dissolved in formic acid with (spectra c and d) and without (spectra a and b) CSA. The spectrum (a) is recorded from a solution form and spectrum (b) from as cast film. The spectrum (a) shows that the PANI in the formic acid solution is in the emeraldine salt (ES) state since the polaron band at 1.6 eV (768 nm) and the π-π^* band gap transition at 3.5 eV (350 nm) are observed [17]. On the other hand, the spectrum (b) of the cast PANI film has the π_B-π_Q transition at 2.0 eV (622 nm), and the π-π^* band gap transition at 3.8 eV (324 nm). Comparing the two spectra a and b, the blue shifts of the polaron transition and the band gap transition signalize deprotonation of PANI film to the EB form [17,18]. This implies that formic acid works as protonating agent for the PANI film and it is evaporating from the film after casting the PANI film. When the supporting protonating agent, CSA, is present in the PANI formic acid solution before casting the film, the recorded spectrum (c) does not differ from the cast PANI·CSA film spectrum (d). These results confirm that the cast PANI·CSA film is in the protonated state and agree with the published results of Zagorska et al [3]. Recognizing CSA as one of the

possible proper supporting protonating agents for PANI film that is a stronger acid-dopant than formic acid and has very low volatility, we have examined the long-term stability of the material after UV-irradiation.

In order to elucidate the effects of UV treatment on PANI in solution of formic acid, UV treatment at 254 nm was applied for 0, 4, 7, 9, 12 and 25 minutes of duration. Figure 1.2a shows spectra for PANI formic acid solution (0.08 mg/mL) recorded from A to F for the step-wise increasing UV dose. The formic acid has a strong absorption band at 254 nm as shown in spectrum G (without PANI). It is known that low molecular carboxylic acids with UV light at 254 nm generate free *reducing* radicals [19–21]. During UV-irradiation of the solution, the color changed from green to brown. When the concentration of the PANI solution was diluted down to ca. 0.01 mg/mL, the color changed from light green to transparent. This color change is attributed to the fact that PANI-ES is fully reduced to the leucoemeraldine (PANI-LE) form since the PANI-LE is colorless and sometimes called "white polyaniline" [22, 23]. When the same irradiation experiment was carried out for PANI formic acid solution at 356 nm, the solution color did not change at all. The presence of the weakly developed band with maxima around 3.5 eV (352 nm) and a shoulder at 3.0 eV (416 nm) reveal the transition from the low valence levels to polaron band and as π-π^* band gap of PANI-ES [17, 25]. It is interesting to point out that the recorded spectra from A to F show similarities to the UV spectra recorded during electrochemical reduction of PANI film; the maximum of the polaron band at 1.6 eV (768 nm) rapidly decreases and red-shifts with the increasing UV radiation dose. After 25 minutes of UV irradiation the polaron band almost disappeared [22]. Also the electronic transitions at 3.0 eV (416 nm) and 3.5 eV (352 nm) are decreasing in magnitude with the UV dose. This behavior, as well as the increasing transition peak at 4.4 eV (280 nm) due to the π-π^* bandgap of leucoemeraldine salt (LS) [17], suggests a progressive reduction of PANI to the PANI-LE state with increasing UV dose. Furthermore, the isosbestic point around 350 nm suggests that there are continuous changes in the redox state of the dispersed PANI with UV treatment [2].

Figure 1.2b shows Uv-vis spectra of the PANI·CSA film cast from formic acid, recorded

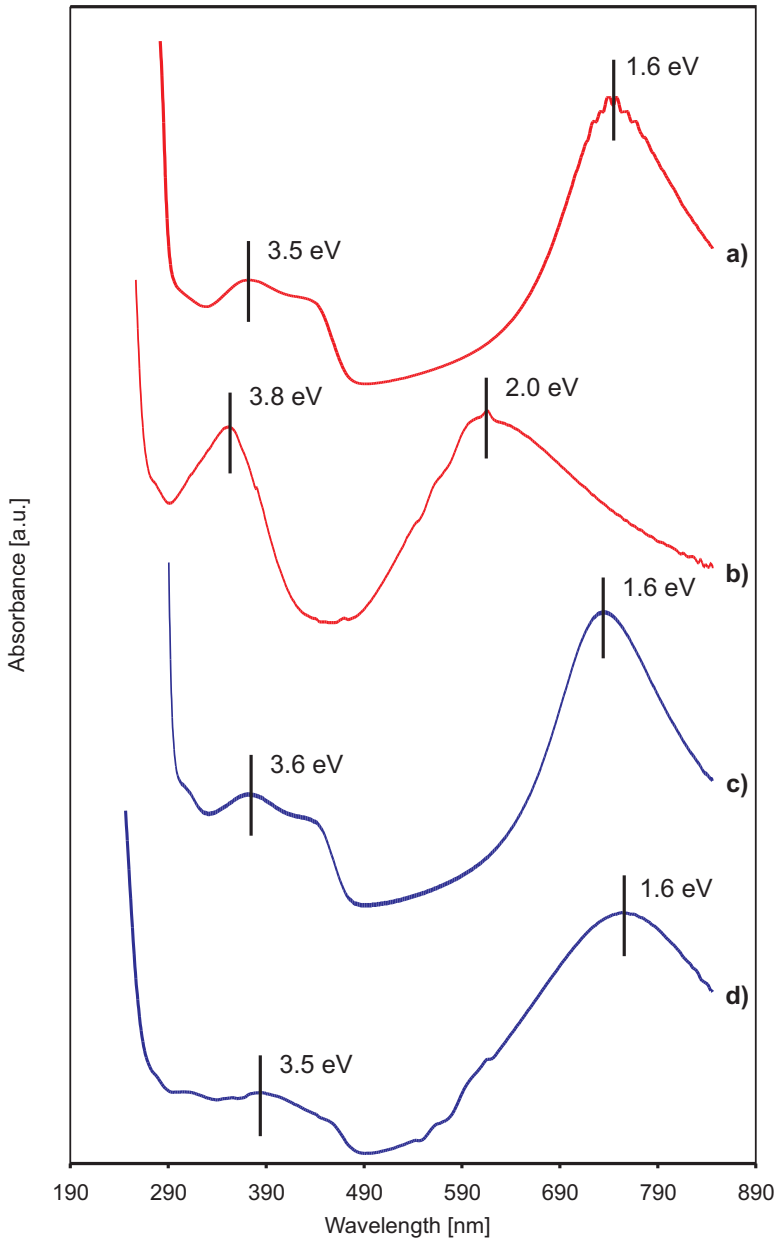

Figure 1.1: Uv-vis spectra of (a) PANI in formic acid solution, (b) PANI film cast from formic acid solution, (c) PANI and CSA in formic acid solution, and (d) PANI·CSA film cast from formic acid solution.

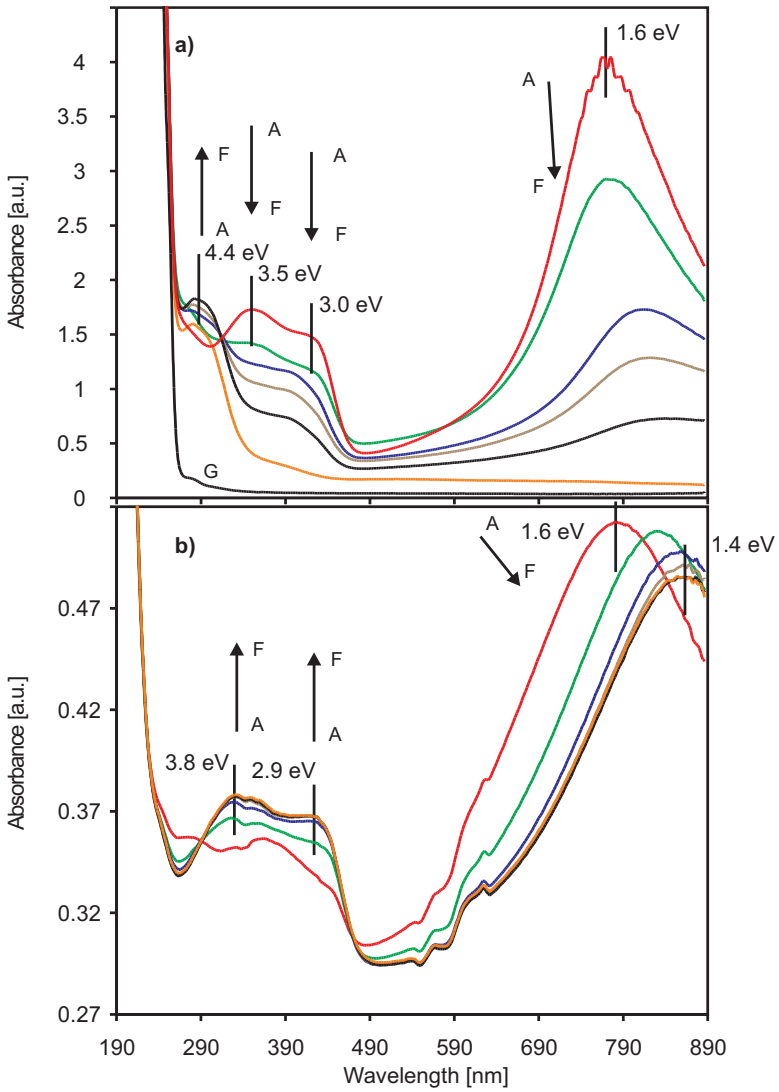

Figure 1.2: (a). Uv-vis spectra of PANI in formic acid solution recorded after UV irradiation at 254 nm for 0, 4, 7, 9, 12, and 25 min (from A to F). Spectrum G is only formic acid for comparison. (b). Uv-vis spectra of PANI·CSA cast film on quartz substrate recorded after 0, 10, 40, 90, 190, and 240 min of UV irradiation (from A to F).

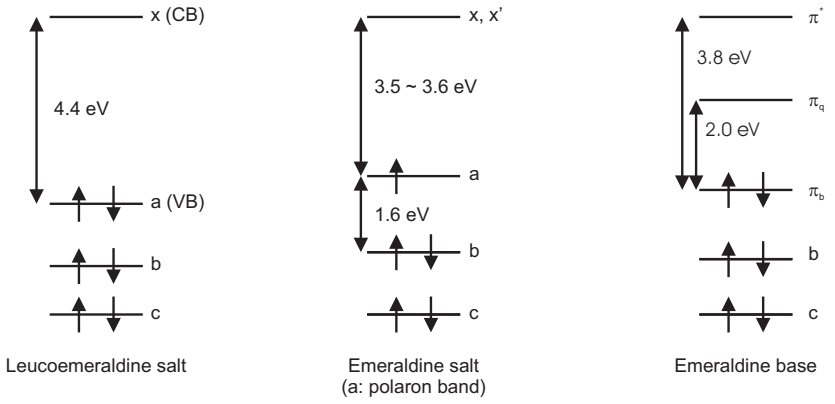

Figure 1.3: Energy level diagrams obtained from the Uv-vis spectra of leucoemeraldine salt, emeraldine salt, and emeraldine base (CB: Conduction Band, VB: Valence Band).

for the UV treatment of 0, 10, 40, 90, 190, to 240 minutes (spectra A to F). The transmittance of the 100 nm thick film was calculated at 254 nm to be 95.7 %. With increasing UV dose, the valence-polaron band at 1.6 eV (760 nm) red shifts to 1.4 eV (870 nm). This behavior indicates an increase of the intraband-free carrier excitations, often discussed in the context of structural re-orientation of the aromatic units, leading to an increased conjugation length of the polymer chain [26]. The electronic transitions at 422 nm (2.9 eV) and at 330 nm (3.8 eV) both increased with UV dose [18,24,25]. That behavior differs from the one shown in Figure 1.2a. The observed isosbestic points (Figure 1.2b) at 290 nm (4.3 eV) and at 470 nm (2.6 eV) confirm the existence of the equilibrium state in the doping-related sub-gap absorptions of PANI·CSA film. The decrease of the polaron band intensity stopped after 90 min and staied constant until 240 min of UV dose. When the already irradiated PANI·CSA film was post-exposed to formic acid vapor, the polaron transition at 1.4 eV showed a small blue shift with no change in absorbance intensity. An additional irradiation with UV light did not cause any further change in the optical spectrum suggesting that the PANI·CSA film attained already a stable proton-doping state. Figure 1.3 shows the energy level diagrams of the leucoemeraldine salt (LS), emeraldine salt (ES), and emeraldine base (EB) obtained from the Uv-vis data in Figures 1.1 and 1.2 (CB: Conduction Band, VB: Valence Band) [18].

1.3.2 FT-IR Spectroscopy

Figure 1.4 and Table 1.1 [27, 28] show the FT-IR spectra of the PANI·CSA film (ca. 100nm thick) exposed to UV (254 nm) after 0, 10, 40, and 90 minutes. With the increasing time of UV irradiation, the slope between 1500 and 3000 cm^{-1} increased. That suggests that the number of the free charge carriers on the polymer backbone *increased* and the film became *more conductive* [5]. Furthermore, it is seen that the band at 780 cm^{-1}, attributed to the vibrational stretch of C-H out of plane bending of 1, 4-ring [29], became larger with irradiation time up to 40 min and disappeared after 90 min. The similar change in the intensity of the band was observed before and after electrochemically cycling a PANI film at the same oxidation state in an inorganic acid solution [30]. In Table 1.1, it is clearly seen that the wavenumber is also changing. We presume that the change in the intensity and the energy of this vibration band is related to morphological changes in the PANI film, e.g., rearrangement of the chains. Note that with increasing UV dose the ratio of the quinoid units (1590cm^{-1}) to benzenoid units (1510 cm^{-1}) is increasing. This result confirms the UV result (Figure 1.2b), and it can be inferred that UV irradiation facilitates the proton transfer from CSA to PANI without any sign of degradation of the polymer.

Table 1.1: FT-IR band assignments of PANI·CSA film cast from formic acid with different UV doses.

Dose [min]	C–H[a]	N=Q=N[b]	C–N[c]	N–B–N[d]	N=Q=N[e]
0	783 cm^{-1}	1165 cm^{-1}	1302 cm^{-1}	1503 cm^{-1}	1601 cm^{-1}
10	770 cm^{-1}	1165 cm^{-1}	1308 cm^{-1}	1503 cm^{-1}	1599 cm^{-1}
40	768 cm^{-1}	1165 cm^{-1}	1308 cm^{-1}	1503 cm^{-1}	1599 cm^{-1}
90	783 cm^{-1}	1167 cm^{-1}	1308 cm^{-1}	1503 cm^{-1}	1599 cm^{-1}

a: C–H out of plane bending on 1,4-ring, b: a mode of N=Q=N, c: C–N stretching, d: stretching of N–B–N, e: stretching of N=Q=N, where Q is quinoid unit and B is benzenoid unit.

To clarify the UV effect on PANI in the presence of formic acid, UV treatment was conducted with PANI without CSA after spin-casting a film on silicon substrate for FT-IR study (Figure 1.5 and Table 1.2 [27, 28]). For comparison, PANI film cast without UV treatment is shown as spectrum (0 min UV dose). The spectra, recorded 10, 40 and 90

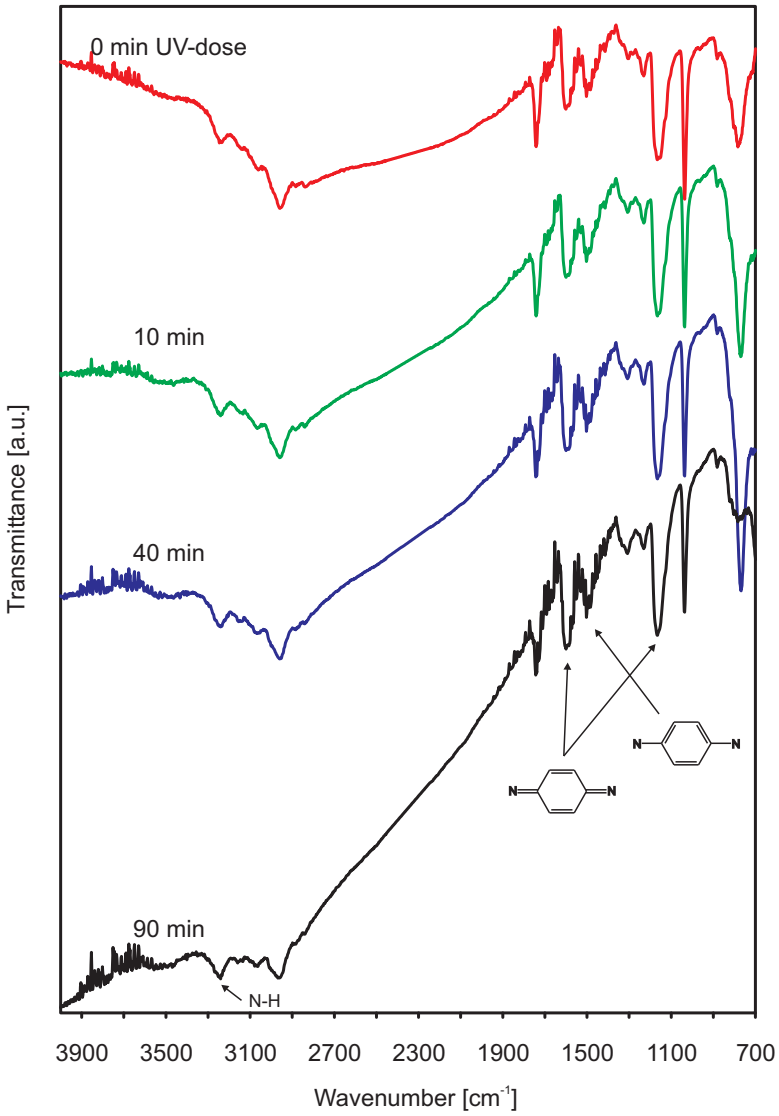

Figure 1.4: FT-IR spectra of PANI·CSA film cast on silicon substrate after 0, 10, 40, and 90 minutes of UV irradiation time.

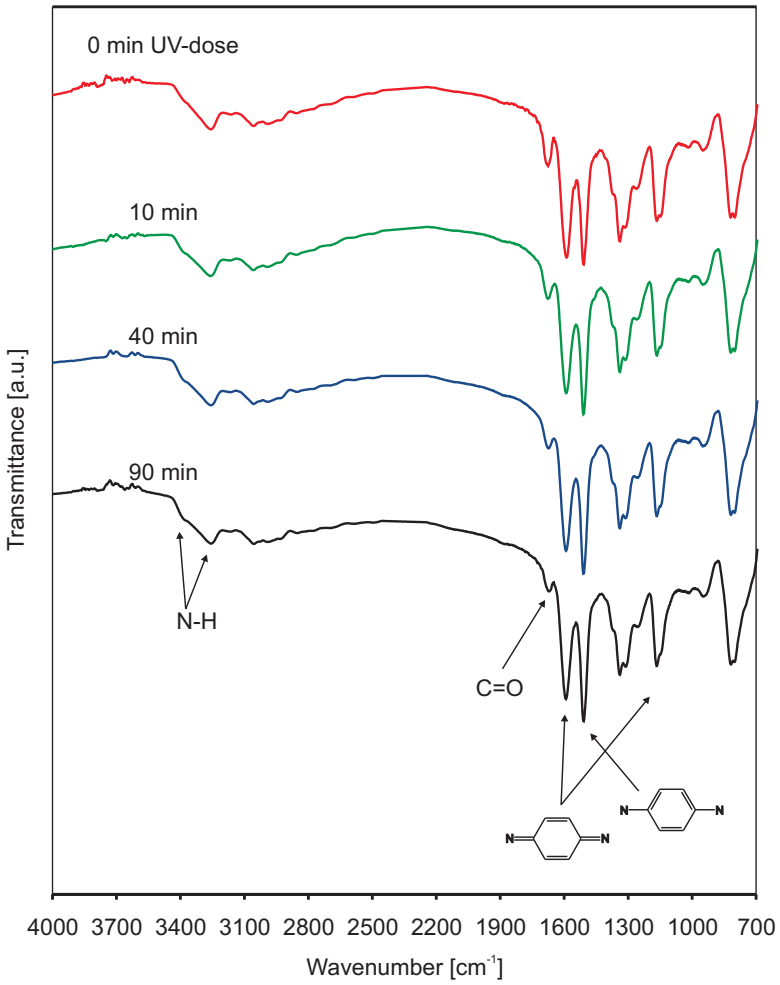

Figure 1.5: FT-IR spectrum of PANI film without CSA cast on silicon after 0, 10, 40 and 90 min UV irradiation time.

minutes after UV irradiation, show that UV treatment causes a decrease of the ratio of the quinoid units (1170 and 1590 cm^{-1} to the benzenoid units (1510 cm^{-1}). That behavior indicates that reduction of PANI takes place [31]. It also agrees with the behavior of the UV irradiated PANI in formic acid solution as already discussed (Figure 1.2a). Furthermore, note that the intensity of the C=O stretch decreases with the applied UV dose most probably due to decomposition of the residual formic acid inside the film to free radicals that then act as reducing agent for the PANI. No change is observed in the transmittance slope between 1500 and 3000 cm^{-1}.

Table 1.2: FT-IR band assignments of PANI film cast from formic acid with different UV doses.

Dose [min]	C–H[a]	N=Q=N[b]	C–N[c]	N–B–N[d]	N=Q=N[e]
0	818 cm^{-1}	1166 cm^{-1}	1339 cm^{-1}	1508 cm^{-1}	1591 cm^{-1}
10	818 cm^{-1}	1165 cm^{-1}	1339 cm^{-1}	1510 cm^{-1}	1591 cm^{-1}
40	818 cm^{-1}	1165 cm^{-1}	1339 cm^{-1}	1510 cm^{-1}	1591 cm^{-1}
90	820 cm^{-1}	1165 cm^{-1}	1339 cm^{-1}	1508 cm^{-1}	1589 cm^{-1}

a: C–H out of plane bending on 1,4-ring, b: a mode of N=Q=N, c: C–N stretching, d: stretching of N–B–N, e: stretching of N=Q=N, where Q is quinoid unit and B is benzenoid unit.

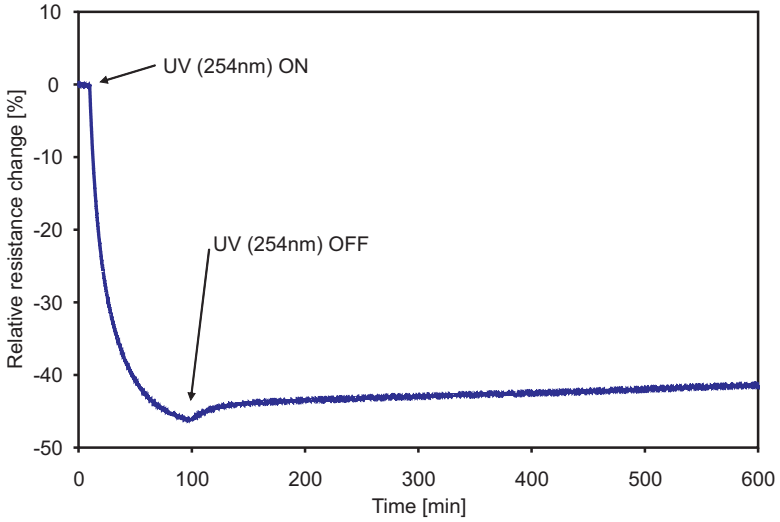

Figure 1.6: Relative change in resistance of PANI·CSA film drop-cast on the sensor device (GT02) during 90 min exposure to the UV.

1.3.3 Resistance Response of PANI·CSA Film During UV Treatment

Figure 1.6 shows the result of UV-induced change of the resistance of PANI·CSA in film form with 90 min UV treatment. The relative resistance change (the definition is explained below) became smaller with UV light on and was relatively stable over time after the UV light was turned off. The decrease of the relative resistance is in good agreement with the increase of the slope of the FT-IR spectra seen in Figure 1.4.

1.3.4 Impedance Analysis with QC Resonator

A similar experiment of UV exposure was conducted with the PANI·CSA film spin-cast on QC resonator. The UV treatment was done for 90 min at 254 nm. As seen in Figure

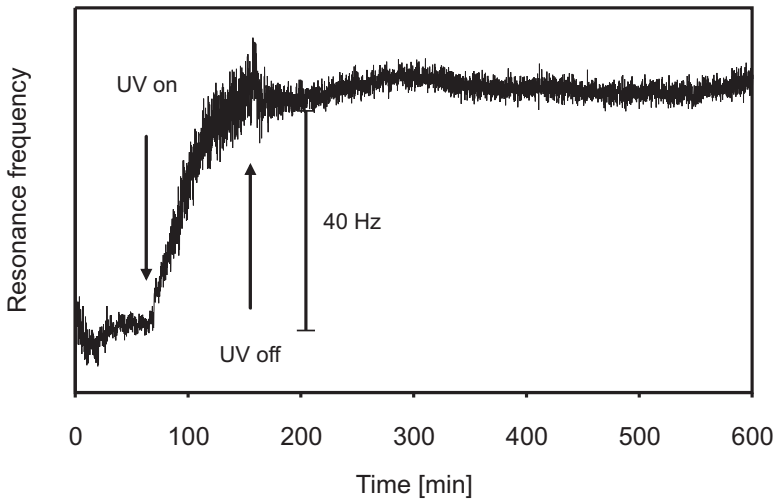

Figure 1.7: Resonance frequency change of PANI·CSA film coated on QC resonator during 90 min UV exposure.

1.7, the resonant frequency *increased* during the UV and stayed relatively constant after the UV. If the residual formic acid exists in the film and the frequency increase is due to the mass decrease of the film, the resonant frequency after the UV may be expected to increase (or decrease) since other gas molecules, most likely water vapor, take the place of the decomposed formic acid molecules. The reason why the frequency did not change can be because the frequency shift results from the mechanical property changes of the film related to the morphological changes. From the frequency shift, it is impossible to clarify the reason for the frequency shift. Therefore impedance analysis of the QC resonator with PANI·CSA film was conducted to investigate the mechanical property changes due to the UV treatment.

For mechanical impedance analysis of the PANI·CSA film coated on QC resonator, a lumped-element equivalent circuit shown in Figure 1.8 was used. In order to evaluate the viscoelastic properties of the film, an analysis of the admittance (Y) of the QC before and after UV treatment was conducted. The equivalent circuit is composed of a static arm (C_0^*) in parallel with a motional arm (L_1, R_1, C_1, L_2 and R_2) [32, 33]. The capacitance in the static arm (C_0^*) originates from the capacitive geometry of QC resonator itself. In the motional arm, L_1, R_1 and C_1 are motional inductance, resistance, and capacitance of the bare (unperturbed) QC resonator, respectively. L_1 and C_1 represent the mass and

mechanical elasticity of the QC. R_1 is the proportional loss of energy. L_2 and R_2 represent the motional inductance and resistance of the cast PANI·CSA film, respectively. When the QC is not coated with the film, those impedance values are zero. The complex element for QC in the motional arm (Z_Q), the complex element of the cast PANI·CSA in the motional arm (Z_F), and the admittance of the equivalent circuit shown in Figure 1.8 (Y) are:

$$Z_Q = L_1\omega j + R_1 + 1/C_1\omega j \tag{1.1}$$

$$Z_F = L_2\omega j + R_2 \tag{1.2}$$

$$Y = C_0^*\omega j + 1/(Z_Q + Z_F) \tag{1.3}$$

where ω is the angular frequency.

The data of impedance analysis are shown as changes in the magnitude of admittance (Figure 1.9a) and the phase angle (Figure 1.9b). As seen in Figure 1.9a, the maximum of admittance showed a shift to a higher resonant frequency after UV treatment as well as a decrease of the peak height (damping). The shift in the resonant frequency comes from a change in mass, whereas, the damping results from the energy loss of oscillation. The results of the data fitting are shown in Table 1.3. The obtained impedance values of the bare QC resonator are similar to the ones reported elsewhere [34] except for the R_1 value, which is also affected by the QC mounting to the QC holder. For data fitting to obtain the mechanical impedance of the film (L_2 and R_2) before and after UV treatment, all the other values related to the bare QC (C_0^*, L_1, R_1, and C_1) were assumed to be constant after casting the film and UV treatment as indicated by the # mark in Table 1.3. The R_2 value of the film increased after UV treatment due to the change in the film viscoelasticity; that is, the film became more viscous presumably due to an increase of intermolecular interaction of the polymer. The L_2 value of the film shows only a small increase presumably due to the mass decrease, caused by the decomposition of the residual formic acid molecules inside the film, suggesting that even after the intensive drying process of the PANI·CSA films (at 100 °C for 24 h under vacuum), there are some residual formic acid molecules inside the

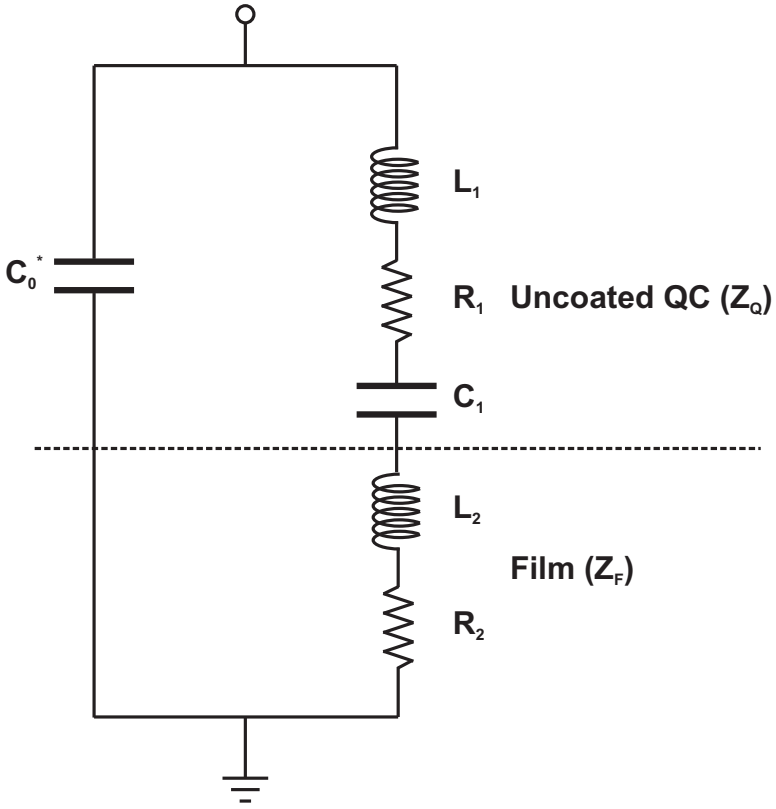

Figure 1.8: Lumped-element equivalent circuit used to represent the near resonant impedance responses of QC resonator coated with PANI·CSA film. C_0^* is the sum of the static and parasitic capacitances. L_1, R_1, and C_1 are the bare QC resonator motional inductance, resistance, and capacitance, respectively. L_2 and R_2 are for the PANI·CSA film.

film. If the residual formic acid exists and keeps evaporating into the air, it would cause the baseline drift of the sensor signal over time. From the resonant frequency shift of the film cast from the PANI and CSA solution in formic acid, the density of the film was determined to be ca. 1.4 g/cm^3 from the Sauerbrey equation [35].

Table 1.3: Results of Impedance Analysis of QC resonator.

	C_0^* [pF]	L_1 [mH]	R_1 [Ω]	C_1 [fF]	L_2 [mH]	R_2 [Ω]
Uncoated QC	6.763	9.185	16.73	27.58	0	0
Before UV treatment	6.763#	9.185#	16.73#	27.58#	0.0059	0.79
After UV treatment	6.763#	9.185#	16.73#	27.58#	0.0058	3.28

Suggests that the values were assumed to be constant after casting the PANI·CSA film and 90 min UV treatment.

To elucidate UV effects in more detail on the film mechanical properties, the results of the impedance analysis were used to obtain the change in the complex shear modulus (G):

$$G = G' + jG" \tag{1.4}$$

where G' (storage modulus) is the real part related to the layer elasticity, and G" (loss modulus) is the imaginary part related to the layer viscosity [33]. The UV treatment changed the R_2 value from 0.79 to 3.28. That R_2 change is a function of G and the film thickness [36]. In order to obtain the G values, for simplicity of calculations, the film thickness was assumed to be constant using the following equation [32, 33, 36]:

$$Z_F = \frac{N\pi}{4K^2\omega_0 C_0^*} tanh\Big(j\omega h_f \sqrt{\frac{\rho_f}{G}}\Big) \sqrt{\frac{G\rho_f}{\mu_q \rho_q}} \tag{1.5}$$

where N is the mode of oscillation (1), K^2 is the square of the quartz electromechanical coupling coefficient (7.74 x 10^{-3}), ω_0 is the resonant frequency (rad/s), C_0^* is the static capacitance of the resonator (6.763 x 10^{-12} F), ω is the angular frequency (rad/s), ρ_q is the shear stiffness of the quartz (2.947 x 10^{10} N/m^2), h_f is the film thickness (1 x 10^{-7} m), ρ_f is the density of the layer (1.4 x 10^3 kg/m^3), ρ_q is the density of the quartz (2.651 x 10^3 kg/m^3), and j^2 = -1. The calculated shear moduli are $10^{4.19}$ + $10^{1.13}$j Pa (before

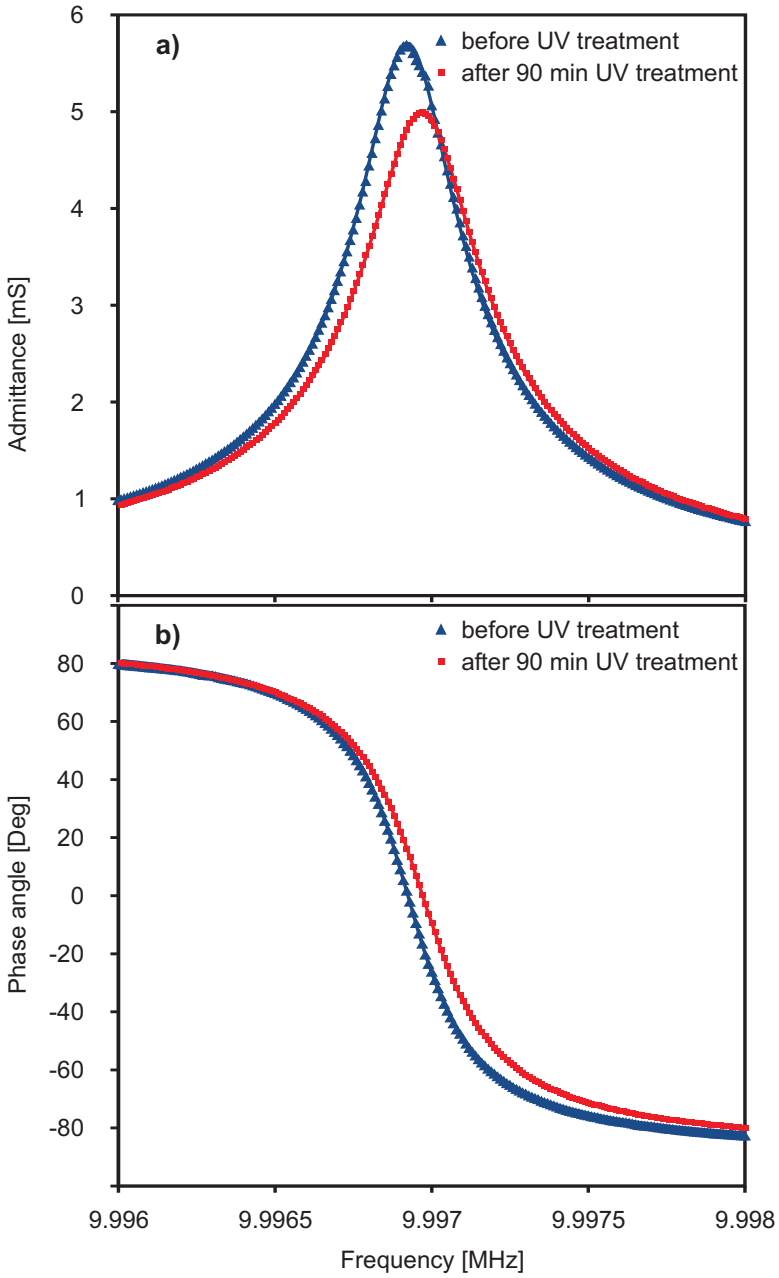

Figure 1.9: (a). Admittance and (b) phase angle of QC resonator coated with PANI·CSA film before (▲), and after 90 min of UV treatment (■). The lines are calculated from the equivalent circuit model in Figure 1.8.

UV) and $10^{4.19}$ + $10^{1.75}$j Pa (after UV). The real part did not change but the imaginary part *increased* after UV treatment. The increase of the G" suggests that the PANI·CSA film became more viscous presumably due to the increased intermolecular π-π interactions caused by the morphological re-arrangement.

1.3.5 Long-term Physical Properties of PANI·CSA using ChemFETs and Chemiresistors

The long-term stability of chemFETs and chemiresistors coated with PANI·CSA film are compared as a function of post-treatment: UV treatment, heat treatment or no additional treatment after casting (Figures 1.10a and 1.10b). The changes of the threshold voltage and the resistance in Figures 1.6 and 1.10 are shown as a relative percent change, Xrel:

$$X_{rel} = \frac{(X_{meas} - X_0)}{X_0} \times 100 \quad [\%] \tag{1.6}$$

where X_0 is the initial value of the resistance (R), or the threshold voltage (V_T), measured before the UV or the heat treatment. The average values of the initial V_T and R are ca. 1.3 V and 780 Ω, respectively. The data in Figure 1.10a shows that the V_T values of all three treatments increase with storage time independently, and remain relatively stable after 70 days. It has been observed that electrochemically induced relaxation of PANI films is slow due to the slow morphological changes and exhibits continuous relaxation up to 900 h [37]. It is also seen that the relative threshold voltage change of the UV treated chemFET is improved (ca. 7 % after 70 days.) compared to the heat and no treatments (ca. 12 %). The changes in the relative resistance of the PANI·CSA chemiresistor in Figure 1.10b, on the other hand, show that the UV treatment stabilizes the relative change significantly as compared to the heat treatment or no treatment at all.

It is important to point out that the total resistance of the film is a combination of the bulk resistance and interface resistances between the film and the device, and between the film and air. In most cases, the bulk resistance is dominant over the interface resistances. The stability of the threshold voltage, on the other hand, is based on the charge distribution in the film at the interface between the film and the device surface. Therefore, the stabilities

of those two transduction principles originate from different parts of the film: bulk of the film (chemiresistor) and interface between the film and the sensor device (chemFET). More precisely, the threshold voltage is governed by the charge distribution in the space charge region, which is about 500 nm thick from the interface [38]. If the UV light penetrates the film deep enough to reach the upper part of the space charge region but not enough to reach the bottom part, the improvement of the chemiresistor stability can be greater than the one of the chemFET stability.

To estimate the penetration depth of the UV light, the film thickness on the sensor devices was calculated using the density of the film (1.4 g/cm^3), dispensed volume of the PANI and CSA solution (0.02 mm^3), solution concentration including the weight of CSA (11.4 mg/mL), and surface area of the device (0.4 x 0.5 mm). The film thickness and the transmittance were calculated to be ca. 1 x 10^3 nm and ca. 64 %, respectively. If reproducible threshold voltages among chemFETs are required, the thickness of the film needs to be thicker than the space charge region [38]. Consequently, the optimum film thickness may range between 500 and 1000 nm to obtain reproducible threshold voltages as well as to increase the transmittance of the UV light.

The change in the G" value after UV treatment suggests that the PANI·CSA film became mechanically more viscous, which might support that the PANI·CSA film underwent morphological changes in the PANI structure. It is possible that the morphological changes increased the intermolecular $\pi - \pi$ interactions and stabilized the charge mobility, especially the intermolecular charge carrier hopping, therefore the distances between the polymer chains become fixed over time.

In Figure 1.10b is seen, that an improvement of the resistance with heat treatment as compared to the film without any treatment can be also achieved. However, the relative change in resistance immediately after the heat treatment increased , presumably due to the loss of the absorbed water inside the film [39, 40]. That is opposite to the UV treated film. Based on these results, one can say that the UV treatment stabilizes the resistance of the PANI·CSA matrix in a different way than the heat treatment.

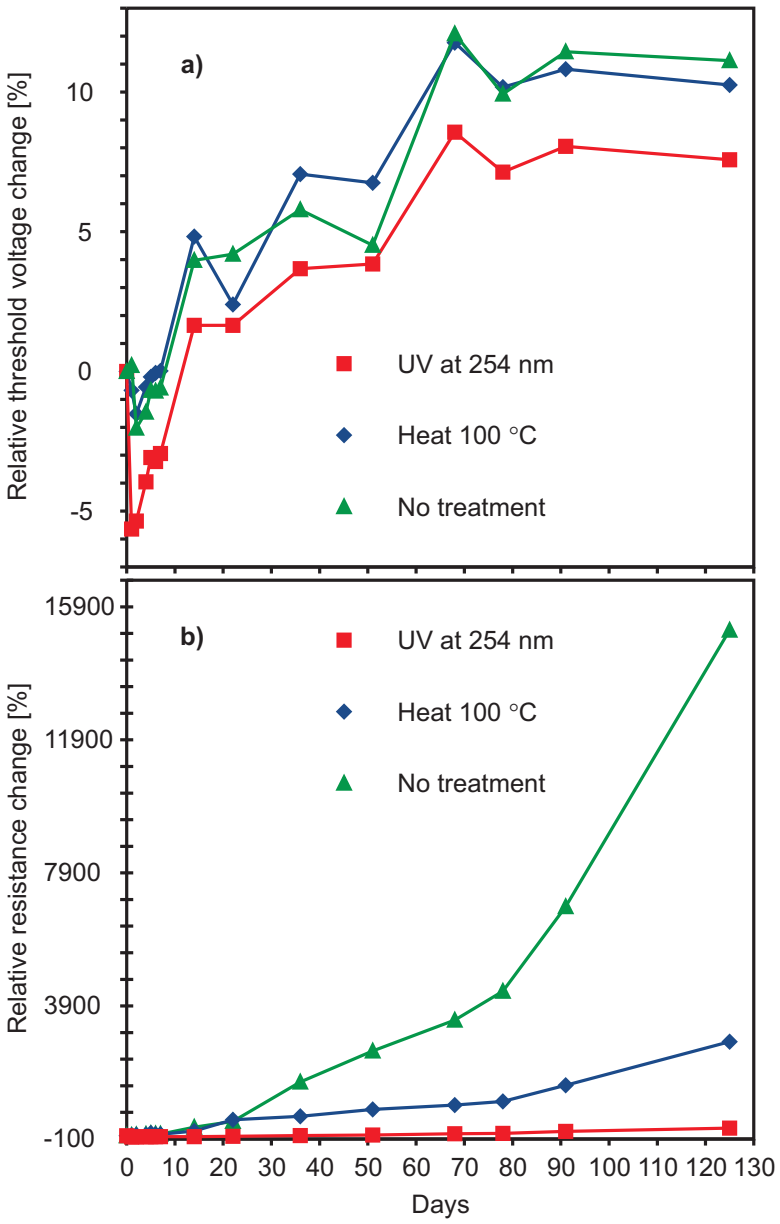

Figure 1.10: Long-term stability of chemFETs (a) and chemiresistors (b) with 90 min UV treatment at 254 nm (■), heat treatment at 100 °C for 90 min (♦), and no treatment (control) (▲). The y-axes are shown as a relative percent change with respect to the initial value measured before the treatments. The initial average values of threshold voltage and resistance are ca. 1.3 V and 780 Ω, respectively.

1.4 Conclusions

This chapter has shown that the UV treatment of PANI·CSA films at 254 nm improved significantly the long-term stability of the chemiresistor as compared to the film without post-treatment. On the other hand, the chemFETs after UV treatment showed an improvement by 7 % as compared to the other treatments. The difference in the long-term stability behavior of the chemiresistor and the chemFET sensors is due to the different transduction principles.

CHAPTER II

INCORPORATION OF BINDING SITES IN PANI MATRIX FOR GAS SENSING

2.1 Introduction

PANI films [41, 42] (Chapters 3 and 4) and fibers [42–44] in the polyaniline emeraldine salt (PANI-ES) form have been used for ammonia gas detection. The non-conducting form without dopant acid (PANI-EB) has also been used for HCl gas sensors [42,43]. In addition, to achieve versatile selectivities to other gases, metal/metal oxide clusters were introduced into the PANI matrix [41, 45–47]. The aim of this chapter is to investigate the best way to incorporate metal/metal oxide clusters as sensitive sites into the PANI matrix. Figure 2.1 shows the molecular design of a composite film of selective binding sites and PANI film, (metal/metal oxide)*PANI. In this case, the analyte gas is expected to be an electron donor but can also be an electron acceptor. The electron donor or acceptor behavior depends on the electron affinity of the composite film [12, 48]. The gas sensor signal results from this partial charge transfer between the analyte gas and the cluster and subsequent change in the work function of the PANI film, which can be detected by chemFET and/or chemiresistor.

There are several ways to accomplish incorporation of the metal clusters into the PANI matrix (Figure 2.2) [47].

1. **Adding metal salts into the PANI casting solution.**

   Mechanically mix the salt into the PANI casting solution and then casting a film. However, due to the limited solubility of the salts in the casting solution, the grain size of the additives may become difficult to control. It is also possible to electrochemically reduce the salt to the metal clusters.

2. **Reduction of metal salts using the activated PANI film.**

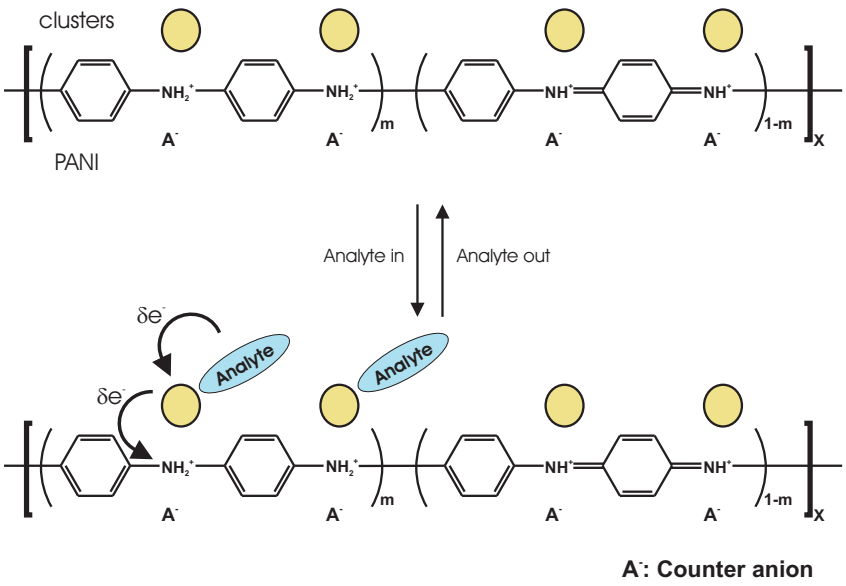

Figure 2.1: Schematic of clusters in PANI matrix and the gas sensing mechanism. When the analyte forms a charge transfer complex with the clusters, for example, flow of partial charge (δe^-) into the molecular PANI backbone takes place. Consequently the work function of the overall matrix changes leading to generation of an analytical signal measured by chemFET and chemiresistor.

It has been shown that an electrochemically activated PANI film acts as an electron donor [38, 47, 49]. When transferred into metal ion solution, the film is able to reduce the ion due to its slow relaxation related to the conformational changes of the polymer. As a result, a composite material of PANI with metal/metal oxide clusters is formed.

3. **Electrochemically induced clusters.**

   The metal clusters can also be incorporated electrochemically into the priori cast PANI film on the device. During the electrochemical cycling of the film, the soluble form of metal ions present in solution is reduced into the metal on the PANI. The advantage of this method over the last two is that it is possible to calculate the number of moles of the cluster from the total charge used for the reduction process.

This chapter mainly deals with the first and second methods to incorporate clusters into PANI matrix. In the previous study, PANI and mercurous chloride composite film (Hg_2Cl_2*PANI) was shown to be sensitive to HCN gas down to sub-ppm levels with a Kelvin probe [38] and suspended gate FET [49]. The sensing mechanism is as follows [38]:

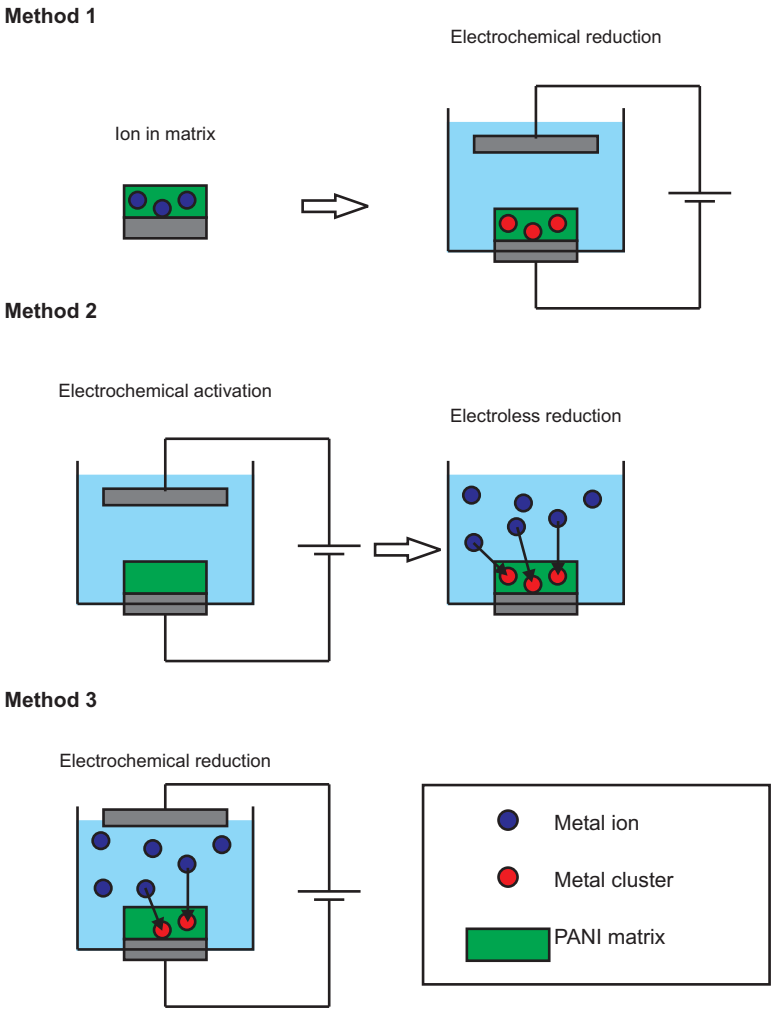

Figure 2.2: Three different methods to form metal/metal oxide clusters and PANI composite film.

$$HCN(g) + Hg_2Cl_2 * PANI \longleftrightarrow HCN * Hg_2Cl_2 * PANI \tag{2.1}$$

The partial charge transfer between the sorbed HCN molecule and the Hg_2Cl_2 cluster results in the change of the work function and the conductivity of the PANI matrix. Based on these previous studies, the first part of this chapter focuses on HCN gas sensors using Hg_2Cl_2*PANI composite film using Method 1. PANI and $HgCl_2$ mixture was used to drop-cast films for the sensing layers of chemFETs and chemiresistors. The salt was then electrochemically reduced into insoluble Hg_2Cl_2 for HCN sensing.

By the second method, six different clusters were introduced. After electrochemical activation of the cast PANI·CSA film in acid solution by applying constant cathodic potential, the matrix is transferred into an acid solution containing metal ion for cluster deposition [38, 41]. The metal ions are reduced due to the slow relaxation of the PANI film. The prepared GT03 platform has six different metal/metal oxide clusters (silver, copper, iron, nickel, palladium and mercury) as well as two cluster-free PANI·CSA films. Then they are exposed to various gases to see the "fingerprint patterns" specific to the gases (methanol, ammonia, acetone, hexanes, toluene, acetonitrile, and HCN).

2.2 Experimental Section

2.2.1 Materials

Tetrafluoroboric acid (HBF_4; Aldrich, 48 wt% solution in water), aniline (Aldrich, 99.51 %), polyaniline (Aldrich), acetic acid (CH_3COOH, Fisher, 99.8 %), mercuric chloride ($HgCl_2$, Aldrich), cupric sulfate ($CuSO_4$, Fisher Scientific), ferrous sulfate, 7-hydrate ($FeSO_4 \cdot 7H_2O$, J.T. Baker), nickelous sulfate, 6-hydrate ($NiSO_4 \cdot 6H_2O$, J.T. Baker), and silver nitrate ($AgNO_3$, Aldrich) were used as received.

2.2.2 Methods 1: Hg_2Cl_2*PANI for HCN Sensing

2.2.2.1 Electrochemical Preparation of PANI

The PANI was electrochemically polymerized on a Pt foil in 0.1 M aniline/2 M HBF_4 solution with a Pt foil counter electrode and a quasi Ag/AgCl in 1M KCl reference electrode

using a Scanning Potentiostat (Model 362, EG& G). The potential range was controlled from 0 to 0.85 V for the first 20 min and then changed to -0.05 to 0.08 V until a thick green PANI film was formed on the Pt electrode (ca. 7 hours) at a scan speed of 50 mV/s.

2.2.2.2 Preparation of PANI + $HgCl_2$ in Formic Acid Solution

After the cleaning procedure [15], 1.1 mg of dry PANI-EB (Emeraldine Base) powder removed from the Pt electrode was dissolved in 0.25 mL of formic acid. Separately, $HgCl_2$ powder was dissolved in formic acid to be 0.01 M. The solutions were mixed together before casting in a volume ratio of 1:1.

*2.2.2.3 Preparation of Hg_2Cl_2*PANI Film*

The PANI + $HgCl_2$ films were drop-cast on the GT03B platform with a glass capillary. After drying at room temperature, the films were electrochemically cycled in 1M acetic acid within the potential range of -0.2 to 0.35 V vs. Ag/AgCl at a scan speed of 20 mV/s for 10 cycles with a Potentiostat/Galvanostat (Model 273A, EG& G). The scan was stopped at 0.35 V. After washing the films with deionized water shortly, the sensors were placed in a closed container in the presence of KCN powder overnight .

2.2.2.4 HCN Sensing Experiment

An HCN permeation tube (1226 ng/min at 30 °C, VICI) was used for the HCN gas source and a pressurized N_2 tank (Airgas) was used as a carrier gas with the Environics S4000. A glass vial containing water was placed between the gas output of the Environics and the gas flow through cell to introduce wet HCN gas. The experimental setup for HCN gas exposure is shown in Figure 2.3. The output gas volume flow rate was 30 cm^3/min. The chemFET responses were measured by passing a constant drain-source current of $I_{DS} = 0.2$ mA and the gate voltage change was measured. The chemiresistor responses were measured by passing a constant current of 10 μA between the contacts and the voltage change across the film was monitored. The HCN concentrating was changed from 0 to 1, 5, 10, 20 and 0 ppm in wet N_2.

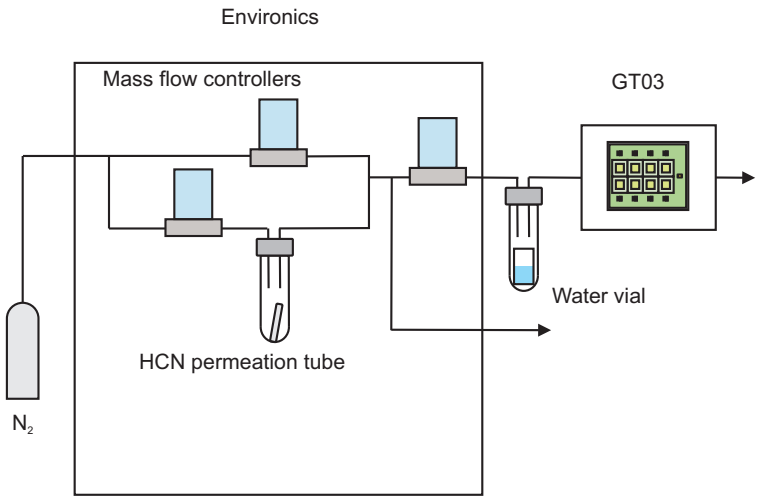

Figure 2.3: Experimental setup for HCN sensing experiment using Environics. A vial containing water was placed before the gas flow through cell to make the gas wet.

2.2.3 Methods 2: (Metal/Metal oxide)*PANI for Gas Sensor Array

2.2.3.1 Preparation of PANI

The PANI used in this experiment was purchased from Aldrich and the preparation is already described in Section 3.2.3.

2.2.3.2 Electrochemical Activation of PANI·CSA Matrix

The drop-cast PANI·CSA films on the GT03 platform were electrochemically activated by applying a constant voltage of -0.25 V vs. Ag/AgCl in 1M H_2SO_4 for 60 second using a Potentiostat/Galvanostat (Model 273A, EG& G) or an Electrochemical Workstation (Model 660, CH Instruments). After the electrochemical activation step, the PANI·CSA films were blow-dried with a N_2 gun shortly and ca. 0.02 mm^3 of the metal salt solutions were dropped into each sensing module with a glass capillary. After 2 to 4 hour cluster deposition time, the films were washed shortly with deionized water and dried at room temperature. All the metal salt solutions were made to be 2 mM in 1M H_2SO_4. Table 2.1 shows the summary of the applied potentials and the metal salt solutions. Module 7 and 8 do not have any clusters and only Module 7 was activated but not Module 8.

Table 2.1: Applied potentials for the PANI·CSA activation and the metal salt solutions for the cluster formation.

Module	Applied potential [V]	Cluster solution
1	-0.25	Ag_2SO_4
2	-0.25	$CuSO_4$
3	-0.25	Fe_3SO_2
4	-0.25	$NiSO_4$
5	-0.25	$PdSO_4$
6	-0.25	$HgSO_4$
7	-0.25	No solution‡
8	OCP†	No solution‡

†: No potential was applied (OCP) but in the same 1M H_2SO_4 solution.
‡: The film had no metal salt solution.

*2.2.3.3 CVs of (metal/metal oxide)*PANI·CSA Films in 1M H_2SO_4*

After the activation and cluster deposition processes, the cluster and PANI·CSA composite films on Pt electrodes, prepared in the same way described in the previous section, were electrochemically cycled in 1M H_2SO_4 solution to see the redox chemistry of the clusters.

2.2.3.4 Gas Sensing Experiment

The GT03 platform with 6 different metal/metal oxide clusters was operated in the chemFET mode for gas sensing after 90 min UV treatment (Chapter 1). The experimental setup for gas exposure is shown in Figure 3.8a. The vapors from solutions of methanol, ammonium hydroxide solution, acetone, hexanes, toluene, and acetonitrile and a vapor from solid of KCN were used. The diaphragm of Cell 05 was operated at a frequency of 720 Hz and with a supplied voltage of 26 Vrms.

2.3 Results and Discussion

2.3.1 Methods 1: Hg_2Cl_2*PANI for HCN Sensing

2.3.1.1 Formation of Hg_2Cl_2 Clusters in PANI Matrix

Figure 2.4 shows the last cycle of the CV of the PANI and $HgCl_2$ film on a Pt electrode (0.20 cm^2). The broad cathodic peak around 0.05 V, characteristic to the acetic acid is seen [15]. However, any obvious reduction peak of $HgCl_2$ was not observed presumably due

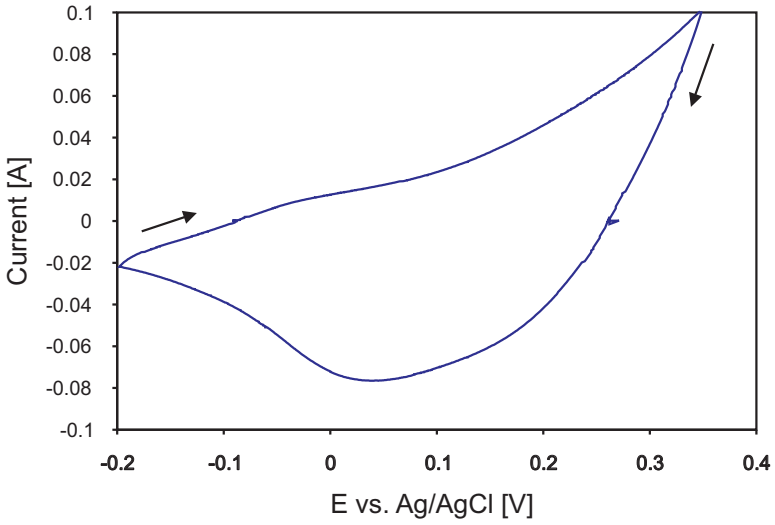

Figure 2.4: Cyclic voltammogram of PANI + $HgCl_2$ film in 1 M acetic acid at 50 mV/s.

to the small amount of the $HgCl_2$. The open circuit potential of the film before the CV was 0.436 V. The scan was always stopped at 0.35 V so that the mercury ion was reduced and the PANI film was in the conducting state [50].

2.3.1.2 HCN Sensing Experiment

The responses of the chemFETs in Figure 2.5a and chemiresistors in Figure 2.5b were obtained using the same film; that is, chemFET 1 and chemiresistor 1 are from the same sensing Module 1 modified with the Hg_2Cl_2*PANI film. It is known that the chemFET response follows the logarithm of the gas concentration (Equation 4.1) but the chemiresistor does not necessarily show the "logarithmic response". However, to obtain the detection limit and the sensitivity of the chemiresistor, it was assumed that the chemiresistor response to the HCN follows Equation 4.1. The calibration curves of both chemFETs and chemiresistors in Figure 2.6 are obtained using averages of the two sensing modules. It is clearly seen that the 3σ of the chemFETs shown as error bars is much smaller than the one of chemiresistors. This is because the sensitivity of the chemiresistors is influenced by the film thickness as discussed in Chapter 1. Table 2.2 shows the sensitivities and the detection limits of the sensors, and their standard deviations (σ). The detection limits were obtained based on the 3σ (σ is the standard deviation of the sensor baseline). From the calculation, both types of the transduction modes (chemFET and chemiresistor) can be expected to show sub ppm

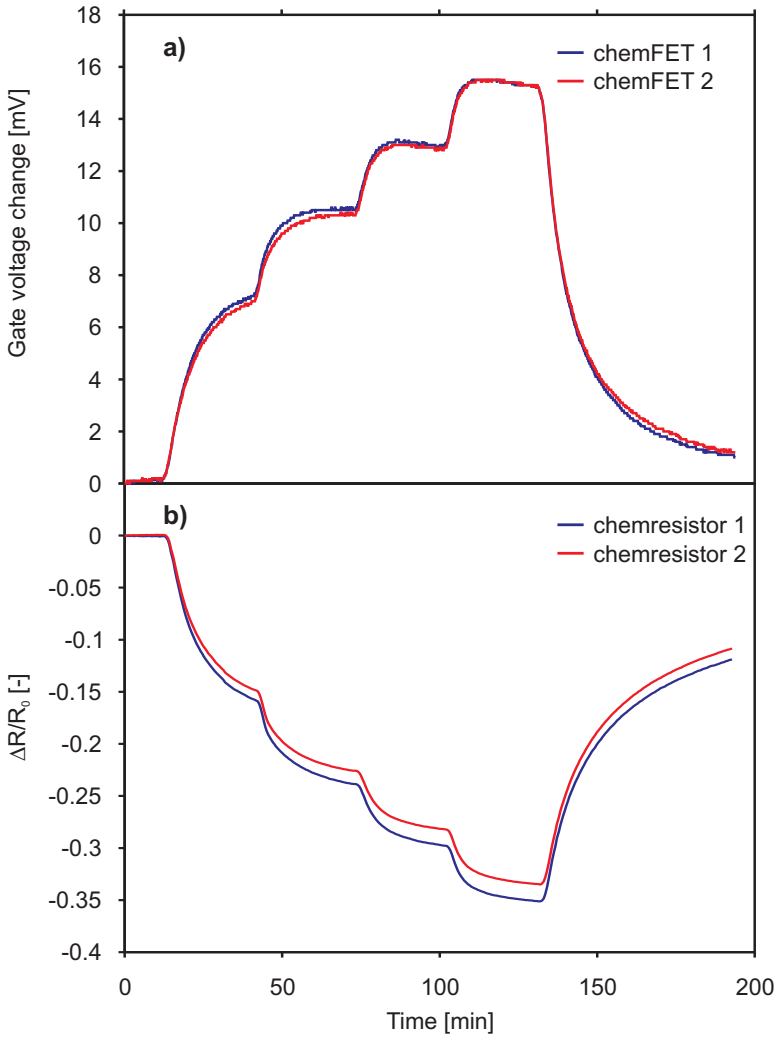

Figure 2.5: Responses of two sensing modules in the chemFET mode (a) and in the chemiresistors mode. The modules have the Hg_2Cl_2*PANI film. The concentration steps of the HCN gas are from 0 to 1, 5, 10, 20 and 0 ppm in N_2.

detection of HCN gas.

The Hg_2Cl_2*PANI film was acid-doped with acetic acid. The average of the film resistances became from 77 kΩ to 650 kΩ after 44 days, whereas, the average of the threshold voltages of chemFETs changed from -0.649 V to -0.578 V after 22 days. This instability comes from the volatile dopant-acid (acetic acid). Therefore it is concluded that a stable (non-volatile) dopant-acid is important to obtain stable gas sensor signals as discussed in Section 1.3.1.

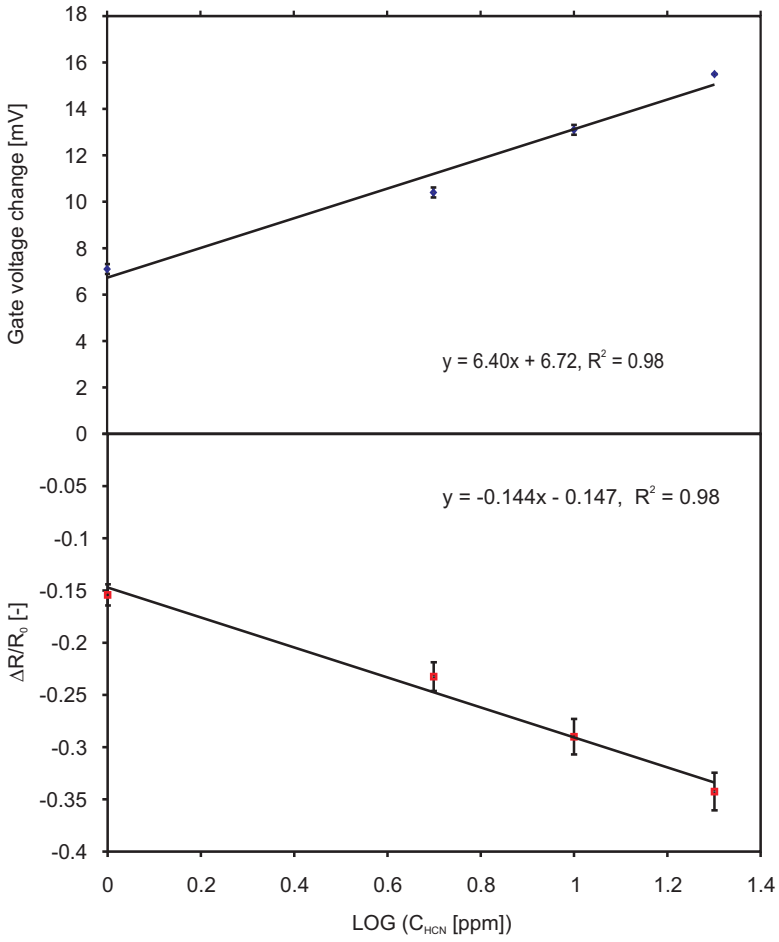

Figure 2.6: Calibration curves of (a) chemFET and (b) chemiresistor to HCN gas (1, 5, 10, and 20 ppm). Each data point is an average of the two different sensing modules (Figure 2.5) and the error bars are 3σ.

Table 2.2: Detection limits of HCN gas with the chemFETs and the chemiresistors modified with Hg_2Cl_2*PANI film and their sensitivities.

	chemFET	chemiresistor
Detection limit [ppm]	0.090 ± 0.008	0.094 ± 0.004
Sensitivity	6.4 ± 0.08 [mV/decade]	-9165 ± 747 [Ω/decade]

2.3.2 Methods 2: (Metal/Metal oxide)*PANI for Gas Sensor Array

2.3.2.1 PANI·CSA Film Activation

Figure 2.7a shows the current vs. time response during the activation of PANI·CSA film in 1M H_2SO_4 for a single-potential step chronoamperometry experiment. The potential was changed from the OCP (open circuit potential) to -0.25 V vs. Ag/AgCl. After 60 second activation step of the PANI·CSA film on Pt electrode, the OCP was measured in the same 1M H_2SO_4 without metal ions to observe the relaxation of the electrochemically activated PANI·CSA film (Figure 2.7b). The OCP of the PANI·CSA film on Pt electrode before the activation process was 0.414 V. As seen in figure 2.7b, the relaxation process is slow and lasts ca. 1 hour.

*2.3.2.2 CVs of (metal/metal oxide)*PANI·CSA Films in 1M H_2SO_4*

After the cluster deposition on Pt electrodes, CVs of each film were performed in 1M H_2SO_4 and the results are shown in Figure 2.8. The CVs of (b) copper, (c) iron, and (e) nickel have no difference from the one of PANI·CSA film without clusters. On the other hand, (a) silver, (d) mercury, and (f) palladium have additional peak(s). The anodic peak at 0.457 V for (a) silver and the one at 0.613 V for (d) mercury have the maximum in the first cycle and disappeared with the cycle as indicated by the arrow. This is because the silver and mercury metals/metal oxides were reduced and dissolved into the solution. The anodic peak of (a) silver has a small shoulder peak at lower potential, presumably due to the reduction of the silver oxide on the surface of the metal clusters. The CV of (f) palladium shows the hydrogen adsorption peak at -0.207 V and the hydrogen evolution peak around -0.3 V during the cathodic sweep. In the anodic sweep, the hydrogen desorption peak at -0.133 V and hydrogen oxidation peak at 0.206 V were observed. Those four peaks

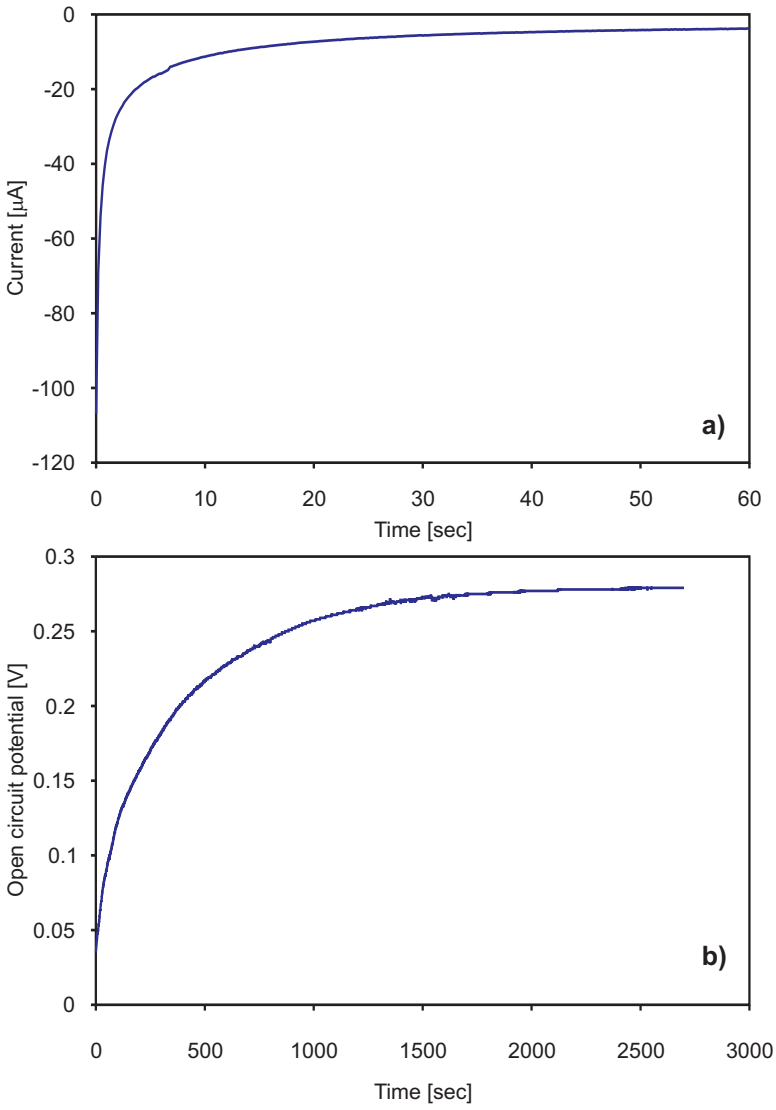

Figure 2.7: (a). Current vs. time response during the activation of PANI·CSA film in 1M H_2SO_4 for a single-potential step chronoamperometry experiment (from the open circuit potential to -0.25 V vs. Ag/AgCl). (b). Open circuit potential vs. time response during the relaxation of the same film after the 60 second activation in the same solution (1M H_2SO_4) without metal ions.

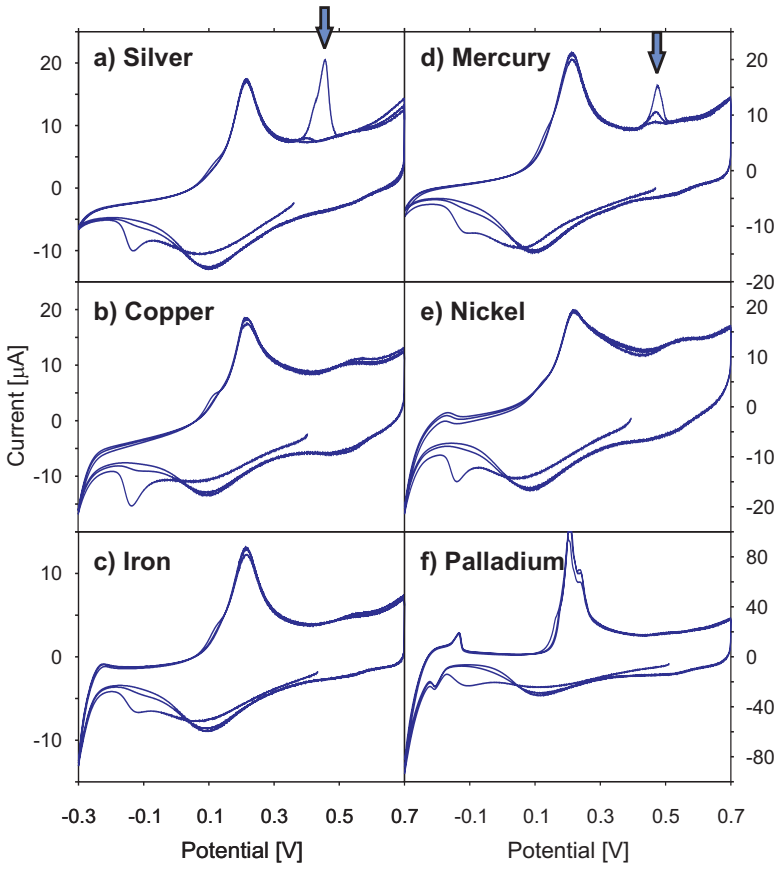

Figure 2.8: CVs of (metal/metal oxide)*PANI·CSA composite films in 1M H_2SO_4. The arrow indicates the reduction of the cluster.

suggest that the PANI·CSA matrix has Pd clusters where the sorption of hydrogen are taking place [47].

2.3.2.3 Gas Sensing Experiment

The GT03 platform, with six different composite films and two PANI·CSA, was exposed to seven different gases and the responses are shown in Figure 2.9. The plotted data are an average of three successive exposures and the error bar shows the standard deviation of the three measurements. Similar to the result in Section 2.3.1.2, Module 6 (mercury clusters) is sensitive to the HCN (Figure 2.9e). Module 1 (silver clusters) also shows the second highest sensitivity to the HCN as reported in Reference [38]. Almost all the modules respond to methanol (Figure 2.9a) and ammonia (Figure 2.9b) because of the responses of PANI·CSA itself rather than the clusters. Module 3 (iron clusters) responds well to toluene (Figure

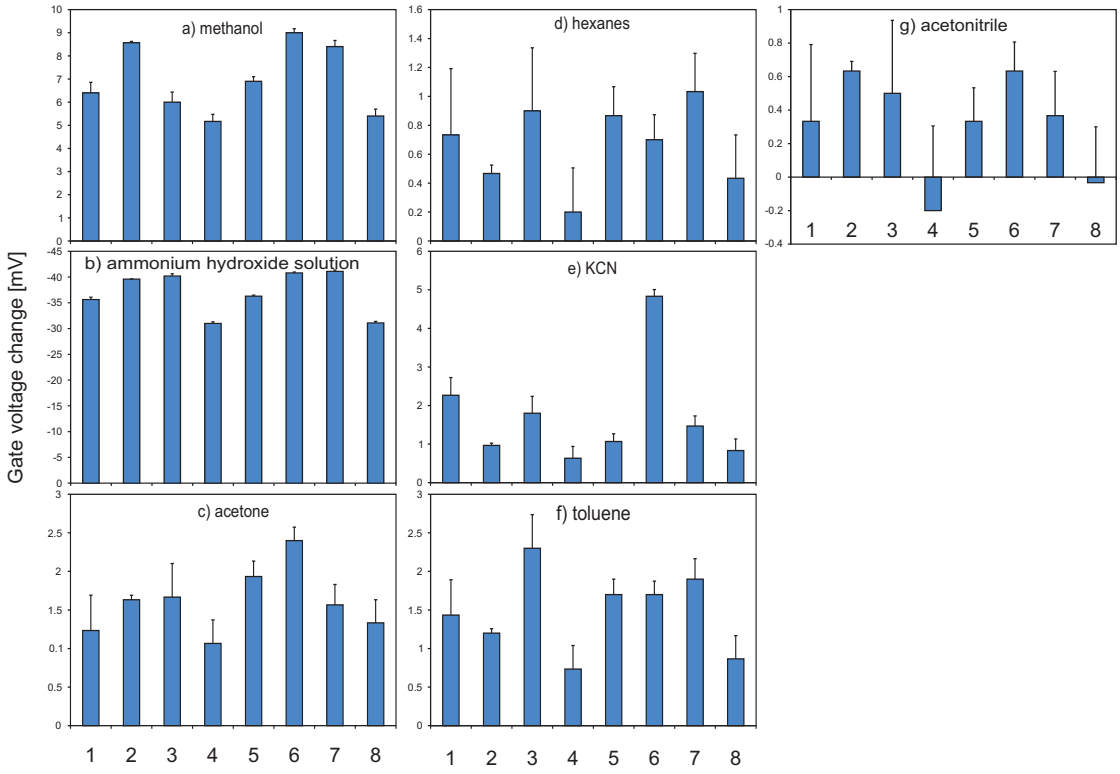

Figure 2.9: Responses of six (metal/metal oxide)*PANI·CSA composite films and two PANI·CSA films on the same GT03 sensing platform. Module 1 = silver, Module 2 = copper, Module 3 = iron, Module 4 = nickel, Module 5 = palladium, Module 6 = mercury, Modules 7 and 8 = no cluster.

2.9f). From these responses, it can be concluded that there are some "finger print" patterns specific to the gases.

2.4 Conclusions

The Hg_2Cl_2 clusters were electrochemically reduced from soluble $HgCl_2$ using Method 1. The chemFET and chemiresistor modified with Hg_2Cl_2*PANI films were used for HCN gas sensing. Both of the sensors showed sub ppm detection of HCN. However, due to the volatile dopant-acid, the threshold voltage of chemFET and resistance of chemiresistor changed over time. Therefore to realize a stable chemical sensors using PANI, a stable and non-volatile dopant-acid needs to be used.

In the second part, six different metal/metal oxide clusters (silver, copper, iron, nickel,

palladium and mercury) were introduced into the PANI·CSA matrices by Method 2 (electroless). The array of chemFETs was exposed to seven different gases (methanol, ammonium hydroxide solution, acetone, hexanes, toluene, acetonitrile and HCN). Among the gases tested, the gas-specific patterns of the responses are obtained.

CHAPTER III

DESIGN AND TESTING OF THE JET SYSTEM FOR FAST GAS SENSING

3.1 Introduction

A number of investigations, triggered by the pioneering work conducted by Persaud and Dodd [51], have demonstrated that gas sensor systems can mimic the mammalian olfaction system. The resemblance between signal processing from the multiple olfactory centers and pattern recognition technique for processing the responses of a gas sensor array has led to the descriptor "electronic nose" [51], which is now becoming successful in some applications (e.g., AromaScan, Neotronics Scientific, Alpha MOS [52]). The focus of the present work is to develop the idea further by integrating an active fluidic actuator to achieve both gas "sniffing" functionality and thereby deliver sample gases to a gas sensor or a gas sensor array and induce small-scale fluid motions near the surface of the sensor to overcome the diffusion-limited mass transfer to the surface of the sensing element. Furthermore, the fluidic element can also be used to deliver a flushing gas to clean or calibrate the sensor (as our nose dose so) in long-term operation. The fluidic functionality is achieved by integrating a millimeter-scale synthetic jet actuator [53, 54] into a gas sensor cell.

As discussed in Smith and Glezer [53] and Glezer and Amitay [54], synthetic jets are produced by time-periodic expulsion and suction of fluid through an orifice in an otherwise sealed small cavity. The flow is induced by the motion of a diaphragm (e.g., driven by a piezoelectric element) that is integrated into one of the cavity walls as shown schematically in Figure 3.1. These jets are inherently zero net mass flux (i.e., comprised entirely of ambient fluid and therefore no need of compressed gas supply) and therefore can induce directionally and spatially controlled flow field that combines sink-like entrainment of ambient fluid towards the jet orifice and source-like ejection of that fluid towards a desired target. The

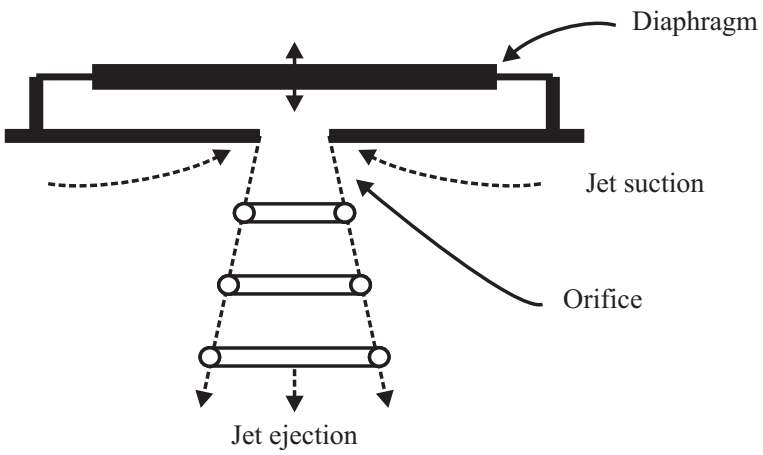

Figure 3.1: Schematic diagram of the generation of a synthetic jet by the motion of a diaphragm in a sealed cavity. As the diaphragm goes "up" the pressure around the cavity drops and the gas is sucked along the surface. When the diaphragm goes "down" the overpressure inside the cavity ejects the jet downward.

small-scale motions that are induced by the time-periodic actuation can lead to improved transport and mixing of the entrained fluid near the sensing element. While synthetic jets can be realized over a broad range of scales, micro-scale jets (having orifice diameter in the range of 10-100 μm) that are fabricated using MEMS technologies [55] are of particular interest for integration with gas sensors.

Two different prototype jet modules, Cell 02 and Cell 05, were designed to evaluate how the gas sensor responses vary with and without the synthetic jet assisted gas sampling. The first prototype (Cell 02) was designed and tested to investigate the gas-mixing in a *closed* system. The second one, Cell 05, is intended for gas sampling (sniffing) in an *open* space for more practical applications. This module is also utilized in Chapter 4 to demonstrate a practical application example (monitoring of gas filter performance).

As mentioned above, Cell 05 was designed specifically to the gas sniffing in an *open* space. The present implementation of the gas sampling system is shown schematically in Figure 3.2. The rectangular orifice is placed about 8 orifice widths away from the surface of the sensing platform. The formation of the jet induces a low-pressure domain in the vicinity of the orifice and thereby draws sample gas through an integrated conduit (that may be thought of as a "nose"). The sample gas is transported by the jet and impinges on the

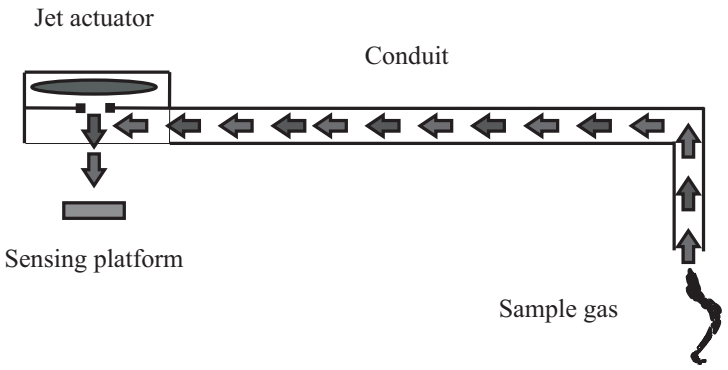

Figure 3.2: Schematic diagram of synthetic jet-assisted gas sampling system consisting of a single conduit, jet actuator, and a gas sensor.

embedded sensing platform. The volume flow rate of the sample gas can be easily regulated by the amplitude of the diaphragm motion. The crucial element of this new approach is that it eliminates the long transport time that is typically associated with diffusion of the sample gas towards the surface of the sensor. The characteristic dimensions of the jet are designed to scale with the active surface of the sensor for maximum coverage and sensitivity, which is discussed in Section 4.3.4. In the present experiments, the jet orifice measures 0.5 x 7 mm and the amplitude of the jet velocity at the orifice is about 40 cm/sec (as shown by Smith and Glezer [53], jet speeds on the order of 10-20 m/sec can be easily realized). The actuation frequency is about 1 kHz and therefore the characteristic jet period is several orders of magnitude *lower* than the response time of the gas sensor (1 to 100 sec), which is normally limited by the diffusion *through the sensing material*. The fabricated module which integrates the jet actuator, fluidic channeling, and the gas sensor is discussed in the Experimental section.

The basic functioning mechanism of Cell 02 is same as Cell 05. Cell 02 has two gas line connectors for inlet and exit of gas, which allow using Cell 02 as a normal gas flow through cell. Therefore, it is also possible to investigate the sensor response time with the perpendicularly impinging jet onto the film surface. It is of interest, especially when the sensing layer is not dense (porous or fibrous), to see the perpendicularly impinging jet effects on the "diffusion" of the gas molecules into the sensing layers, represented by the apparent diffusion coefficient (D_{app}).

The present chapter demonstrates that the integrated gas sampling (Cell 05) and mixing (Cell 02) functionality by fluidic actuation significantly improves the chemical *response times* of the sensor system. It is also studied how the impinging jet normal to the sensing surface affects the D_{app}. The detected gas is either vapor above ammonium hydroxide solution to simulate gas emission from a spilled volatile solution, or released pressurized ammonia gas to the atmosphere to simulate a continuous gas leak from a pressurized container.

3.2 Experimental Section

3.2.1 Cell 05 for Gas Sniffing in Open System

A fluidic manifold integrated with a synthetic jet module is fabricated using stereolithography. The manifold which is shown schematically in Figure 3.3 has two branches that are connected to a single feed line. Each branch is terminated in a rectangular (1.5 x 7 mm) duct (diffuser) along each of the long sides of the rectangular jet orifice (0.5 x 7 mm) so that when the jet is active, it draws the sample gas through the manifold and directs it normal to the surface of the sensor. The rectangular ducts are designed as a diffuser to improve the flow rectifying. The fluidic manifold is connected to an external tube having an internal diameter of 3.9 mm.

The design drawing of the jet module is shown in Figure 3.4 drawn by Solid Edge Ver. 15 (UGS corp.). An optical image of the fabricated fluidic module before the assembly of the driver diaphragm is shown in Figure 3.5. The jet is ejected in the direction from the orifice toward the backside of the optical image in Figure 3.5. The diaphragm (Murata Manufacturing Co.) is a unimorph construction of a piezoceramic element that is sandwiched by two 30.5 mm diameter thin metal disks as electrodes (smaller diaphragms can be easily implemented). The depth of the jet cavity is 1 mm and the diaphragm is driven at its resonance frequency (ca. 1 kHz at up to 37 Vrms) after gluing it to the cell with mixture of Stycast 2651 and Catalyst 11 (Emerson & Cuming). The distance between the orifice and the sensor is 4 mm and the jet is designed so that it impinges on all eight sensing modules on the sensing platform. In the present experiments only one module in the chemFET mode was used to compare the chemical response times in the presence and absence of the

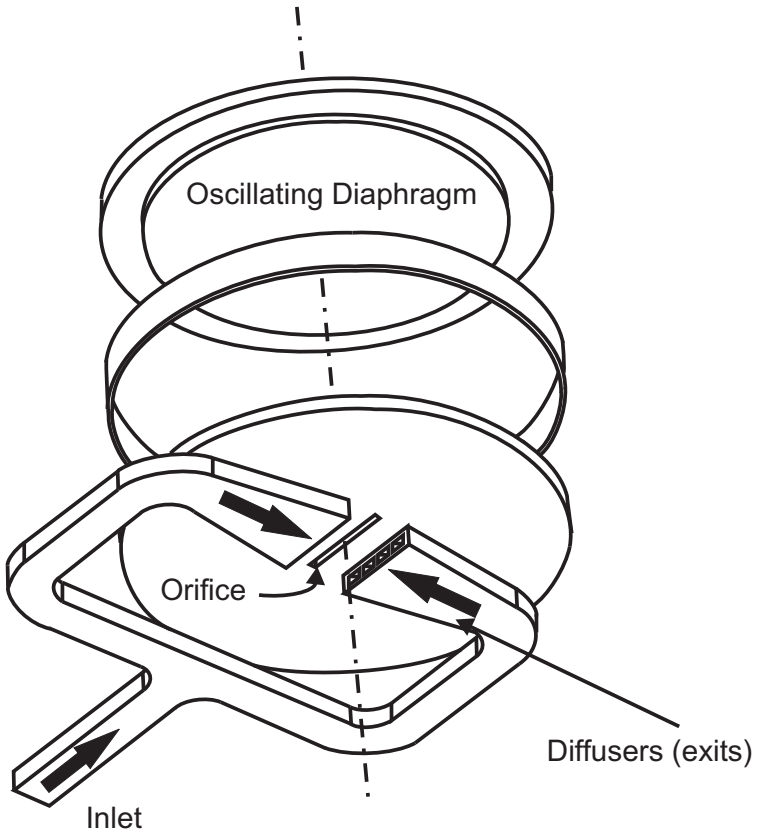

Figure 3.3: Exploded diagram of the jet actuator module (Cell 05).

jet induced gas sampling. Since Cell 05 is open to the atmosphere, the gas after sensing is pushed outside of the cell by the following jet trains as shown in Figure 4.1.

3.2.2 Cell 02 for Gas Mixing and D_{app} (Apparent Diffusion Coefficient) in Closed System

Cell 02 was designed and fabricated in the same way as Cell 05. Cell 02 can be shielded with a bottom cover (not shown) and can be used as a normal gas flow through cell with the two gas line connectors (Figure 3.6). For the gas mixing experiments one of the gas line connectors was plugged. The distance between the rectangular orifice (0.5 x 11 mm) and the oscillating diaphragm is designed to be 1 mm. The distance between the orifice and the sensor surface is 10 mm. To investigate jet effects on D_{app}, Cell 02 was used as a normal flow through cell. In this case the main gas flow to Cell 02, indicated by the white arrows in Figure 3.6, was supplied by Environics 4000S (Environics, Inc.).

3.2.3 Gas Sensor

The gas sensor is constructed using the GT02 (Figure 3.7) or GT03 (Figure 4.2), and both of them have identical eight sensing modules. Each module can be operated in the chemFET (Chemically sensitive Field Effect Transistor) mode or in the chemiresistor mode [13] with a drop-cast conducting polymer film. The micro-structured wells are designed to allow casting different films on the same platform [16]. Polyaniline (PANI) doped with camphorsulfonic acid (CSA) was used as the sensing material. For all the gas sensing experiments in this chapter, only the chemFET mode was used. In Chapter 4, all eight modules were used to observe the gas concentration distributions of ammonia gas on the sensing platform surface.

After a cleaning procedure of undoped polyaniline emeraldine base powder (PANI-EB) [15], 50 mg of the dry PANI-EB powder (Aldrich) was dissolved in 10 mL of 88 % formic acid (Fisher Scientific) with 10 min sonication followed by overnight stirring. To this solution of polyaniline emeraldine salt (PANI-ES), (1R)-(-)-10-camphorsulfonic acid (Aldrich) was dissolved into the solution with 10 min sonication so that there are two CSA molecules per four benzene units of PANI (PANI·CSA). For the gas sniffing experiment, this stock

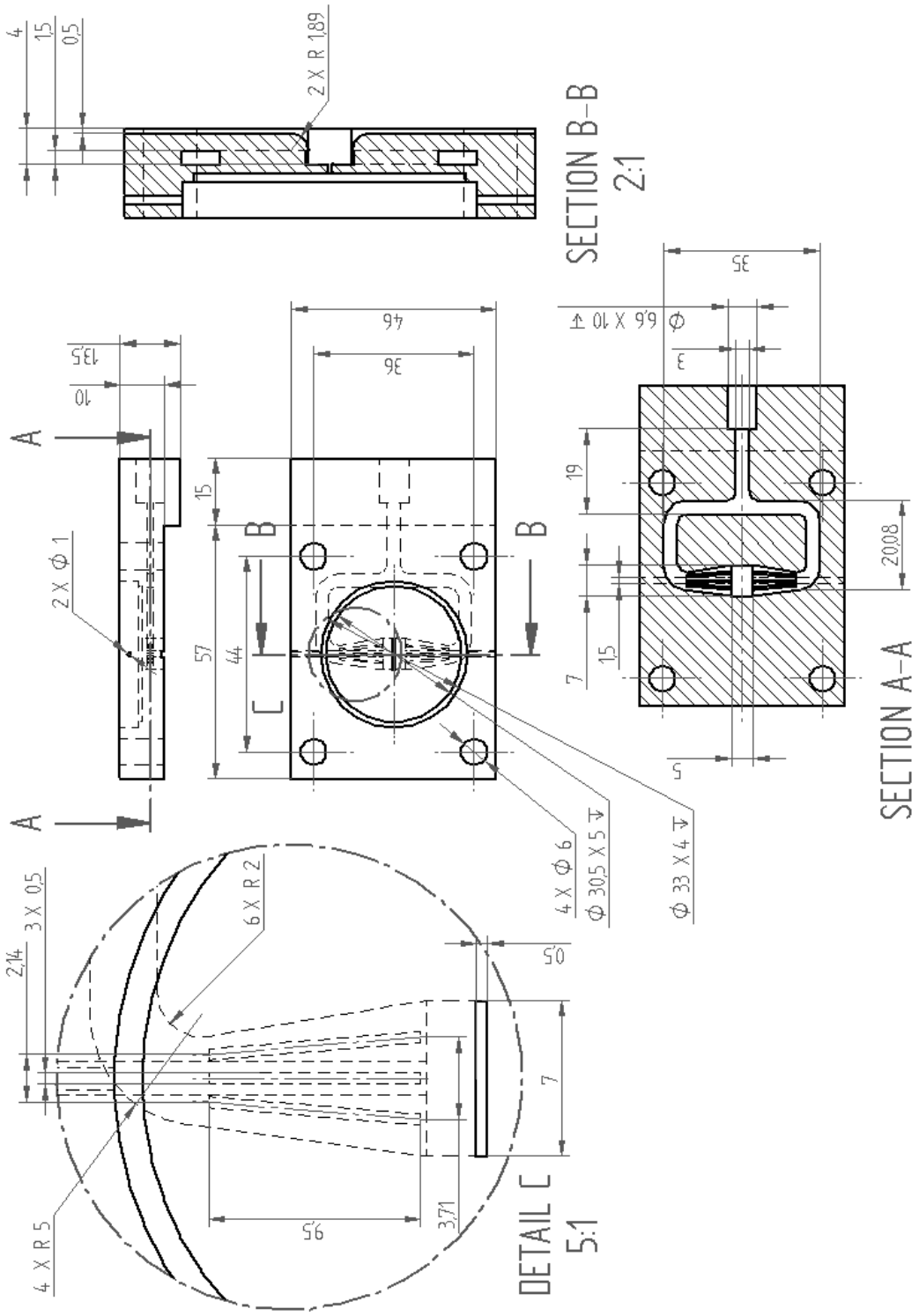

Figure 3.4: Design drawing of the jet module (Cell 05).

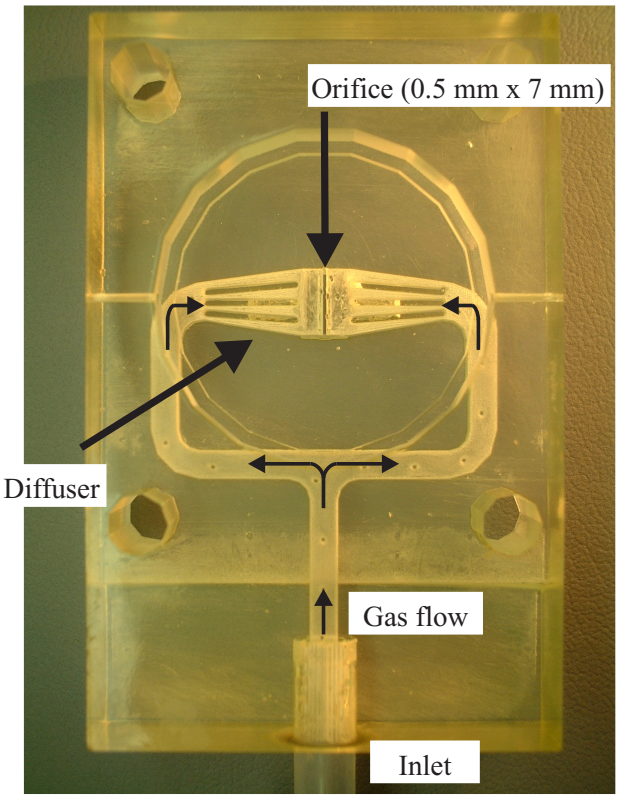

Figure 3.5: Optical image of the fabricated fluidic module (Cell 05) before the oscillating diaphragm is assembled.

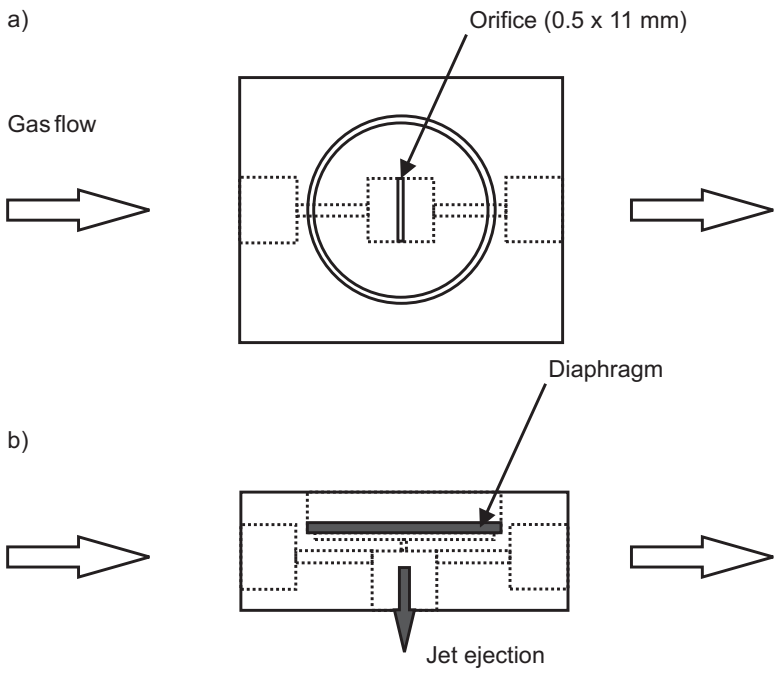

Figure 3.6: Schematic of designed Cell 02 for closed space mixing showing (a) top view and (b) side view. With a bottom shielding cover, the cell can be used as a normal flow through cell.

solution was further diluted with formic acid if necessary. The concentrations of PANI + CSA solution are 1 mg/mL for gas sniffing, 5 mg/mL for gas mixing, and 2.5 mg/mL for D_{app} experiments. The films were drop-cast onto each module using a glass capillary (the volume of the solution dispensed is ca. 0.02 mm^3). The films were dried at 60 °C for 24 hours. Figure 3.7b shows an optical image of a sensing module with a drop-cast PANI·CSA film. The gas sensing response of a chemFET was measured as a change in the gate voltage with a constant drain-source current of 0.2 mA (Figure 3.7c).

3.2.4 Sample Gas

This chapter focuses on the characteristic response times of the sensor (1) when the jet is inactive and the sample gas (ammonia) is transported by diffusion only, and (2) when the sample gas is transported and/or mixed by the jet actuator. As noted in the previous section, two separate gas sources were used. The first source is the vapor that forms above a 29.3 % ammonium hydroxide solution (Fisher Scientific) which may be thought of as a sample of the gas that is released from a spilled volatile solution. The second source is a

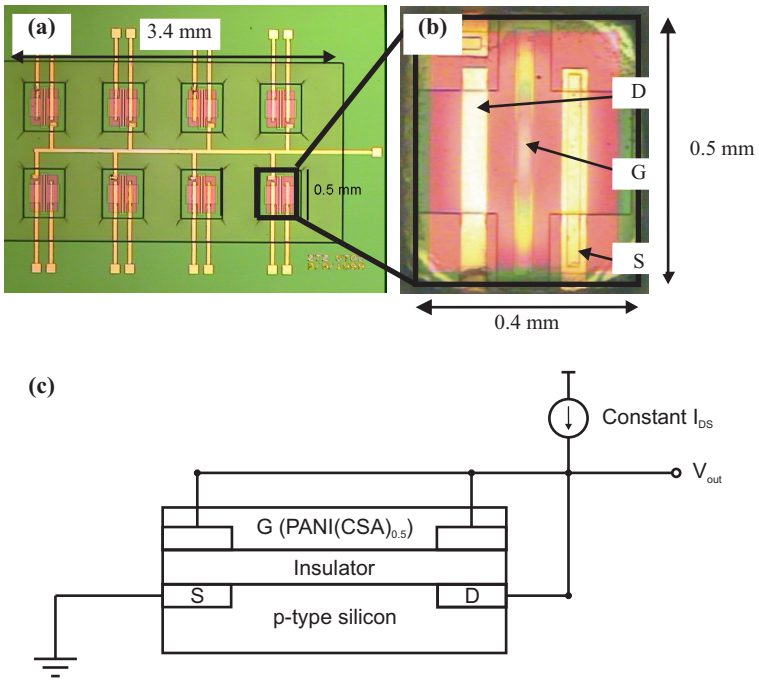

Figure 3.7: Images of 8 modules on the GT02 platform and an enlarged single module are shown in (a) and (b), respectively. The module (b) is shown after drop-casting a PANI·CSA film where D, G and S, are the drain, gate and source, respectively. A simplified schematic side view of a ChemFET with a constant drain-source current (0.2 mA) is shown in (c). The response of the sensor to sample gas is monitored by measuring the changes in the gate voltage (V_{out}).

pressurized reservoir of 5.14 % ammonia gas (Matheson) that is released to the atmosphere and may be thought of as a sample from a continuous leak of a pressurized container.

3.2.5 Gas Sniffing Setup (Cell 05)

The setups of gas sniffing experiments are shown schematically in Figure 3.8. A three-way solenoid valve (ASCO) was used to switch between the sample gas line and cleaning (flushing) gas line that is simply the ambient air pumped and transported to the sensor by the jet assisted sampling.

The induced flow rate over a range of supplied AC voltages (V_{AC}) for jet flows was computed from pressure drop measurements based on laminar Poisseuile flow [56] in the feed tube (L = 128.5 cm) using a micromanometer (Dwyer) that can resolve 6.35 x 10^{-3} mm-H_2O based on the following equation:

$$Q = \frac{\pi D^4 \Delta P}{128 \mu l} \tag{3.1}$$

where Q [m^3/s] is the volume flow rate, D is the diameter of the tube (3.9 x 10^{-3} m), ΔP [N/m^2] is the pressure drop across the feed tube, μ is the viscosity of air at 15 °C (1.79 x 10^{-5} Ns/m^2), and l is the length of the feed tube (1.285 m). The experimental setup is shown in Figure 3.9.

For the flow rate measurements, both frequency (500, 700, 720, 1000, 1250, 1300, 1500, 2000, 2500 Hz) and supplied AC voltage (6.6, 13, 20, 26, 33, 37 Vrms) were changed. The suction pressure (low pressure near the orifice) when the net flow is zero was also measured and the experimental setup is shown in Figure 3.10. The frequency was changed (500, 700, 720, 1000, 1250, 1300, 1500, 2000, 2500 Hz) with constant V_{AC} at 37 Vrms.

3.2.6 Gas Mixing Setup (Cell 02)

As mentioned in the introduction section, Cell 02 has the two gas line connectors but for the gas mixing experiments one of them was plugged and the other one was connected via a stop valve to a glass bottle (volume is 1000 mL) containing ammonia gas source (Figure 3.11). The bottle contains 50 ml of 5 times diluted ammonium hydroxide solution

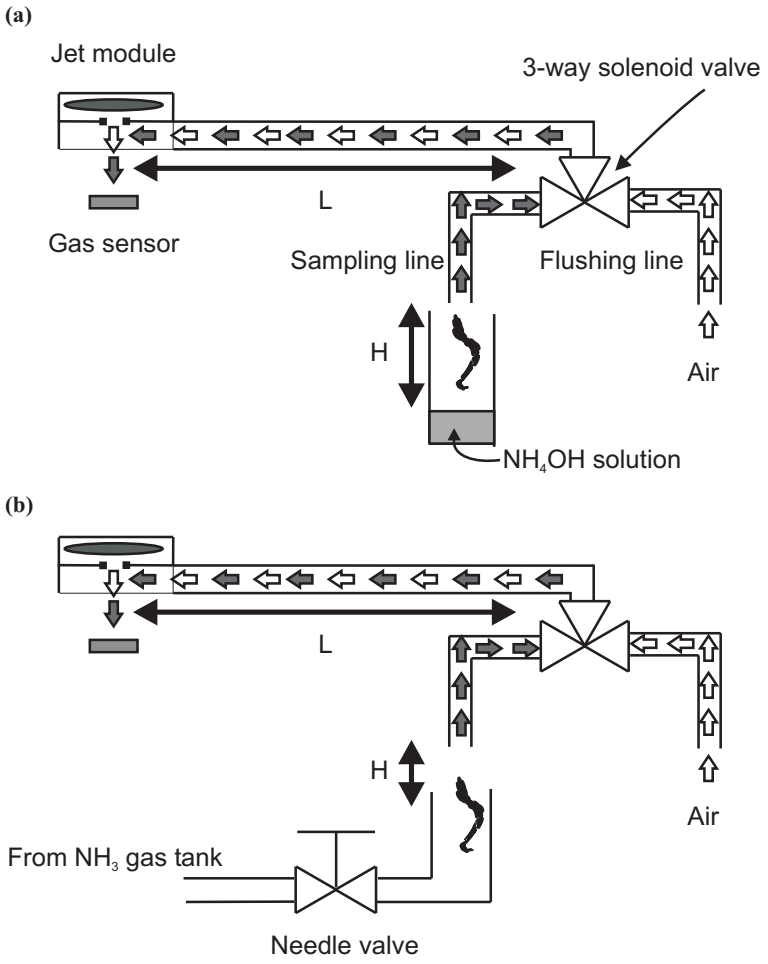

Figure 3.8: Experimental setups for gas sampling (Cell 05) with two different gas sources: (a) vapor above ammonium hydroxide solution and (b) leakage of ammonia gas through a needle valve. A three-way valve is switched between the sampling line and flushing (air) line. The separation between the sensor and the three-way valve (L), and the height (H) between the intake port of the sampling line and either the solution surface (a) or the edge of the gas tube (b) can be easily varied. The ambient (pure) air is pumped by the jet actuator.

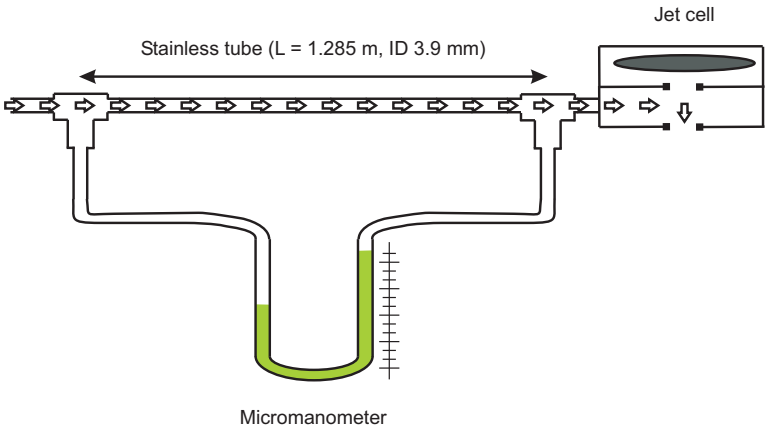

Figure 3.9: Experimental setup for the flow rate measurements (Cell 05).

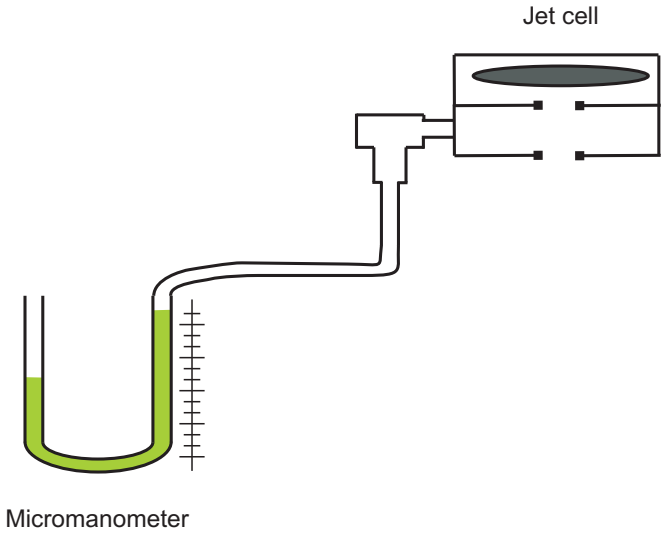

Figure 3.10: Experimental setup for the suction pressure measurements (Cell 05).

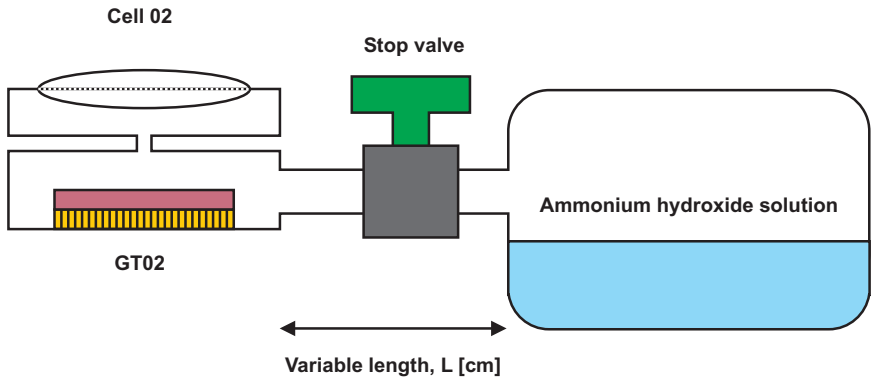

Figure 3.11: Experimental setup for jet assisted gas mixing (Cell 02) in closed system.

(29.3 %, Fisher Scientific). The size of the bottle (1000 ml) is large compared to the total volume of the tube and the cell, and it is possible to consider the bottle with the saturated ammonia vapor as a constant concentration ammonia gas source. Therefore the limiting step is the gas diffusion from the bottle to the sensor, not the evaporation of the vapor from the solution. The ammonia gas was introduced into the cell either by diffusion or by the jet induced gas mixing after the stop valve was opened. All the measurements were started after the valve was opened.

3.2.7 Apparent Diffusion Setup (Cell 02)

The experimental setup for measuring D_{app} is shown in Figure 3.12. The volume flow rate (Q_{out}) to the cell, controlled by Environics, is 50 or 70 [cm^3/s], and the V_{AC} is 0, 20, or 37 Vrms ($V_{AC} = 0$ means no jet and therefore Cell 02 is a normal gas flow through cell). The concentration steps of the ammonia gas are from 0 to 306, 0, 612 and 0 ppm in dry air.

D_{app} values with different V_{AC} and Q_{out} were obtained based on the following equation [57]:

$$\Delta V_G(t) - \Delta V_G(t = \infty) = klog(t^{-1/2}) + klog(x/2\sqrt{D_{app}}) \tag{3.2}$$

where $\Delta V_G(t)$ is the gate voltage change [mV] at time t [sec], $\Delta V_G(t = \infty)$ is the gate voltage change [mV] from $t = 0$ to ∞, D_{app} is the apparent diffusion coefficient of ammonia through PANI·CSA film [cm^2/s], x is the film thickness [cm] and k is the constant. D_{app} values were

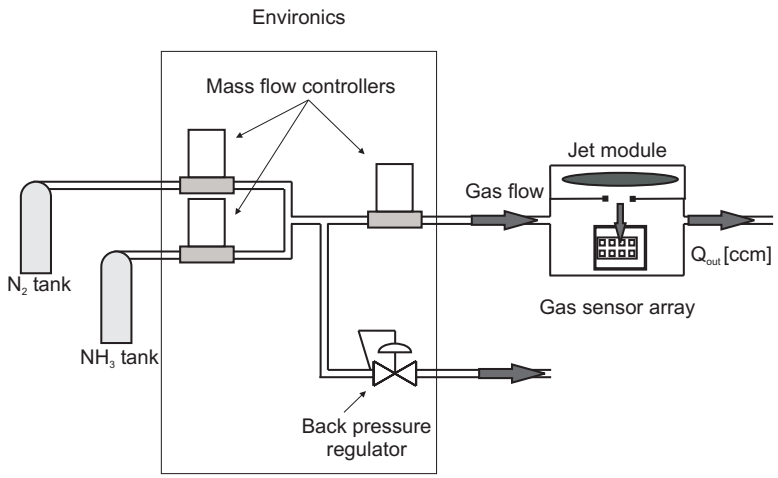

Figure 3.12: Experimental setup to measure apparent diffusion coefficient, D_{app}, of the chemFET sensor in the presence or in the absence of perpendicularly impinging jet using Cell 02. The volume flow rate controlled by Environics is Q_{out}.

obtained by plotting $\Delta V_G(t) - \Delta V_G(t = \infty)$ versus $\log(t^{-1/2})$. Equation 3.2 assumes that the limiting step of the response to ammonia is the diffusion through the film (500 nm) and the gate voltage change is linear to the logarithm of the ammonia concentration (Equation 4.1)

3.3 Results and Discussion

3.3.1 Gas Mixing in Closed System with Cell 02

Figure 3.13 shows the normalized responses with and without jet assisted mixing with different tube lengths: L = 12.5 cm, 18.0 cm, and 31.0 cm. The arrows show the improvement of the sensor response times in the presence of the jet actuation. Table 3.1 summarizes the 90 % responses, which is the time required for a sensor to reach the 90 % of the full response. The improved sensor response times result from the micro-scale mixing in the closed system induced by the jet. The 90 % response time with jet is about five times faster than the one without jet when L = 12.5 cm and 18.0 cm, and three times when L = 31.0 cm.

3.3.2 Apparent Diffusion in Closed System with Cell 02

Figure 3.14 shows chemFET responses to ammonia with different V_{AC} and Q_{out} with the experimental setup in Figure 3.12. To compare the jet effects on the D_{app}, Figures 3.14a,

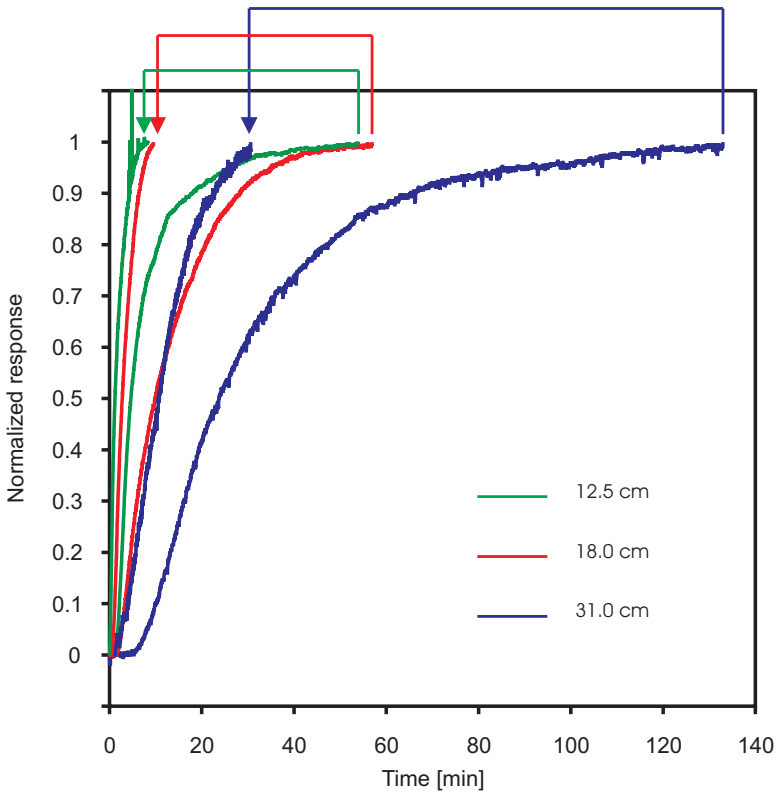

Figure 3.13: ChemFET responses to ammonium hydroxide solution vapor. When t = 0, the stop valve was opened. The arrows show comparisons with and without jet assisted mixing at three different tube length.

Table 3.1: 90 % response times with and without jet assisted mixing.

L [cm]	with jet [min]	without jet [min]	with/without jet [%]
12.5	4.2	18.0	23
18.0	6.4	28.3	23
31.0	22.7	65.1	35

b, and c have the same Q_{out} (50 cm^3/min) but increasing V_{AC} (from a to c stronger jet impinging normal to the PANI·CSA surface). In addition, Figures 3.14a and d are obtained to investigate Q_{out} effects on D_{app} without jet and to confirm that the limiting step of the sensor response is *not* the filling of the dead volume of Cell 02 with the ammonia gas *but* the diffusion of the ammonia through the PANI·CSA film.

To obtain D_{app} values using Equation 3.2, $\Delta V_G(t)$ - $\Delta V_G(t = \infty)$ versus $\log(t^{-1/2})$ were plotted using the transient responses when the introduction and removal of the ammonia gas from Cell 02. As an example, the plots when Q_{out} = 50 cm^3/min and V_{AC} = 37 Vrms are shown in Figure 3.15a for introducing ammonia and Figure 3.15b for removal of ammonia. The linear lines plotted together are the fitted curves in the linear region where the diffusion process is the limiting step.

In Figure 3.16, the calculated D_{app} values are shown when the ammonia introduction: (a) from 0 to 306 ppm and (b) from 0 to 612 ppm as well as when the ammonia removal: (c) 306 to 0 ppm and (b) 612 to 0 ppm. The data are an average of seven chemFETs on the same platform and the error bar shows the standard deviation. At the bottom of each graph, Q_{out} and V_{AC} values are listed. It is clearly seen that with the V_{AC} to the jet, the D_{app} increases when the ammonia gas was introduced (Figures 3.16a and b). Especially, the D_{app} values when V_{AC} = 37 Vrms becomes twice larger than the one when V_{AC} = 0 Vrms. This is probably due to the *convectional flow* induced by the impinging jet in the same direction as the one of the diffusion of the ammonia. If compare Figures 3.14a and c when 612 ppm ammonia was *introduced* (the second ammonia gas introduction) the transient response of Figure 3.14c (V_{AC} = 37 Vrms) reached the steady response faster than Figure 3.14a (V_{AC} = 0 Vrms). The improvement of the jet-induced D_{app} is based on the assumption that the drop-cast PANI·CSA film is not smooth compact (dense) but

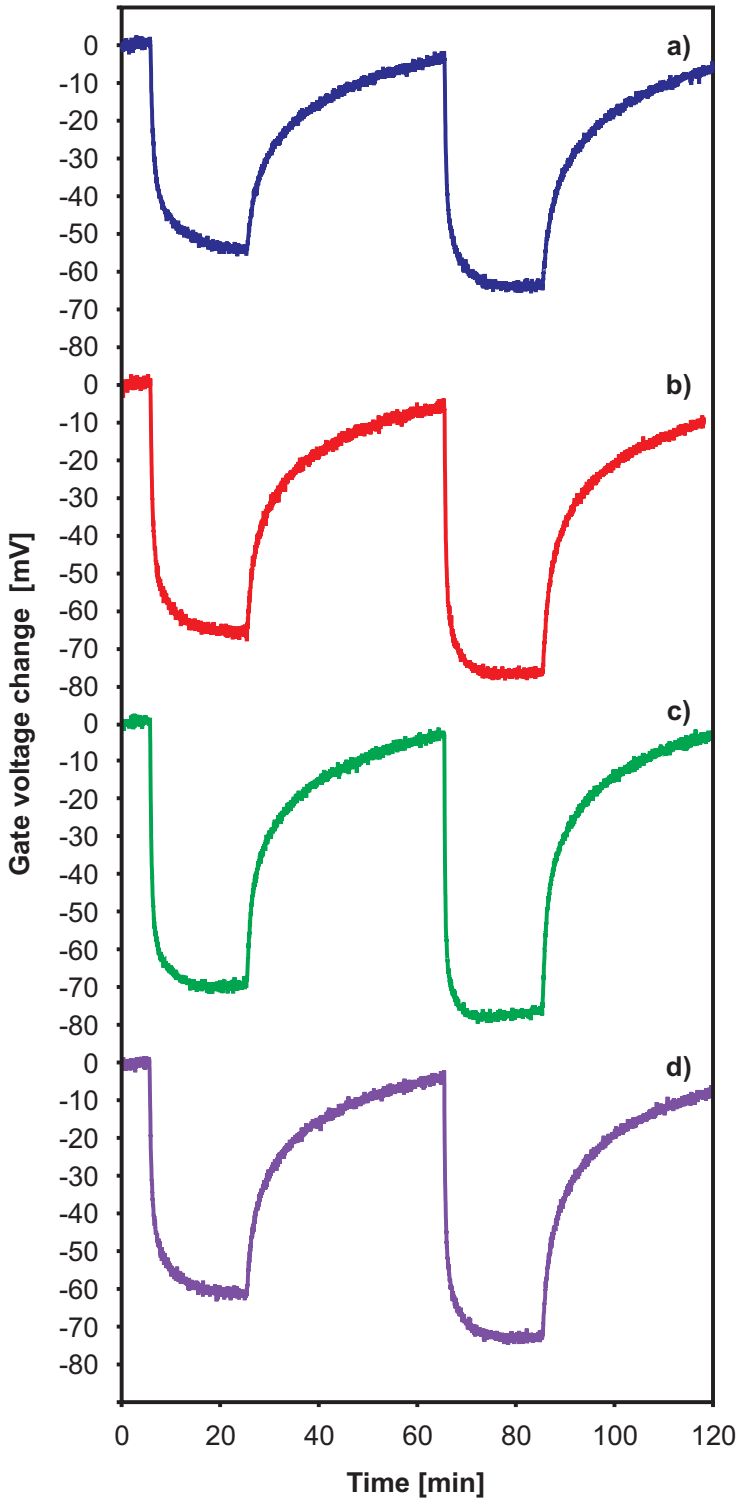

Figure 3.14: Comparison between responses of chemFET sensor with drop-cast PANI·CSA film as functions of volume flow rate (Q_{out}) of NH_3 and applied voltage (V_{AC}) to the jet when: (a) Q_{out} = 50 cm^3/min with no jet (V_{AC} = 0 Vrms), (b) Q_{out} = 50 cm^3/min with jet (V_{AC} = 20 Vrms), (c) Q_{out} = 50 cm^3/min with jet (V_{AC} = 37 Vrms), and (d) Q_{out} = 70 cm^3/min with no jet (V_{AC} = 0 Vrms). The concentration steps of the ammonia gas are from 0 to 306, 0, 612 and 0 ppm in air.

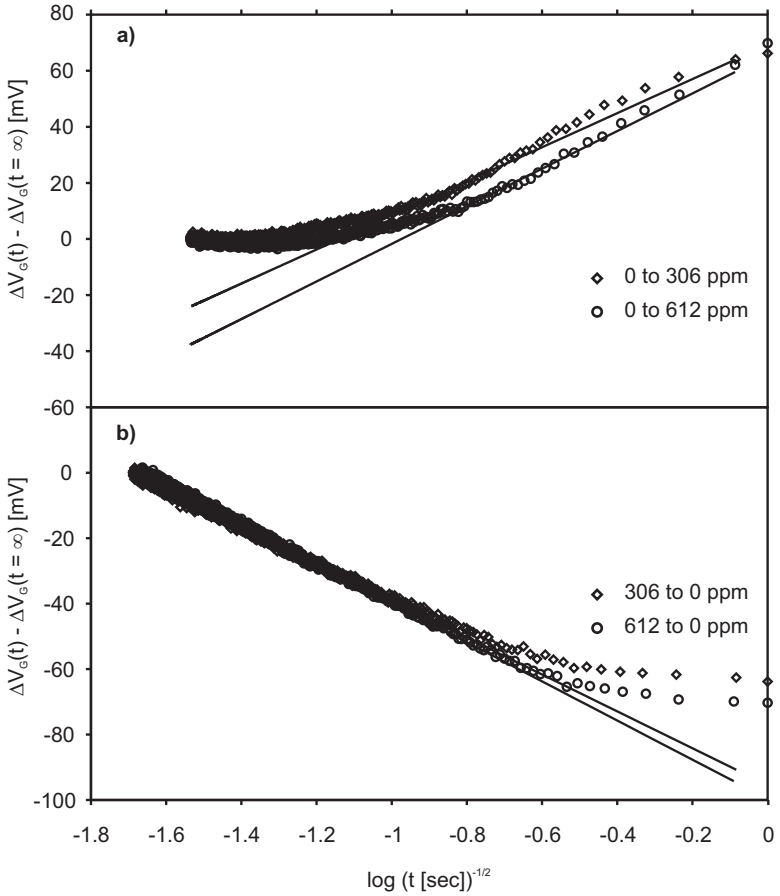

Figure 3.15: Gate voltage changes for (a) the introduction and (b) the removal of ammonia for $Q_{out} = 50$ cm^3/min and $V_{AC} = 37$ Vrms.

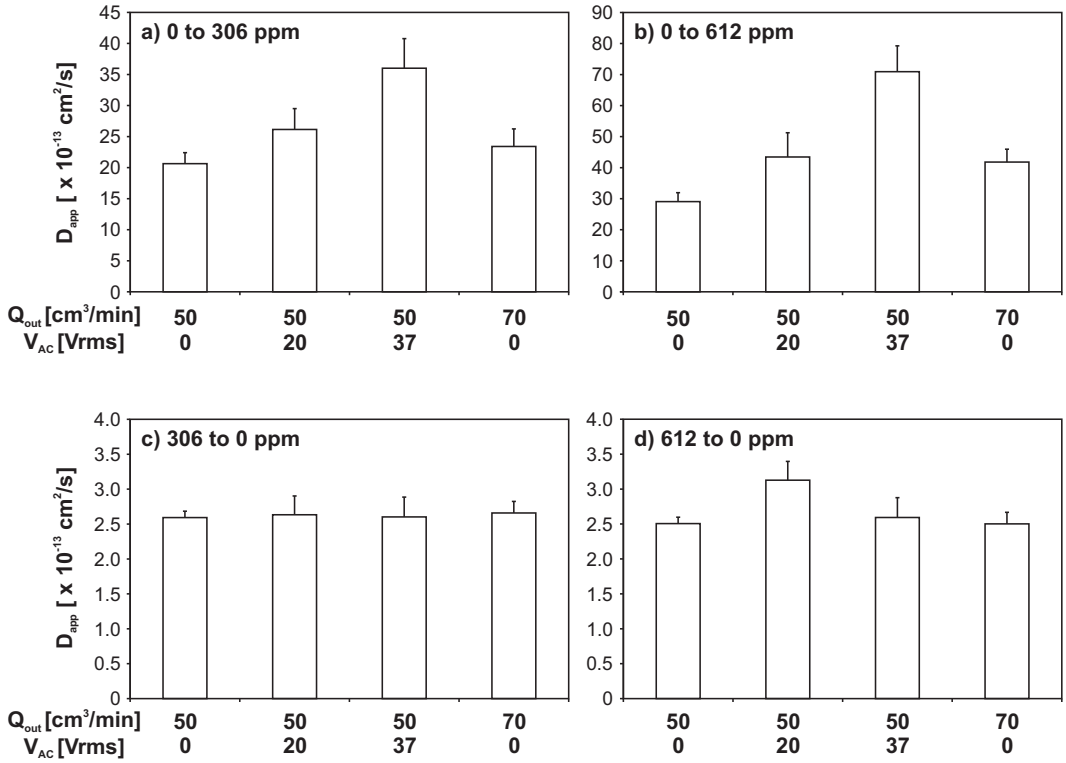

Figure 3.16: Changes in D_{app} of ammonia introduction (a and b) or removal (c and d) of ammonia from PANI·CSA film as a function of Q_{out} and V_{AC} to the jet.

porous. The film morphology changes depending on the synthetic conditions of PANI [58], acid-dopants [59], or solvents [60] and a study using SEM (scanning electron microscopy) will be helpful for the further study.

On the other hand, when the ammonia gas was removed from the PANI·CSA film (Figures 3.16c and d), there is no jet effect on the D_{app}. If the "convectional flow" is opposite to the direction of the diffusion (from the film bottom to the top), it is reasonable to assume that the D_{app} becomes *smaller* than the one without jet but further studying is required. Again, it also should be noted that the increase of the Q_{out} from 50 to 70 cm^3/min does not change the D_{app}. Thereby, the limiting step of the response to ammonia is *not* the filling of the dead volume of Cell 02 with ammonia.

3.3.3 Basic Characteristics of Cell 05

The variation of the flow rates computed from the measured pressure drops in the feed tube using Equation 3.1 as functions of F and V_{AC} is shown in Figure 3.17. These data

show two distinct peaks corresponding to the diaphragm's fundamental (nominally 1000 Hz) and the second-harmonic resonances. While the flow rate evidently increases with actuation voltage, the increase is nonlinear and appears to saturate as the voltage increases (e.g., at 2000 Hz, the flow rate increases from 1.3 to 1.5 cm^3/s as the actuation voltage increases from 26 to 37 Vrms) indicating that for a given diaphragm the power dissipated increases nonlinearly with volume flow rate. The calculated nominal velocity magnitude at the exit plane of the jet is 38 cm/s at F = 720 and 1000 Hz (V_{AC} = 37 Vrms) where the corresponding volume ejected per stroke is 0.483 mm^3 and the jet Reynolds number was calculated to be 29 based on the equation:

$$Re = \frac{\rho V D}{\mu} \tag{3.3}$$

where ρ is the density of air at 15 °C (1.23 kg/m^3), V is the velocity of the air flow (0.38 m/s), D is the diameter of the tube (3.9 x 10^{-3} m), and μ is the viscosity of air at 15 °C (1.79 x 10^{-5} Ns/m^2).

The result of suction pressure when the net flow is zero is shown in Figure 3.18. Similar to the flow rate (Figure 3.17), the suction pressure is maximum around the fundamental frequency of the diaphragm and the second peak is also observed around the second harmonic.

The power consumption for the jet actuation was obtained by measuring the AC current while applying a certain AC voltage and the result is shown in Table 3.2. It is seen that the power consumption increases quadratically with the AC voltage. This is contrary to the flow rate shown in Figure 3.17, which appears to saturate at high V_{AC} values.

The noise effect due to the impinging jet on the sensor baseline signal was examined and the result, when F = 1500 Hz and V_{AC} = 34 Vrms, is shown in Figure 3.19. There are two things should be mentioned. First, with the jet on, the baseline decreased and stabilized in less than 5 min. When the jet assisted sniffing system does not need a continuous operation or when the power consumption is the concern, the cell and the sensor can be operated in an interrupted manner (programmable operation). In that case the system including the

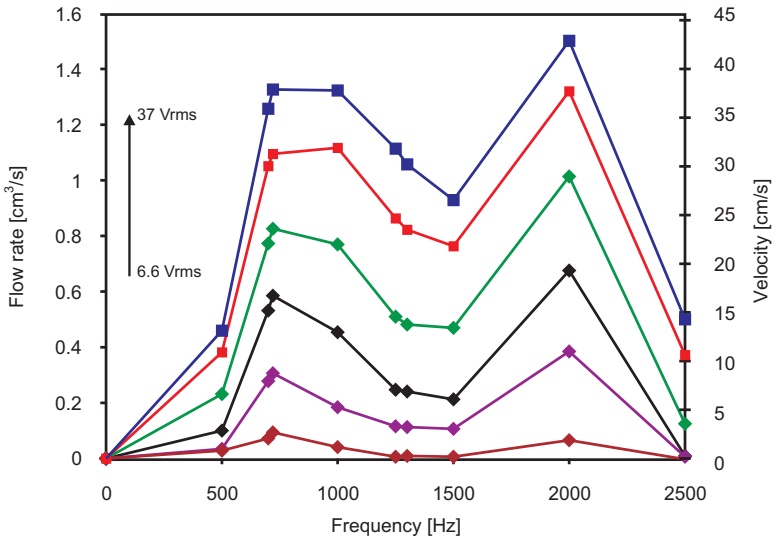

Figure 3.17: Variation of the flow rate (computed from pressure drop measurements) with frequency and actuator voltage (from bottom to top, 6.6, 9.9, 13, 20, 26, and 37 Vrms). The linear velocity was calculated based on the orifice size (0.5 x 7 mm).

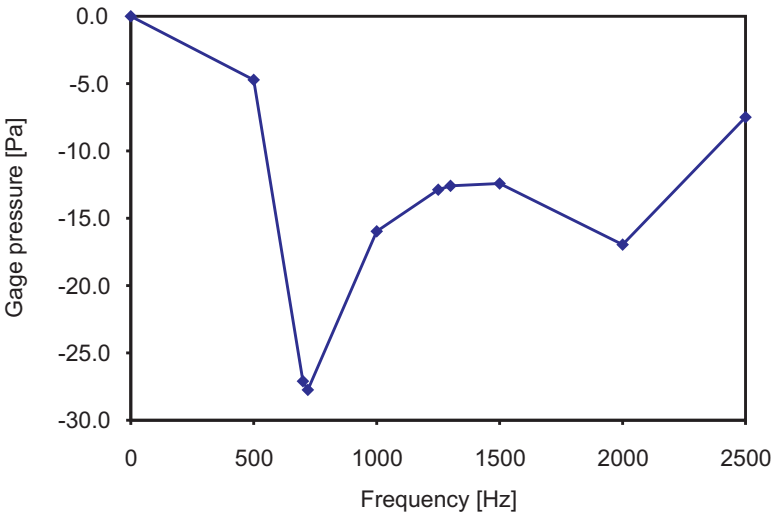

Figure 3.18: Suction pressure around the orifice when the net flow is zero. The frequency is 500, 700, 720, 1000, 1250, 1300, 1500, 2000, or 2500 Hz with constant V_{AC} at 37 Vrms.

Table 3.2: Power consumption of the jet module (Cell 05).

V [V]	I [mA]	P [mW]
6.6	0.17	1.1
9.9	0.52	5.1
13	1.4	18
20	4.6	91
26	6.7	176
37	11	387

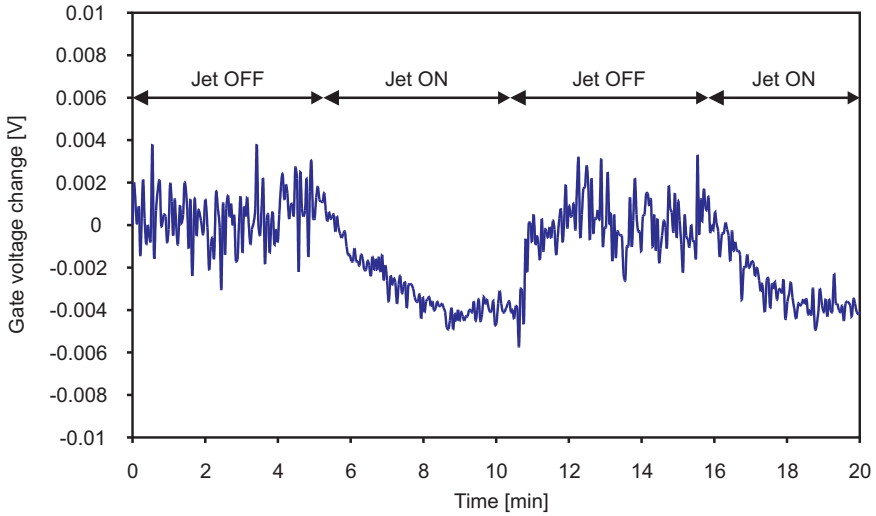

Figure 3.19: Noise effect on the sensor baseline. The frequency and applied voltage are 1500 Hz and 34 Vrms, respectively. The sensor was operated in the chemFET mode in the normal laboratory air.

sensors and the jet need c.a. 5 min to be stable after the system is on. Second, contrary to the expectation, the noise level of the baseline signal when the jet is on is smaller than when the jet is off. There is no explanation for the better noise level at this point of time.

3.3.4 Gas Sniffing in Open System with Cell 05

A sample of the responses of the chemFET sensor to the induced transport of vapor from the ammonium hydroxide solution (the setup in Figure 3.8a) when the intake port is aligned coaxially with the vial is shown in Figure 3.20a (F = 1500 Hz, V_{AC} = 37 V, H = 2 cm, and L = 17 cm). The corresponding switching time trace of three-way solenoid valve is shown in Figure 3.20b (note that when the DC voltage supplied to the three-way valve is low, it is switched to the NH_3 line). The time trace for the control experiment in the absence of the

NH_4OH solution (i.e., both lines are flushing with air) is shown in Figure 3.20c confirming that there are no changes in the sensor output due to the switching of the solenoid valve or residual gases in the system. The response of the sensor in the absence of the jet is shown in Figure 3.20d when the vapor is delivered by "natural" diffusion through the tube. In this control experiment, the three-way vale was kept open to the ammonia line after a 5 min flushing interval with pure air (Figure 3.20e). These data show that *in the presence of the jet the response time of the sensor is remarkably faster by about two orders of magnitude (20 compared to 1800 seconds)* showing that fluidic actuation can significantly improve the detection performance by adding "sniffing" and mixing functionality. This result suggests that for critical applications of a gas sensor system, an addition of the jet pumping system is effective in improving the response time of a sensor system.

A similar (but not identical) experiment was conducted to assess the sensor response to ammonia gas release (leakage) from a pressurized (40 psi) NH_3 tank (the setup in Figure 3.8b). In this case, the released *leak* jet (flow rate of 46 cm^3/sec) is deliberately directed towards the system tube (gas intake port) to allow for forced convection of the ammonia towards the sensor even in the absence of the jet actuation. The response of the sensor is shown in Figure 3.21a (here L = 17 cm, F = 1000 Hz, V_{AC} = 37 V and H = 0.5 cm). The three-way valve was controlled in the same manner as in Figure 3.20b (when the DC voltage to the three-way valve is low, the sensor is switched to the NH_3 line). Despite the fact that the response in the absence of the actuator jet is assisted by the leak jet, the actuator jet still improves the sensitivity of the system by more than an order of magnitude. The response in the presence of the actuator jet is about 20 seconds, and this response degrades to 600 seconds when the jet is turned off.

As shown in Figure 3.22, when wet ammonia gas was introduced to the sensor, the gate voltage change became positive (Figure 3.22a), while the one to the dry ammonia was negative (Figure 3.22b). This is caused by the water vapor coming out of the solution and is a unique characteristic of the sensors measuring work function changes of a sensing layer (chemFET or Kelvin probe [48]). Depending on whether the gas molecule is donating or accepting electrons to or from the PANI film, the gate voltage can change in either direction

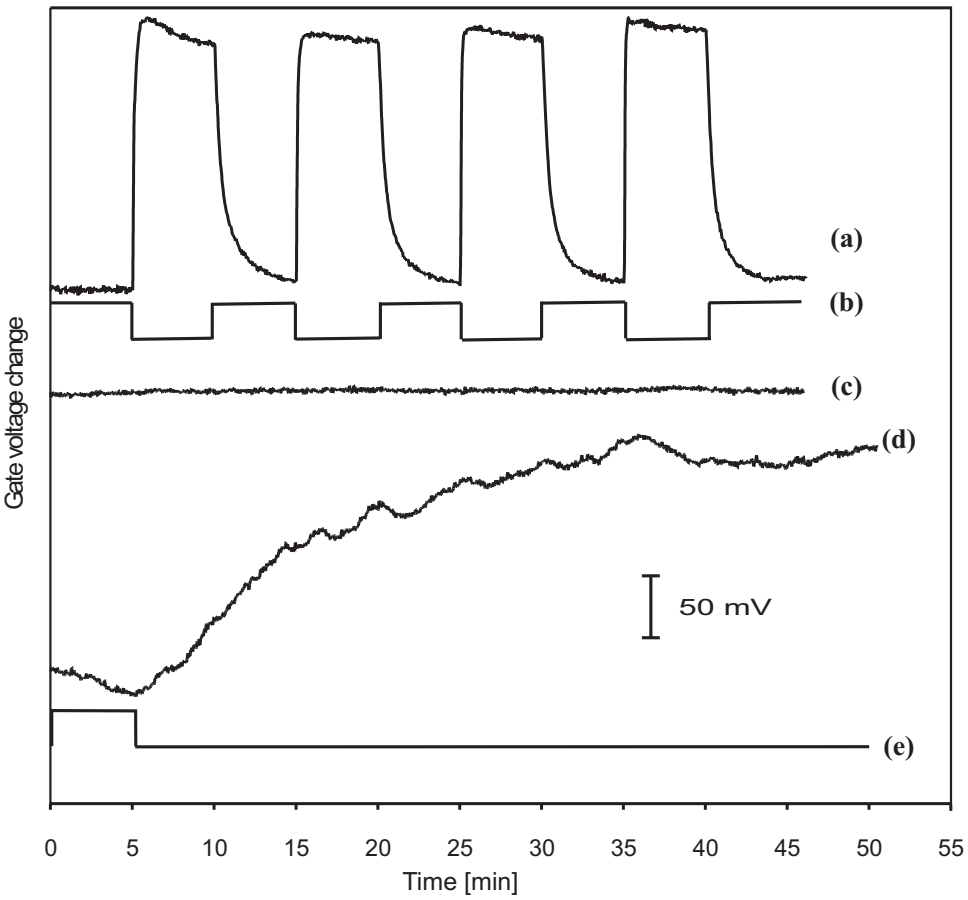

Figure 3.20: Response of the sensor to the induced flow of ammonia gas formed above ammonium hydroxide solution (a) as the three-way valve is switched between the ammonia and flushing air lines at 5-min interval (time trace b). The response (c) is measured when the valve is switched with the same time trace (b) in the absence of the ammonium hydroxide solution. The corresponding time trace of the sensor when the jet is inactive and the three-way valve is opened to the ammonia line (following 5 minutes of flushing with air as shown in time trace e) is (d).

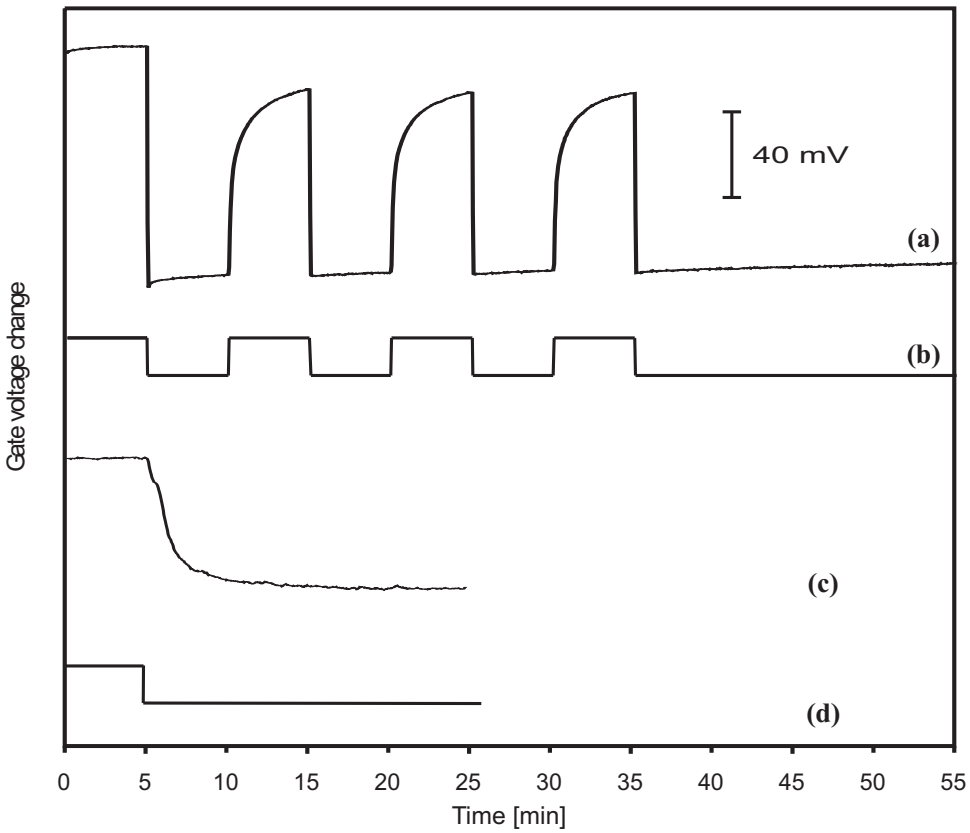

Figure 3.21: Sensor response to an ammonia gas jet released from pressurized tank through a needle valve (a) as the three-way valve is switched between the ammonia and flushing air lines at 5-min interval (time trace b). The corresponding time trace when the jet is inactive and the three-way valve is opened to the ammonia line (following 5 minutes of flushing with air as shown in time trace d) is (c). L = 17 cm.

(see Figure 2.1).

The experiments shown in Figure 3.21 were repeated for a longer feed tube (L = 120 cm) and the response is shown in Figure 3.23a. Despite the fact that the *leak* jet is inducing convection in the feed tube, the response times decreases from 1800 (in the absence of the jet) to 20 seconds (in the presence of the jet). This indicates that as the length of the feed tube increases (or alternately the distance from the source), the effect of the jet actuator becomes more pronounced in overcoming diffusion-limited transport. It also should be mentioned that the noise level with the jet on (Figure 3.23a) is *smaller* than the one with the jet off (Figure 3.23c). This observation agrees well with the one in Figure 3.19.

The performance of the jet actuator was assessed for a range of feed tube lengths (from 17 to 120 cm) and actuation power is shown in Figure 3.24. The characteristic time required to

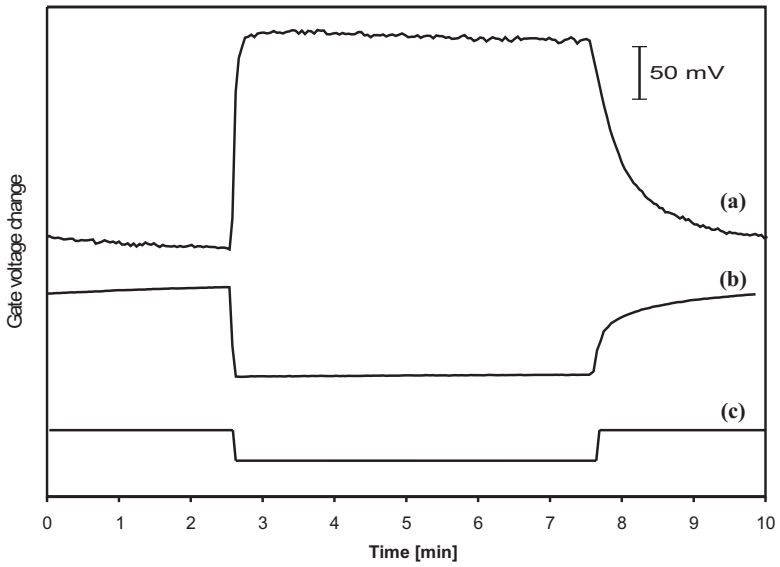

Figure 3.22: Comparison of the responses to (a) "wet" and (b) "dry" ammonia gases. The solenoid valve is switched to the sampling line (ammonia gas) when the three-way valve voltage is low as shown in (c). Note the opposite response to wet and dry gases.

reach 90 % of the steady sensor output (following the switching transient) was measured for ammonia gas released from the pressurized NH_3 tank (Figure 3.8b). These data show that while at low actuation power the jet performance improves, there is typically no advantage in increasing the actuation power beyond a certain level because the response of the sensor is limited by internal diffusion (the apparent diffusion coefficient for a film thickness of 200 nm is 5 x 10^{-11} cm^2/s [43, 57]). In fact Figure 3.24 shows that when the power is higher than 90 mW, the 90 % response time is almost independent of the length of the feed tube (about 20 seconds). These data also indicate that significant performance improvements can be achieved even at low actuation power. When acoustic emission is an issue, the jet can be efficiently driven using electromagnetic diaphragm that operates at frequencies on the order of 100 Hz. The present data suggests that even at these frequencies (100 Hz), the actuation period is still far lower than the characteristic response time of the sensor (20 seconds) and therefore no significant performance degradation is anticipated. Another way to conserve actuation energy is to operate the actuator in a time-modulated sequence since it can be easily turned on and off as shown in Figure 3.19.

Another observation to be mentioned is when the flow rates were measured using a soap

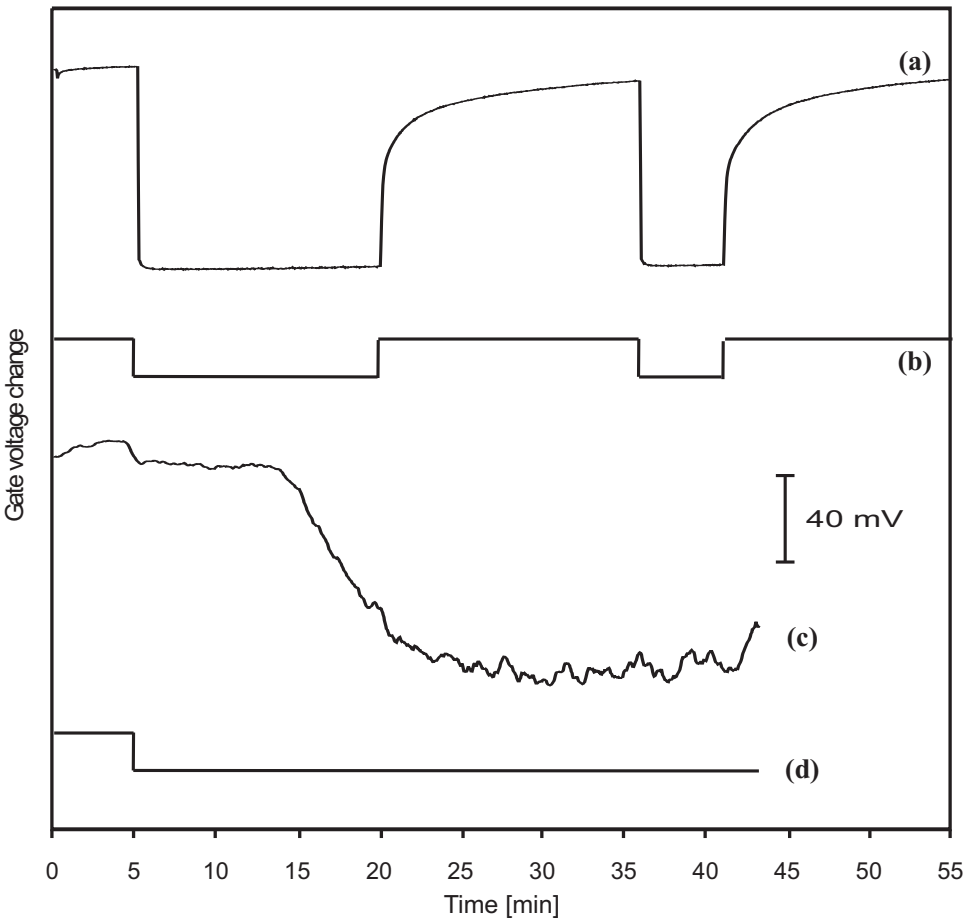

Figure 3.23: Sensor responses to dry ammonia when L = 120 cm similar to the ones in Figure 3.21. The time trace (a) is the sensor response when the three-way valve is switched between the ammonia and flushing air lines as shown in (b). Time trace (c) is the response in the absence of the jet actuator when the three-way valve is open to the ammonia line after a 5-min flush with air (d).

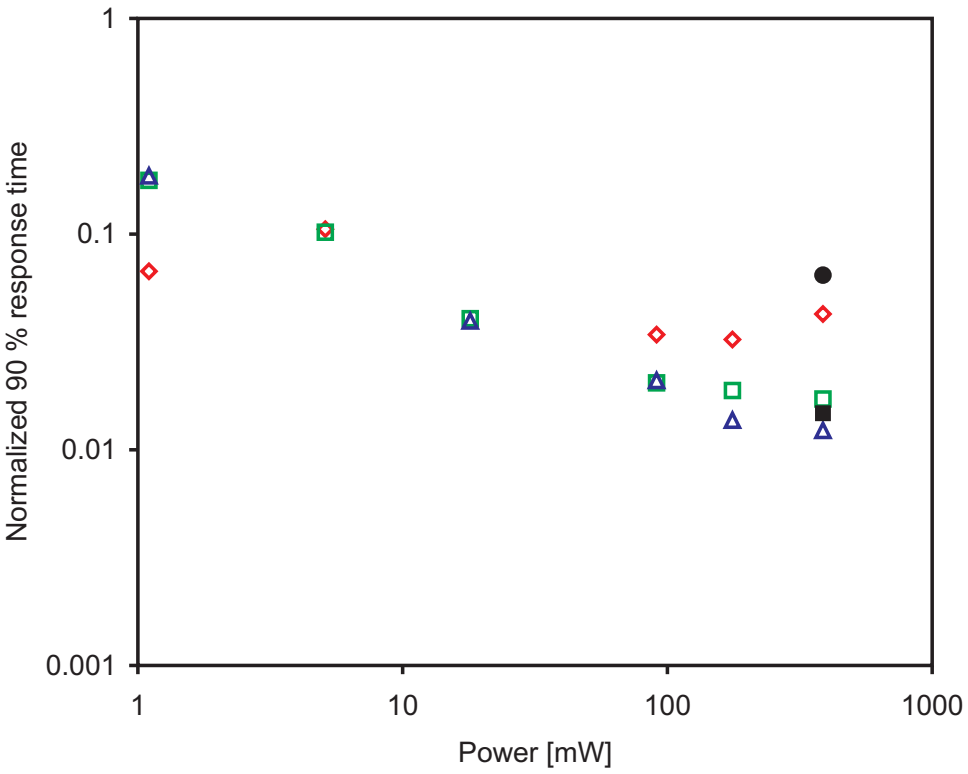

Figure 3.24: The variation with actuation power of the characteristic normalized sensor response time (based on 90 % of steady state when the jet power is zero) to gaseous ammonia for three different feed tube lengths: 17 (◊), 49 (□) and 120 cm (△). The power in x-axis (1.1, 5.1, 18, 91, 176, and 387 mW) was obtained by measuring the current for the jet at different AC voltages (6.6, 9.9, 13, 20, 26, and 37 Vrms). Two data points for "wet" ammonia gas are also included [H = 17 cm, V_{AC} = 37 V: F = 1500 Hz (•), and 720 Hz, (■)].

bubble flow meter (data not shown), the moving soap membrane formed bubbles inside, and the bubbles moved vigorously inside the membrane, and then the membrane collapsed. These results support the strong pumping effect of the jet as well as the mixing of the sample gases.

When the vapor above the ammonium hydroxide solution was used as the gas source and the exposure time was extended longer than 5 min, the response started to decrease and reached a lower plateau (data not shown). This is because the volume of the headspace vapor is finite, and the sample gas flux becomes limited by the vaporization of the solution. This decrease of the signal is observed during the first exposure to "wet" NH_3 in Figure 3.20a, which is not the sensor drift. In order to eliminate the non-constant gas concentration of the source, we have used ammonia gas tank with a needle valve as a continuous gas source. In this case, the sensor response kept a steady value even with extended exposure times (Figures 3.21a and 3.23a). Nevertheless, both types of gas sources are valid for testing real applications.

As shown in Figure 3.8a, the jet cell in combination with a three-way (or multi-way) valve enables to introduce two gas lines (or more) into a single sensing device. This system can be applied to many situations. It is, for instance, possible to examine and compare several gases by switching between the lines (differential sensing) to check before and after a process (e.g. filtering, cleaning, or catalytic converting), and to give an alarm when the process ceases to work properly (e.g. a filter change alarm). It is also possible to connect one of the gas lines to a background (carrier) gas, or a known concentration gas source (reservoir delivery) to refresh or recalibrate the gas sensors for long-term operation. These gases can be stored in a small pressurized gas cartridge due to the small volume of the gas required for the sensors. This application will solve the notorious baseline drift of the gas sensors.

3.4 Conclusions

This chapter focused on significant performance improvement in the response of chemical gas sensors by adding "sniffing" functionality to deliver sample gases to the sensor and

induce small-scale fluid motions near the surface of the sensor to overcome the diffusion-limited mass transfer at the surface of the sensing element (Cell 05). The small-scale jet-induced mixing and faster apparent diffusion (D_{app}) through the film in a closed system were also studied with Cell 02. This functionality was demonstrated by using an integrated, millimeter-scale active fluidic actuator based on synthetic jet technology which can be also used to deliver a flushing gas to clean or calibrate the sensor in long-term operation and thereby mitigate the baseline drift of gas sensors. The integration with the sensor is quite straightforward and is facilitated by the fact that synthetic jets can be (and have been) realized using conventional microfabrication technologies.

In the present implementation, a jet actuator impinges normal to the surface of a gas sensor that is placed several orifice widths away. The formation of the jet induces a low-pressure domain in the vicinity of the orifice and thereby draws sample gas through an integrated conduit (that may be thought of as a "nose"). The sample gas is transported by the jet and impinges on the embedded sensor. The volume flow rate of the sample gas can be easily regulated by the amplitude of the diaphragm motion. The crucial element of this new approach is that it eliminates the long transport time that is typically associated with diffusion of the sample gas towards the surface of the sensor. The characteristic dimensions of the jet are designed to scale with the active element of the sensor for optimal coverage and sensitivity, which are discussed in Chapter 4.

This chapter demonstrated that the integrated gas sampling and mixing functionality by fluidic actuation significantly improved the chemical response times of the sensor system with either gas emission from a spilled volatile solution or the leak of pressurized gas to the atmosphere. It was shown that in the presence of the jet the response time of the sensor was remarkably faster by about two orders of magnitude (20 compared to 1800 seconds) for the gas sniffing and three times faster for the gas mixing, and the D_{app} became twice larger.

CHAPTER IV

CONTINUOUS MONITORING OF FILTER PERFORMANCE USING JET-ASSISTED CHEMFET ARRAY

4.1 Introduction

In Chapter 3 the "sniffing" functionality integrated into the gas sensing system has shown that the sensor response times are two orders of magnitude faster than the ones without the jet-assisted gas sampling [61]. The gas sniffing mechanism using the synthetic jet was already explained in Chapter 3. In brief, the jets are produced by the periodic expulsion- and suction-motions of a diaphragm forcing the fluid through the orifice in Figure 4.1A. These jets are inherently zero net mass and do not need external gas supply like the "conventional" gas flow through cell system (Figure 4.1B).

An advantage of the synthetic jet is to be able to induce directionally and spatially controlled flow field that combines sink-like entrainment of ambient fluid towards the jet orifice and source-like ejection of that fluid towards a desired target (Figure 4.1A). Furthermore use of the synthetic jet is a significant advantage compared with the conventional gas flow through cell system (Figure 4.1B) where the cell has to be completely filled with the gas, which is normally more than enough just for chemical sensing.

In this chapter, the initial attempt for the use of the jet is concentrated on the continuous monitoring of the gas filter performance to be able to indicate the need for its exchange.

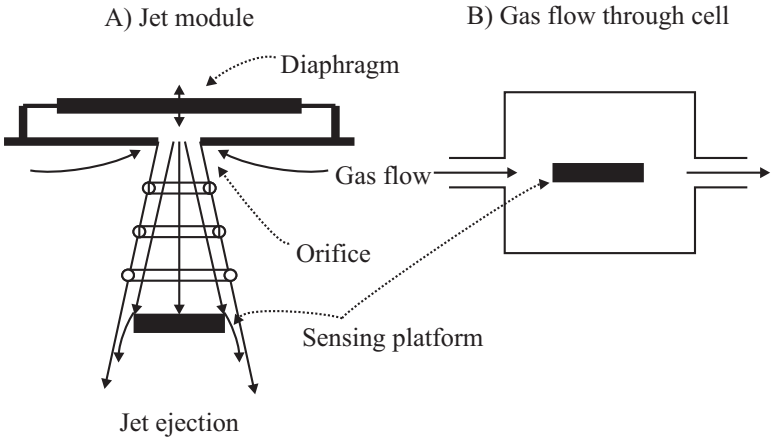

Figure 4.1: Schematics of (A) the synthetic jet assisted gas sampling system and (B) conventional gas flow through cell system. The ejected jets impinge on the sensing platform surface for local delivery of the sampled gas. The excess gas flows downward as indicated by the arrows.

4.2 Experimental Section

4.2.1 Gas Sensor Array

The GT03 sensing platform (Figure 4.2) was used as the array of gas sensors [62]. The platform has eight identical modules, each of which can be used in either the chemFET (chemically sensitive Field Effect Transistor) mode, chemiresistor mode, or OFET (organic Field Effect Transistor) mode after depositing chemically sensitive and electrically conductive materials (Figure 4.2) depending on the external circuitry connected to the platform [62].

Each module (500 x 400 μm) is separated by micro-structured wells [16] facilitating deposition of different sensing materials; the selectable modes of the sensing operation and the array structure allow obtaining diverse chemical information on the gases of interest. In this chapter, however, all the eight modules were used in the chemFET mode with the same sensing material, polyaniline (PANI) film doped with camphorsulfonic acid (CSA). The concentration of PANI + CSA in formic acid solution was 2.5 mg/mL, and the drop-cast film was UV-treated (254 nm) for 90 min to improve the long-term stability of the sensor baselines [63] as described in Chapter 1. The gas sensing responses of the eight chemFETs were measured as a change in the gate voltage with a constant drain-source

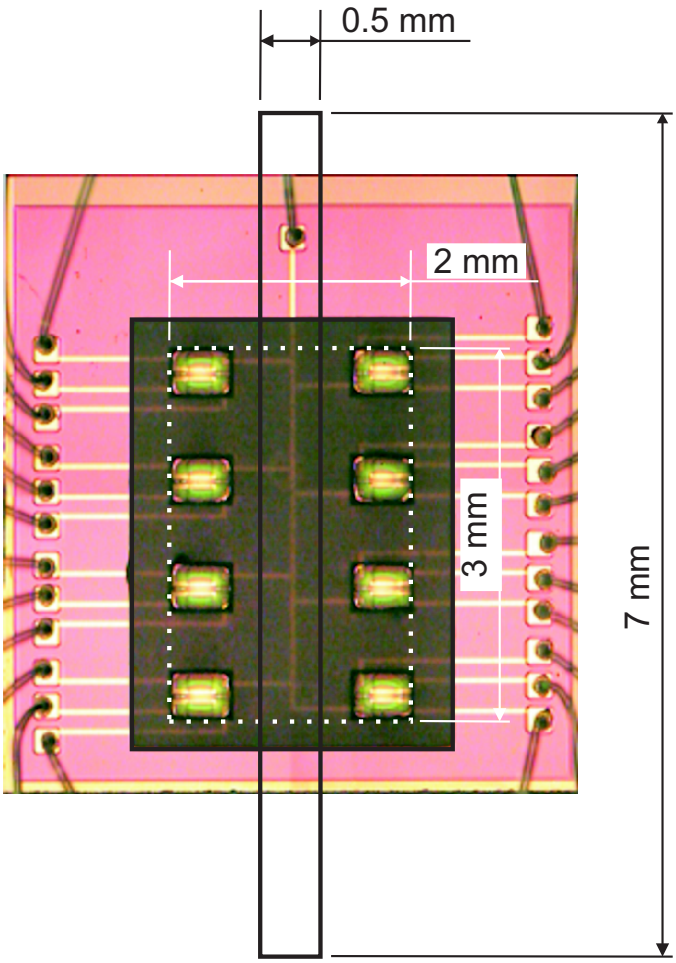

Figure 4.2: Photograph of the GT03 platform used for gas sensing. The platform constitutes eight identical sensing modules, which can be used either as chemFET, chemiresistor, or OFET (organic Field Effect Transistor) mode. In the center of each modules is seen the drop-cast conducting polymer, PANI·CSA, as gate conductor. The modules (Cell 05) are numbered counterclockwise from top left. The overlaid rectangle (0.5 x 7 mm) indicates the orifice size of the jet module placed above the sensing platform.

current of 0.2 mA in the source-follower configuration as shown in Figure 3.7c [13, 61].

In addition to the gas exposure experiments, basic characteristics of the individual eight modules were examined with a Semiconductor Parameter Analyzer (HP 4155A). The threshold voltages (V_T) for chemFETs were determined by measuring drain-source current versus gate voltage, V_G, from -1 to 5 V while keeping V_D constant at 5 V. The film resistances were obtained by measuring the current between the contacts while scanning the voltage from 0 to 1 V [63].

4.2.2 Jet Actuator Module

The detailed design of the synthetic jet module (Cell 05) was already reported in Section 3.2.1 and Reference [61]. The rectangular orifice and sensing platform were placed so that the long sides of both the orifice (0.5 x 7 mm) and the active sensing area (2 x 3 mm) were parallel to each other as indicated in Figure 4.2. The distance between the orifice (the exit of the jet) and the surface of the sensing platform was 4 mm. The distance was determined based on the Schlieren image of the ejected synthetic jet of a similar sized orifice (0.5 x 7.5 mm) in Figure 4.3 from Reference [53]; at a distance of 4 mm, the jet spreads from the size of the short side of the orifice (0.5 mm) to ca. 3 mm, which is large enough to cover the short side of the active sensing area (2 mm).

4.2.3 "Conventional" Gas Delivery System

To deliver ammonia gas of controlled concentrations to the sensor array, an Environics 4000S (Environics, Inc.) was used with a home-made stainless steel gas flow through cell (the dead volume of the cell is ca. 1.2 cm^3) as shown in Figure 4.4. The gas flow rate through the cell was kept at 100 cm^3/s by the mass flow controller. The ammonia concentrations were varied by changing the flow rates of the mass flow controllers connected to the air (Airgas) and the ammonia (5.14 %, Matheson) gas tanks. The flow was programmed with the Environics Series 4000 software to deliver ammonia concentration changes from 0 to 64, 257, 612, 2142 and back to 0 ppm.

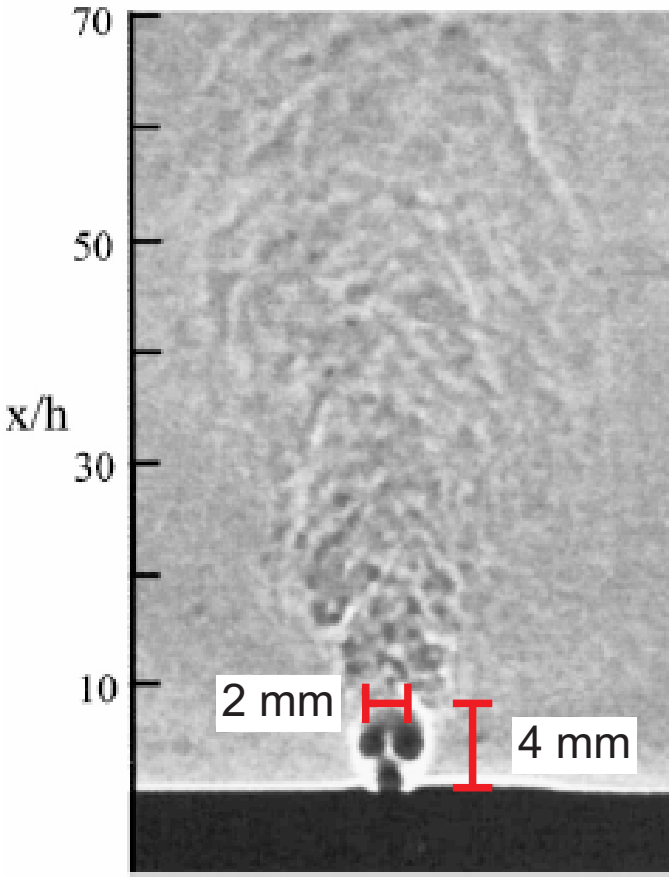

Figure 4.3: Schlieren image of the synthetic jet from an orifice with h = 0.5 x 75 mm.

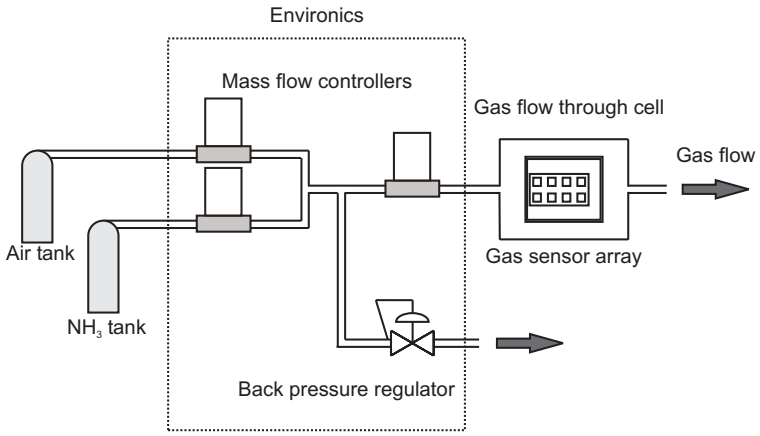

Figure 4.4: "Conventional" gas delivery system. The eight chemFETs are placed in the gas flow through cell after the Environics.

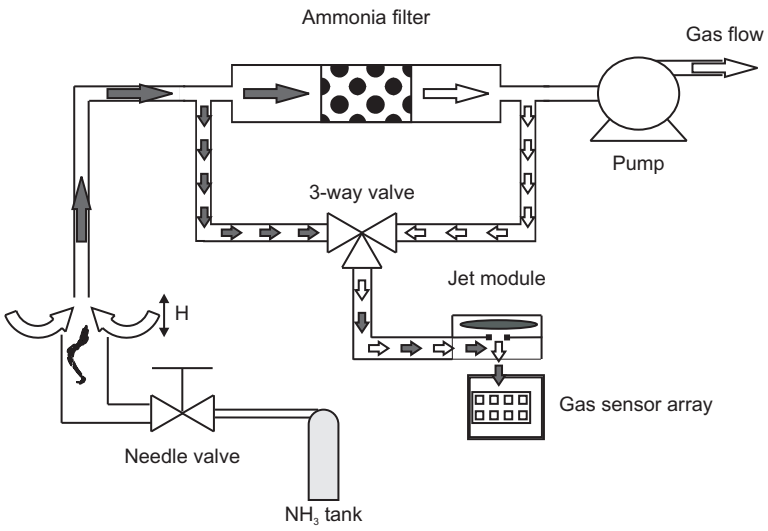

Figure 4.5: Experimental setup for testing filter performance with synthetic jet. The main flow, indicated by the large arrows, was driven by the pump. The flow toward the jet module, indicated by the small arrows, was sampled by the jet module. The dark and white arrows show that the gas contains ammonia before filtering and no (or less) ammonia after filtering, respectively. The ammonia from the tank was introduced to the main flow (distance between the main flow inlet and ammonia gas exit, H = ca. 1.0 mm).

4.2.4 Gas Filter System

Figure 4.5 shows the experimental setup for monitoring the gas filter performance using Cell 05. The main flow (indicated by the large arrows) passing through the filter zeolite was driven by a pump. The zeolite (5$\mathring{A}$, Fisher Science) was used after heating at 150 °C for 1hour in oven, then placed in a 2.5 cm-inner diameter glass tube, sandwiched by porous supports on both sides, and cooled down at room temperature for 1 hour with the main flow driven by the pump. The amount of zeolite was changed (2g, 4g, and 6 g) to observe the onset times of the break-through of the filter (filter life times). The ammonia gas released from the gas tank (5.14 %, Matheson) through a needle valve was introduced into the main flow. The dark arrows indicate the gas contains ammonia, whereas the white arrows show the gas is clean after the filter. The distance between the main flow inlet port and the ammonia gas exit (H) was kept about 1 mm. The normal laboratory air was used as a carrier gas. The pump flow rate was adjusted to be 460 cm^3/s when without zeolite.

To monitor the difference of the ammonia concentrations before and after the filter, a three-way valve (ASCO) was switched between the two lines at a switching interval of 5 min

unless otherwise mentioned. Sniffing of the gas to the active sensing area was conducted with oscillating frequency at 720 Hz and supplied AC voltage at 20 Vrms. The volume flow rate and power required for the jet assisted sampling under this condition were 35 cm^3/s and 91 mW, respectively. The onset of the break-through of the filter was monitored by comparing the sensors' responses before and after the filter; that is, as the filter loses its capacity, the sensor response difference before and after the filter becomes smaller, and eventually becomes zero. We also tested the filter recovering process by passing the carrier gas alone after the break-through of the filter.

4.2.5 2-D Mapping of the Sensor Array Responses to the Synthetic Jet

To assess the two-dimensional concentration distribution of ammonia gas at the active sensing area, the sensing platform was displaced from the center line of the orifice in the x direction (see Figure 4.11c), the direction parallel to the short side of the orifice, and the responses of the eight chemFETs were obtained. The tested offset distances were 0 and 1.4 mm.

4.3 Results and Discussion

4.3.1 Physical Characteristics of the Sensor Array

The averages of the measured V_T values of chemFETs and film resistances of chemiresistors were 844 mV (standard deviation $\sigma = 29$ mV) and 5.42 MΩ ($\sigma = 1.22$ MΩ), respectively (Table 4.1). Figure 4.6 shows an example of chemFET measurement of (A) drain-source current versus gate voltage with a constant drain voltage of 7 V and (B) drain-source current versus drain voltage. The standard deviation of the V_T values with respect to its average value is smaller compared to the one of the film resistance. This is because the polymer solution was dispensed onto each module with a capillary glass, which is not an accurate way to deliver a controlled volume of the solution and to obtain uniform film thicknesses. The film resistance depends on the film thickness, resulting in the larger standard deviation of the film resistances compared with the one of the V_Ts, which are governed by the electronic properties of the film in the space charge region; that is, as far as the film is thicker than the space charge region (ca. 500 nm for a doped PANI [38]) the V_T is less affected by

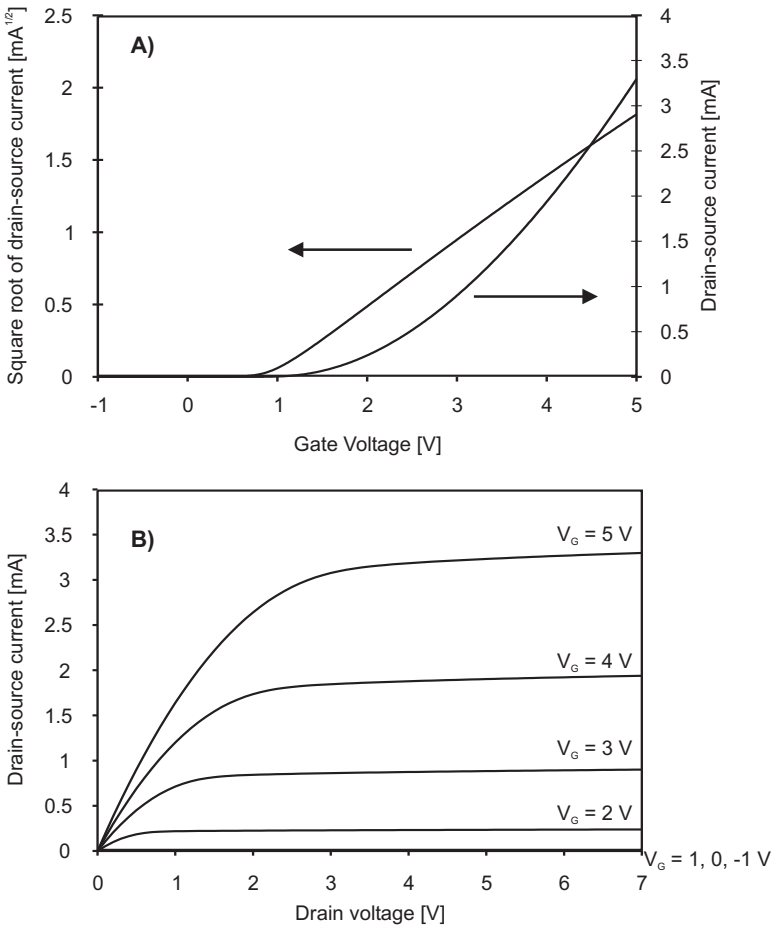

Figure 4.6: Example of chemFET measurement of (A) drain-source current versus gate voltage (the drain voltage was kept at 7 V.) and (B) drain-source current versus drain voltage.

the film thickness variation. This problem can be solved by, for example, using the ink-jet dispensing technology to cast a precise amount of polymer solutions [64].

4.3.2 Calibration Curves of the Sensors using the "Conventional" Gas Delivery System

Using the gas flow through cell system shown in Figure 4.4, the responses of the eight chemFETs to ammonia gas and the calibration curves were obtained (Figures 4.7A and B). The gate voltage changes show similar responses among the eight chemFETs. The calibration curve of chemFET is linearly proportional to the logarithm of the ammonia concentration [48]. At the highest, however, concentration (2142 ppm) the data point deviates from the linear approximation due to the saturation of the sensor signal; that is,

this concentration region is outside the dynamic range of the sensor detection [12]. For that reason, the calculation of the sensitivities was conducted without the highest concentration point and the obtained sensitivities of the eight chemFETs are shown in Table 4.1. The small standard deviation of the sensitivities results from the facts that the standard deviation of the V_T values is small, and the chemFET sensitivity varies based on the V_T [48].

Table 4.1: Correlation between the threshold voltages and the film resistances of the PANI·CSA films cast on the GT03 platform and the sensitivity of the chemFETs to ammonia gas using the experimental setup shown in Figure 4.4.

Module	V_T [mV]	R [MΩ]	Sensitivity [mV/decade]
CH1	924	4.96	-28.0
CH2	851	6.73	-28.2
CH3	851	6.98	-28.8
CH4	796	4.19	-27.6
CH5	838	4.46	-28.5
CH6	832	6.39	-28.7
CH7	849	4.43	-28.3
CH8	893	4.72	-27.9
Average	844 ± 29	5.42 ± 1.22	-28.3 ± 0.427

4.3.3 Monitoring of Filter Performance

Figure 4.8A shows responses of a single chemFET to the gas sampled before and after ammonia filtering using different amounts of zeolite: (a) 2, (b) 4, and (c) 6 g. The measurements were started at t = 0 min and the ammonia gas was introduced to the main flow through the needle valve at t = 0.3 min. The time trace of the three-way valve control sequence is shown in Figure 4.8A-d; when the supplied DC voltage to the three-way valve is low, the jet module samples the gas before the filter and when high, after the filter. All the measurements were started with the three-way valve switched to the gas line before the filter. The ammonia gas tank supplies the constant concentration into the main flow. When, thereby, the three-way valve is switched to the gas before the filter, the gate voltage change should show a constant value with time. The gradual upward shift of the gate voltage change measured with time in Figure 4.8A-a suggests the sensor baseline drift. On the other hand, the decrease of the gate voltage change after the filter indicates the onset of the break-through of the filter, which eventually becomes same as the gate voltage change

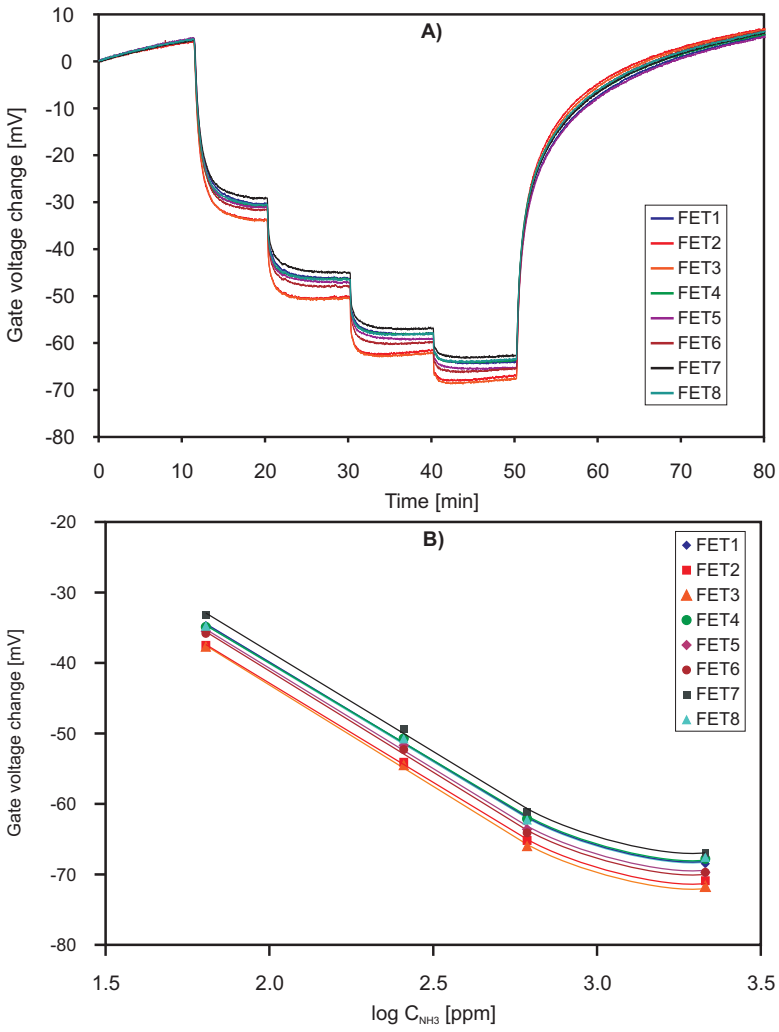

Figure 4.7: (A). Responses of an array of the eight chemFET sensors modified with PANI·CSA film. The concentration steps of the ammonia gas are from 0 to 64, 257, 612, 2142 and 0 ppm. (B). Calibration curves of eight chemFETs to ammonia gas (64, 257, 612, and 2142 ppm). To obtain the sensitivities, the highest concentration point was discarded.

before the filter. For example the onset of the break-through of the filter in Figure 4.8A-c starts after ca. 110 min.

Figure 4.8B is the same data but the responses are shown as the gate voltage difference, which is the gate voltage after the filtering subtracted by the previous gate voltage before the filtering. Both of the points for the subtraction were chosen immediately before switching the three-way valve. An advantage of plotting gate voltage difference is that the ammonia concentration removed by the filter can be obtained without the effects of the sensor baseline drifts (compare Figures 4.8A-a and 4.8B-a). It is observed the onset time of the filter break-though varies with the amount of zeolite. Figure 4.8B contains all the eight responses; all of them show similar plots suggesting that the jet is impinging on the active sensing area evenly as designed.

Figures 4.9A and B show the responses with the same amount of zeolite (4 g) but different switching intervals of the three-way valve: (a) 1 min, (b) 5 min, and (c) 10 min. All of the three data show the similar lifetimes of the filter. The 1 min switching interval (Figure 4.9A-a) shows smaller amplitude of the gate voltage change because the sensor response time is comparable to the switching interval and the sensor is still in the transition state (memory effect). However the break-through time of the 1 min switching interval is comparable to the ones in Figures 4.9A-b and c, indicating that the system can be used for the gas sensor whose response time is slower that the switching interval to obtain the same information.

Figure 4.10 shows two sets of filtering of the ammonia gas and subsequent recovering of the filter. The ammonia gas was introduced when t = 0 to 180 min and t = 760 to 850 min. In both of the time periods, the decrease of the gate voltage difference was observed, which suggests the decrease of the filter capacity. On the other hand, in the filter recovering process (t = 180 to 760 min and t = 850 to 1440 min), the gate voltage difference was negative, indicating the air after the filter contains more ammonia, and became close to zero, which means the filter was cleaned by passing the air through the filter.

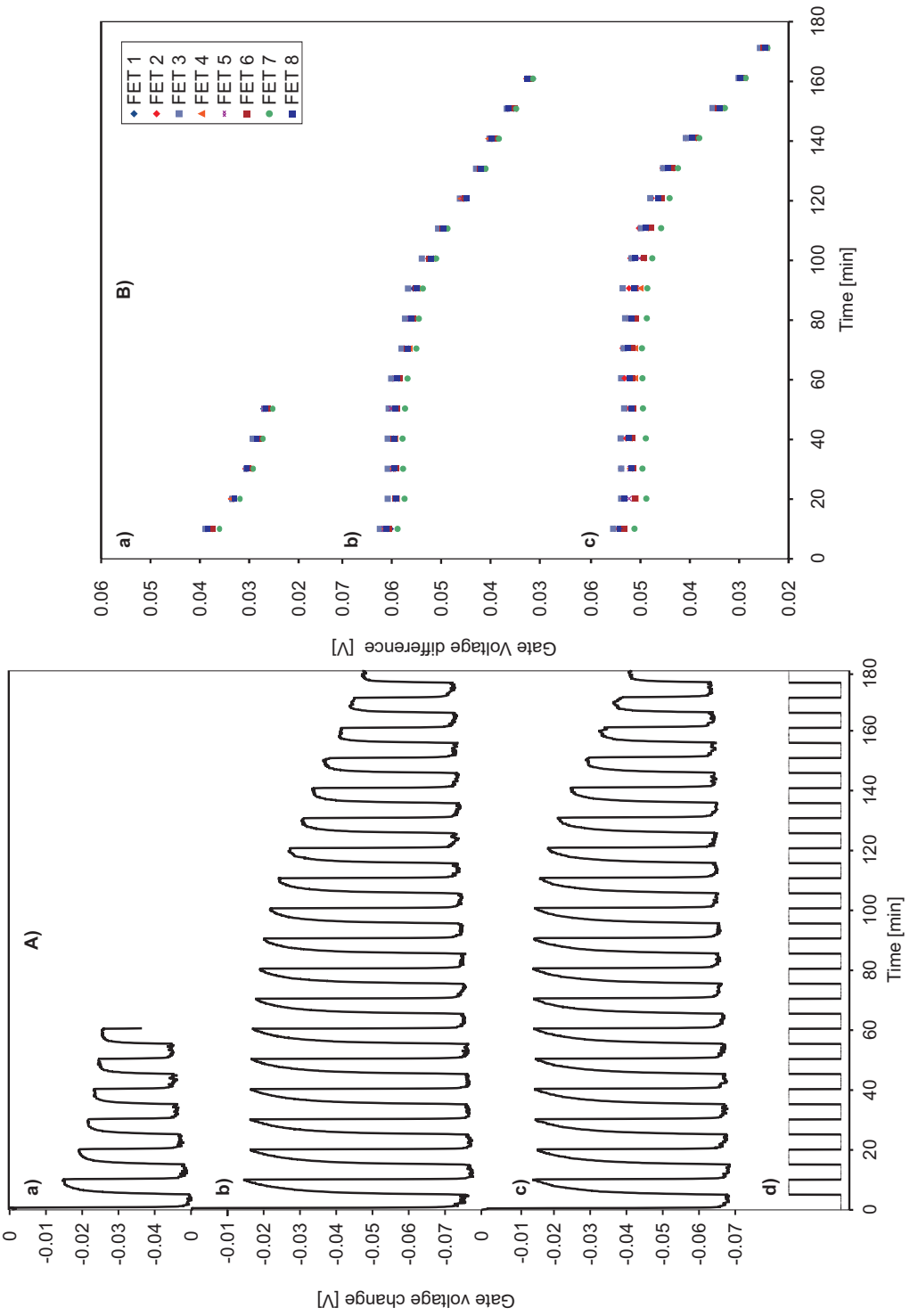

Figure 4.8: (A). Responses of a single chemFET to the gas before and after ammonia filtering using different amounts of zeolite: (a) 2 g, (b) 4 g, and (c) 6 g. The time trace of the three-way valve sequence is shown in (d). When the supplied voltage to the valve is low, the jet module samples the gas before the filter; and when high, after the filter. (B). Gate voltage difference before and after the filter of the array of the chemical sensing modules with different amounts of zeolite: (a) 2 g, (b) 4 g, and (c) 6 g. The gate voltage difference was obtained by subtracting the gate voltage change before the filter from the following one after the filter.

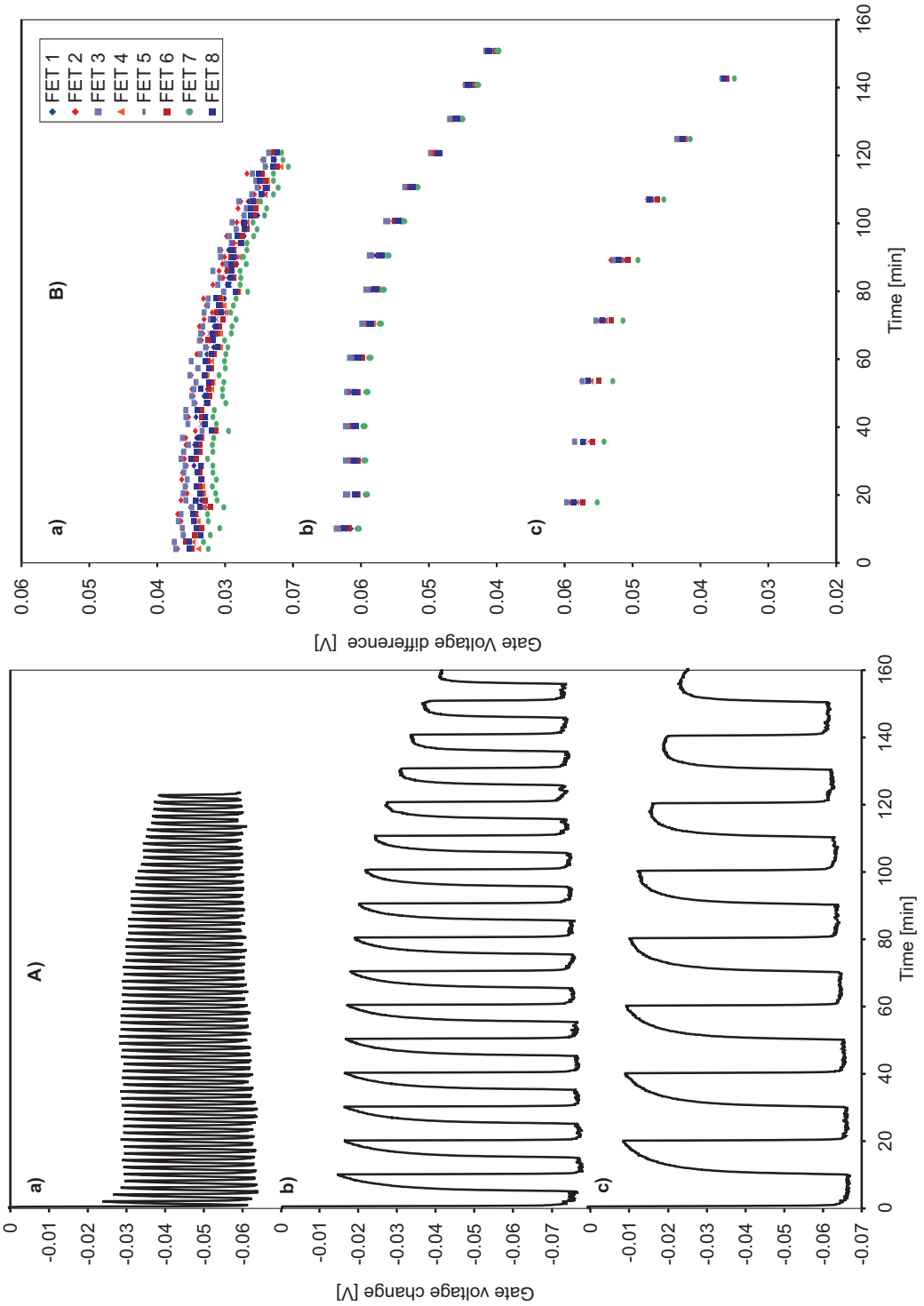

Figure 4.9: Responses of a single chemFET to the gas before and after ammonia filtering with different switching intervals: (a) 1 min, (b) 5 min, and (c) 10 min. (B). Gate voltage difference before and after the filter of the array of the chemFETs with different switching intervals: (a) 1 min, (b) 5 min, and (c) 10 min.

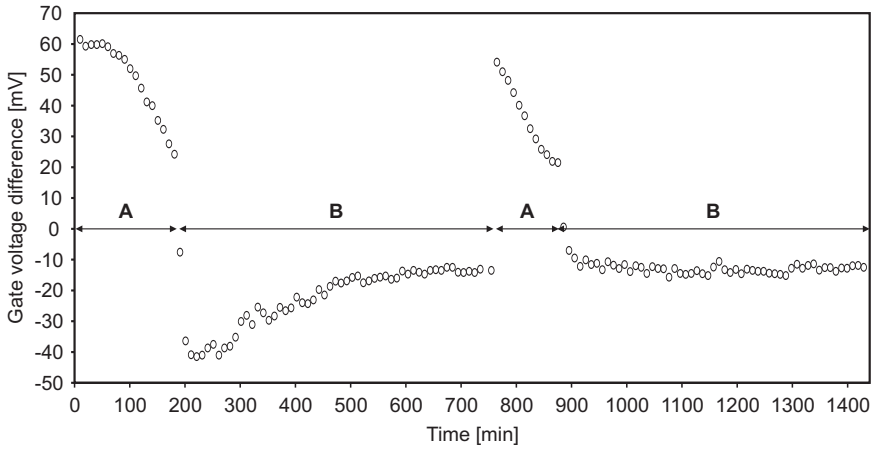

Figure 4.10: Control of the filter operation during the filtering process (A) and the recovery process (B). When the main gas flow contains the ammonia at t = 0 to 180 min and t = 760 to 850 min (filtering process), the gate voltage difference values are positive indicating less ammonia after the filter. When the gate voltage difference is negative at t = 180 to 760 min and t = 850 to 1440 min (recovery process), the filter was cleaned by passing air without ammonia through the filter and more ammonia is coming after the filter.

4.3.4 2-D Mapping of the Sensor Array Responses to the Synthetic Jet

The sensitivities of the sensors are shown very similar to each other (Table 4.1). However, for more precise investigation of the two-dimensional distribution of the jet, the responses of the sensors were normalized using the sensitivity values. The gate voltage of a chemFET is linearly proportional to the logarithm of the gas concentration [65]:

$$V_G = mlog_{10}C + n \tag{4.1}$$

where V_G is the gate voltage in mV, C is the ammonia gas concentration in ppm, m is the sensitivity of the chemFET in mV/decade, n is the constant. Subscripts a and b denote "after" and "before" the filtering, respectively. The equation above is rewritten in terms of the gas removal efficiency as follows:

$$(C_b - C_a)/C_a = 10^{\frac{-(V_a - V_b)}{m}} - 1 \tag{4.2}$$

where V_a - V_b is the gate voltage difference shown in Figures 4.8B and 4.9B. For the two-dimensional mapping, C_b and C_a were obtained when t = 5 min and t = 10 min, respectively.

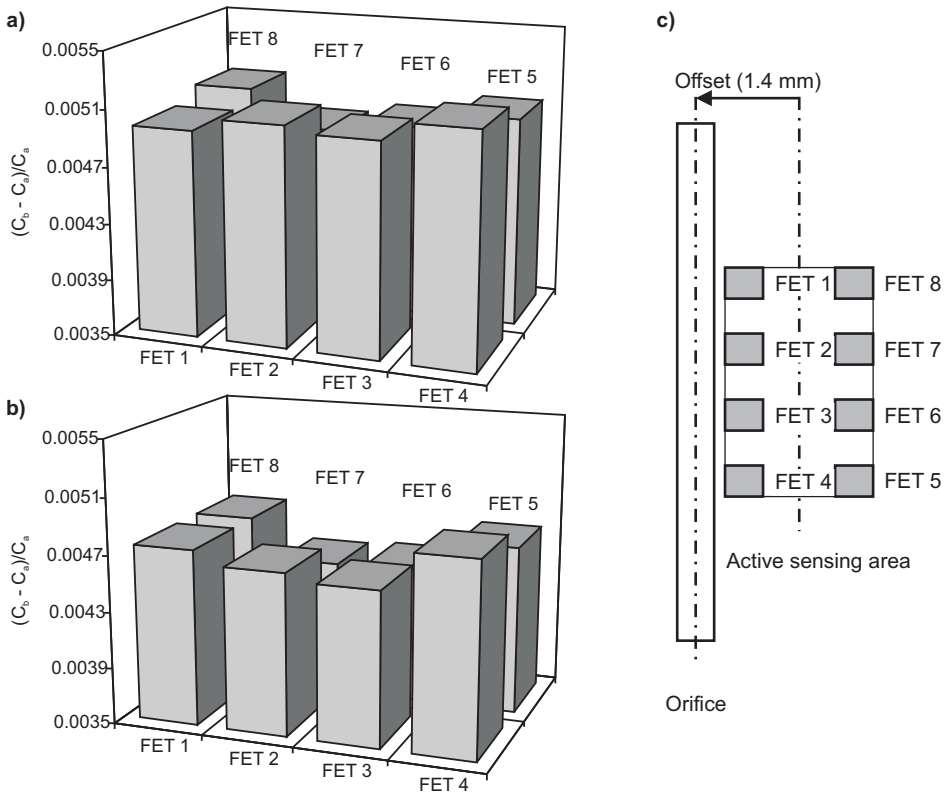

Figure 4.11: Mapping of the sensor array responses with different offset values: (a) 0 mm, (b) 1.4 mm. Schematic (c) of the active sensing area and the orifice with 1.4 mm offset.

Figures 4.11a and b show when the offset is 0 mm and 1.4 mm, respectively. Figure 4.11c shows an overlaid schematic showing the active sensing area and the orifice when the offset is 1.4 mm. The average of the gas removal efficiencies (5.0 x 10^{-3}) when the offset is 0 mm is higher is than the one (4.7 x 10^{-3}) when 1.4 mm. Whereas, the standard deviation when 0 mm is σ = 1.2 x 10^{-4} and when 1.4 mm is σ = 1.5 x 10^{-4}. The higher average vale and smaller standard deviation when 0 mm offset may suggest that the impinging jet delivers uniform gas environments at the center of the active sensing area, where a stagnation point of the jet occurs. When the offset exists, the sensor array was displaced form the stagnation point and therefore the smaller gas removal efficiencies (smaller gas concentrations) and the larger standard deviation of the eight chemFETs were observed. In Figure 4.11b is seen a slight decrease of the gas removal efficiencies of the right column chemFETs (FET 5 to 8) with respect to the left column chemFETs (FET 1 to 4).

Figure 4.12 summarizes expected sensor signal changes (gate voltage changes) before

and after a gas filter (Figure 4.12A) as well as all the observed gate voltage changes while monitoring the filter performance (Figure 4.12B). Figure 4.12A-a shows that the main flow does not contain detectable gas which is to be removed by the filter. Figures 4.12A-b and c represent that the main flow contains the detectable agent to be removed by the filter and the filter is before the break-through point (Figure 4.12A-b), and the filter has the onset of the break-through of the filter (Figure 4.12A-c). Figure 4.12A-d shows the baseline drift of the sensor in the presence of the detectable agent before the break-through point, whereas, Figure 4.12A-e shows loss of sensitivity of the sensor or decrease of concentration of the agent at the main flow inlet. In the actual sensing experiments (a), (b), (c) and (d) were observed as shown in Figure 4.12B side by side. Figure 4.12B-d shows the baseline drift as well as the onset of the break-through of the filter. During the whole experiments we did not observed any loss of sensitivity of the sensors. However, in some experiment (Figure 4.8B-c), FET 1 did not turn on presumably due to bad connection of the electric cables.

4.4 Conclusions

The gas sensing system integrated with the gas sampling functionality can be applied to monitor a gas filter performance continuously. The two-dimensional distribution of the gas concentrations showed that the synthetic jet covers the active sensing area in an effective way so that the sampling volume for sensing is significantly reduced compared with the conventional gas flow cell system. It is possible that this system can be applied to monitor the state of the air purification units installed in air delivery systems for public spaces.

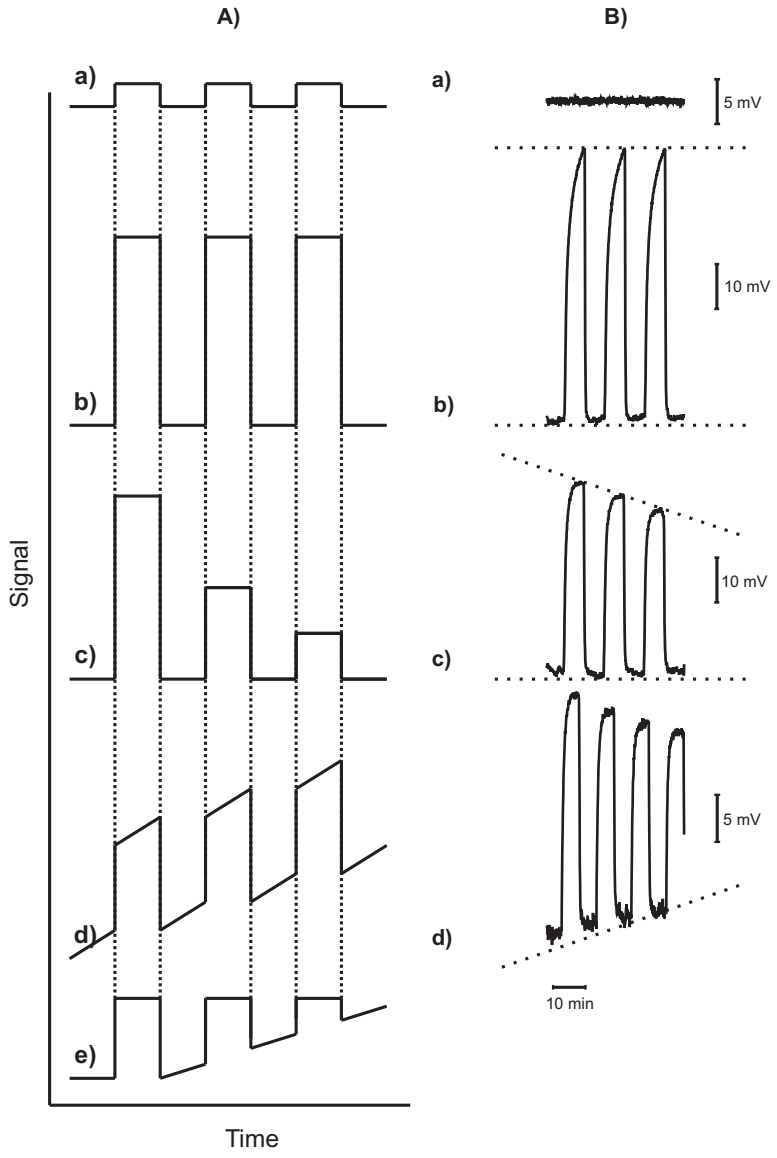

Figure 4.12: Expected sensor signal changes (gate voltage changes) before and after a gas filter indicating: (a) normal operation of the system (no detectable gas), (b) presence of detectable agent to be removed by the filter, (c) onset of the break-through of the filter, (d) baseline drift of the sensor in the presence of detectable agent, (e) loss of sensitivity (or decrease of concentration of the agent). (B). Actual observed gate voltage changes: (a) normal operation without ammonia gas, (b) presence of ammonia gas filtered by zeolite, (c) onset of the filter break-through indicating that the filter needs to be exchanged, (d) baseline drift as well as filter break-through.

CHAPTER V

FUTURE WORK

The future work should continue to improve the physical and chemical properties of the sensing layers and the performance of the newly designed gas sniffing system.

5.1 Sensitive Layer

- PANI Layer Thickness

  The optimum design of a sensor requires taking into account a number of factors such as detection limit, detection speed, long -term stability, and so on. The detection limit and detection speed are controlled by the thickness of the sensitive layer. It is generally known that the thickness should be larger than the space charge region (ca. 500 nm) that is formed at the interface between the PANI·CSA and the insulator. The thinner the film thickness is, the less sensitive the sensor becomes and the faster the sensor response time becomes. It is proposed to reduce the thickness of the layer from 1000 nm to 500 nm by diluting the PANI and CSA solution with formic acid (v/v = 1:1) for the drop-casting.

- Selectivity

  To obtain better selectivities of the sensors modified with metal/metal oxide clusters incorporated in the PANI sensitive films, it is necessary to optimized the conditions for the cluster depositions e.g., the type of acid used for activation of the film, counter anion of the metal salt, the applied potential for the activation of the PANI films. The characterization of the clusters formed in the PANI films will be performed using scanning electron microscopy (SEM) and/or X-ray photo-electron spectroscopy (XPS). Further an introduction of gold clusters [30, 66–69] as binding sites will be tested and mixed gas exposures will be performed with the help of the chemometrics

to identify the mixtures.

- Long-term Stability

  In order to improve the long-term stability of the chemFETs and chemiresistors, it is proposed to test the influence of the UV treatment on the (metal/metal oxide)*PANI·CSA composite films.

- Microscopic Electrochemistry

  The activation of the eight PANI·CSA films on the same platform was conducted at the same time in the same solution. It will be more beneficial to do the activation and cluster deposition processes module by module. For this purpose, microscopic electrochemistry in the individual 500 x 400 μm wells will be applied [70].

5.2 Gas Sniffing System

- Open Space Sniffing

  The distance of the gas intake port and the gas source can be changed as shown in Figure 5.1. It will be necessary to optimize the jet performance conditions e.g., frequency and applied AC voltage, using the same cell (Cell 05). Based on the results a new cell should be designed.

- Continuous Re-calibration of the System

  It was proposed that the jet system can solve the notorious baseline drift of the gas sensors. It is possible to realize the concept by using the current setup, assuming the ammonia gas tank is the calibration gas.

- Miniaturization

  The miniaturization of the jet module can be performed using the MEMS technology.

- Other Applications of the System

  The high potential of the gas sniffing system will be examined in other applications such as air quality monitoring with self-calibration system or liquid sample delivery system.

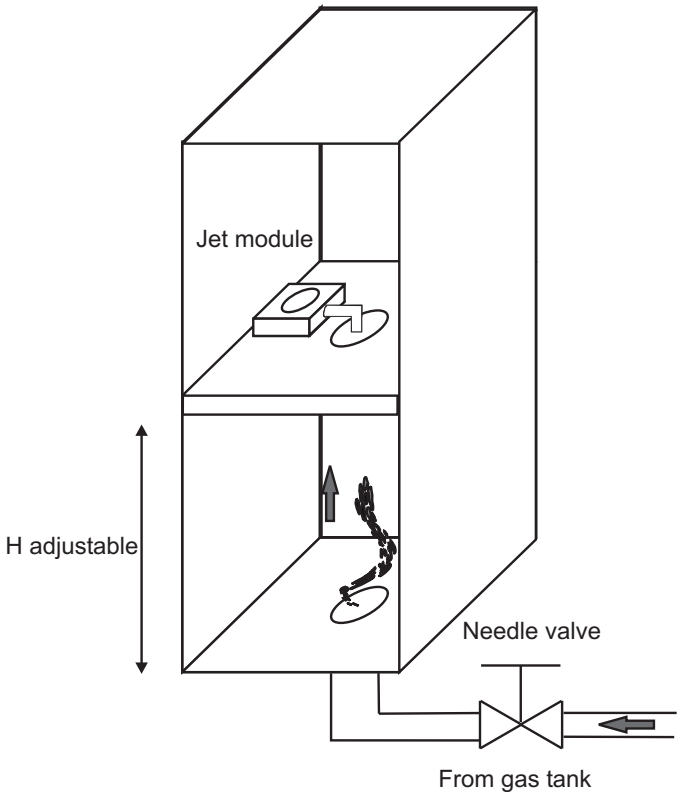

Figure 5.1: Experimental setup for open space gas sniffing. The size of the box could be 1 x 1 x 1 m and the distance between the gas intake port and the source of the gas is adjustable.

REFERENCES

[1] Y. Cao, J. J. Qiu, and P. Smith, "Effect of solvents and cosolvents on the processibility or polyaniline .1. solubility and conductivity studies," *Synthetic Met*, vol. 69, pp. 187–190, 1995.

[2] P. M. Mcmanus, R. J. Cushman, and S. C. Yang, "Influence of oxidation and protonation on the electrical-conductivity of polyaniline," *J Phys Chem*, vol. 91, pp. 744–747, 1987.

[3] M. Zagorska, E. Taler, I. Kulszewicz-Bajer, A. Pron, and J. Niziol, "Conductive polyaniline-polyamide 6 blends processed from formic acid with improved stability against deprotonation," *J Appl Polym Sci*, vol. 73, pp. 1423–1426, 1999.

[4] W. Lu, A. G. Fadeev, B. H. Qi, E. Smela, B. R. Mattes, J. Ding, G. M. Spinks, J. Mazurkiewicz, D. Z. Zhou, G. G. Wallace, D. R. MacFarlane, S. A. Forsyth, and M. Forsyth, "Use of ionic liquids for pi-conjugated polymer electrochemical devices," *Science*, vol. 297, pp. 983–987, 2002.

[5] U. A. Sevil, O. Guven, and S. Suzer, "Spectroscopic investigation of onset and enhancement of electrical conductivity in pvc/pani composites and blends by gamma-ray or uv irradiation," *J Phys Chem B*, vol. 102, pp. 3902–3905, 1998.

[6] M. Wolszczak, J. Kroh, and M. M. Abdelhamid, "Some aspects of the radiation processing of conducting polymers," *Radiat Phys Chem*, vol. 45, pp. 71–78, 1995.

[7] M. Wolszczak, J. Kroh, and M. M. AbdelHamid, "Effect of ionizing radiation on polyaniline solutions," *Radiat Phys Chem*, vol. 47, pp. 859–867, 1996.

[8] J. A. Malmonge, A. Dhanabalan, A. Riul, R. M. Faria, and O. N. Oliveira, "Polyaniline mixed lb films exposed to x-rays," *Synthetic Met*, vol. 101, pp. 801–802, 1999.

[9] M. Wolszczak, J. Kroh, and M. M. AbdelHamid, "Effect of ionizing radiation on polyaniline solutions," *Radiat Phys Chem*, vol. 47, pp. 859–867, 1996.

[10] M. Angelopoulos, Y. H. Liao, B. Furman, and T. Graham, "Licl induced morphological changes in polyaniline base and their effect on the electronic properties of the doped form," *Macromolecules*, vol. 29, pp. 3046–3049, 1996.

[11] Y. N. Xia, J. M. Wiesinger, A. G. Macdiarmid, and A. J. Epstein, "Camphorsulfonic acid fully doped polyaniline emeraldine salt - conformations in different solvents studied by an ultraviolet-visible near-infrared spectroscopic method," *Chem Mater*, vol. 7, pp. 443–445, 1995.

[12] J. Janata, *Principles of Chemical Sensors*. New York: Plenum Press, 1989.

[13] B. J. Polk, J. A. Smith, S. P. DeWeerth, Z. P. Zhou, J. Janata, and K. Domansky, "Design of solid state array for simultaneous potentiometric and impedance sensing in gas phase," *Electroanal*, vol. 11, pp. 707–711, 1999.

[14] B. J. Polk, K. Potje-Kamloth, M. Josowicz, and J. Janata, "Role of protonic and charge transfer doping in solid-state polyaniline," *J Phys Chem B*, vol. 106, pp. 11 457–11 462, 2002.

[15] D. W. Hatchett, M. Josowicz, and J. Janata, "Comparison of chemically and electrochemically synthesized polyaniline films," *J Electrochem Soc*, vol. 146, pp. 4535–4538, 1999.

[16] H. Chen, F. L'Hereec, I. Sasaki, and J. Janata, "High-aspect ratio permanent photomask for solid-state chemical sensing array," *Thin Solid Films*, vol. 444, pp. 241–244, 2003.

[17] D. Chinn, J. Dubow, J. Li, J. Janata, and M. Josowicz, "Comparison of chemically and electrochemically prepared polyaniline films .2. optical-properties," *Chem Mater*, vol. 7, pp. 1510–1518, 1995.

[18] W. S. Huang and A. G. Macdiarmid, "Optical-properties of polyaniline," *Polymer*, vol. 34, pp. 1833–1845, 1993.

[19] X. M. Guo, R. E. Sturgeon, Z. Mester, and G. J. Gardner, "Vapor generation by uv irradiation for sample introduction with atomic spectrometry," *Anal Chem*, vol. 76, pp. 2401–2405, 2004.

[20] ——, "Uv vapor generation for determination of selenium by heated quartz tube atomic absorption spectrometry," *Anal Chem*, vol. 75, pp. 2092–2099, 2003.

[21] L. Khriachtchev, E. Macoas, M. Pettersson, and M. Rasanen, "Conformational memory in photodissociation of formic acid," *J Am Chem Soc*, vol. 124, pp. 10 994–10 995, 2002.

[22] J. Yano, K. Terayama, S. Yamasaki, and K. Aoki, "Logarithmic time dependence of the oxidative coloration of polyaniline film," *Electrochimica Acta*, vol. 44, pp. 337–343, 1998.

[23] J. Yano, K. Terayama, and S. Yamasaki, "White polyaniline as a time display: Reaction of polyaniline with gaseous oxygen," *Synthetic Met*, vol. 85, pp. 1381–1382, 1997.

[24] S. Stafstrom, B. Sjogren, and J. L. Bredas, "An indo/s-ci study of the photoinduced absorption-spectrum of polyemeraldine," *Synthetic Met*, vol. 29, pp. E219–E226, 1989.

[25] Y. Cao, "Spectroscopic studies of acceptor and donor doping of polyaniline in the emeraldine base and pernigraniline forms," *Synthetic Met*, vol. 35, pp. 319–332, 1990.

[26] K. G. Neoh, E. T. Kang, and K. L. Tan, "Spectroscopic studies of protonation, oxidation and light irradiation of polyaniline solutions," *Polymer*, vol. 33, pp. 2292–2298, 1992.

[27] D. Hatchett, M. Josowicz, and J. Janata, "Acid doping of polyaniline: Spectroscopic and electrochemical studies," *J Phys Chem B*, vol. 130, pp. 10 992–10 998, 1999.

[28] J. S. Tang, X. B. Jing, B. C. Wang, and F. S. Wang, "Infrared-spectra of soluble polyaniline," *Synthetic Met*, vol. 24, pp. 231–238, 1988.

[29] E. T. Kang, K. G. Neoh, and K. L. Tan, "Polyaniline: A polymer with many interesting intrinsic redox states," *Prog Polym Sci*, vol. 23, pp. 277–324, 1998.

[30] D. W. Hatchett, M. Josowicz, J. Janata, and D. R. Baer, "Electrochemical formation of au clusters in polyaniline," *Chem Mater*, vol. 11, pp. 2989–2994, 1999.

[31] W. Zheng, M. Angelopoulos, A. J. Epstein, and A. G. MacDiarmid, "Concentration dependence of aggregation of polyaniline in nmp solution and properties of resulting cast films," *Macromolecules*, vol. 30, pp. 7634–7637, 1997.

[32] S. J. Martin and G. C. Frye, "Polymer film characterization using quartz resonators," in *Proc. IEEE Ultrason. Symp.*, 1991, pp. 393–398.

[33] D. S. Ballantine, *Acoustic wave sensors: Theory, design, and physico-chemical applications*. San Diego: Academic Press, 1997.

[34] H. L. Bandey, S. J. Martin, R. W. Cernosek, and A. R. Hillman, "Modeling the responses of thickness-shear mode resonators under various loading conditions," *Anal Chem*, vol. 71, pp. 2205–2214, 1999.

[35] G. Sauerbrey, "Verwendung von schwingquarzen zur wagung dunner schichten und zur mikrowagung," *Z Phys*, vol. 155, pp. 206–222, 1959.

[36] M. A. M. Noel and P. A. Topart, "High-frequency impedance analysis of quartz-crystal microbalances .1. general-considerations," *Anal Chem*, vol. 66, pp. 484–491, 1994.

[37] D. Chinn, J. Dubow, M. Liess, M. Josowicz, and J. Janata, "Comparison of chemically and electrochemically prepared polyaniline films .1. electrical-properties," *Chem Mater*, vol. 7, pp. 1504–1509, 1995.

[38] J. Langmaier and J. Janata, "Sensitive layer for electrochemical detection of hydrogencyanide," *Anal Chem*, vol. 64, pp. 523–527, 1992.

[39] K. G. Neoh, E. T. Kang, S. H. Khor, and K. L. Tan, "Stability studies of polyaniline," *Polym Degrad Stabil*, vol. 27, pp. 107–117, 1990.

[40] M. Angelopoulos, A. Ray, A. G. Macdiarmid, and A. J. Epstein, "Polyaniline - processability from aqueous-solutions and effect of water-vapor on conductivity," *Synthetic Met*, vol. 21, pp. 21–30, 1987.

[41] K. Domansky, J. Li, and J. Janata, "Selective doping of chemically sensitive layers on a multisensing chip," *J Electrochem Soc*, vol. 144, pp. L75–L78, 1997.

[42] J. Huang, S. Virji, B. H. Weiller, and R. B. Kaner, "Nanostructured polyaniline sensors," *Chem-Eur J*, vol. 10, pp. 1315–1319, 2004.

[43] S. Virji, J. X. Huang, R. B. Kaner, and B. H. Weiller, "Polyaniline nanofiber gas sensors: Examination of response mechanisms," *Nano Lett*, vol. 4, pp. 491–496, 2004.

[44] H. Q. Liu, J. Kameoka, D. A. Czaplewski, and H. G. Craighead, "Polymeric nanowire chemical sensor," *Nano Lett*, vol. 4, pp. 671–675, 2004.

[45] S. Sharma, C. Nirkhe, S. Pethkar, and A. A. Athawale, "Chloroform vapour sensor based on copper/polyaniline nanocomposite," *Sensor Actuat B-Chem*, vol. 85, pp. 131–136, 2002.

[46] K. Domansky, D. L. Baldwin, J. W. Grate, T. B. Hall, J. Li, M. Josowicz, and J. Janata, "Development and calibration of field-effect transistor-based sensor array for measurement of hydrogen and ammonia gas mixtures in humid air," *Anal Chem*, vol. 70, pp. 473–481, 1998.

[47] H. S. Li, M. Josowicz, D. R. Baer, M. H. Engelhard, and J. Janata, "Preparation and characterization of polyaniline-palladium composite films," *J Electrochem Soc*, vol. 142, pp. 798–805, 1995.

[48] J. Janata and M. Josowicz, "Chemical modulation of work function as a transduction mechanism for chemical sensors," *Accounts Chem Res*, vol. 31, pp. 241–248, 1998.

[49] J. Li, D. Petelenz, and J. Janata, "Suspended gate field-effect transistor sensitive to gaseous-hydrogen cyanide," *Electroanal*, vol. 5, pp. 791–794, 1993.

[50] E. W. Paul, A. J. Ricco, and M. S. Wrighton, "Resistance of polyaniline films as a function of electrochemical potential and the fabrication of polyaniline-based microelectronic devices," *J Phys Chem*, vol. 89, pp. 1441–1447, 1985.

[51] K. Persaud and G. Dodd, "Analysis of discrimination mechanisms in the mammalian olfactory system using a model nose," *Nature*, vol. 299, pp. 352–355, 1982.

[52] J. W. Gardner and W. E. Gardner, "The role of the electronic nose in condition monitoring," *Insight*, vol. 39, pp. 865–869, 1997.

[53] B. L. Smith and A. Glezer, "The formation and evolution of synthetic jets," *Physics of fluids*, vol. 10, pp. 2281–2297, 1998.

[54] A. Glezer and M. Amitay, "Synthetic jets," *Annu Rev Fluid Mech*, vol. 34, pp. 503–529, 2002.

[55] D. J. Coe, M. G. Allen, B. L. Smith, and A. Glezer, "Addressable micromachined jet arrays," in *TRANSDUCERS '95*, Stockholm, Sweden, 1995.

[56] B. R. Munson, D. F. Young, and T. H. Okiishi, *Fundamentals of fluid mechanics*. New York: Wiley, 2002.

[57] J. Li, J. Janata, and M. Josowicz, "Application of poly(cyclophosphazene) for potentiometric detection of tributyl phosphate vapor," *Electroanal*, vol. 8, pp. 778–783, 1996.

[58] J. X. Huang, S. Virji, B. H. Weiller, and R. B. Kaner, "Polyaniline nanofibers: Facile synthesis and chemical sensors," *J Am Chem Soc*, vol. 125, pp. 314–315, 2003.

[59] R. C. Patil, S. F. Patil, I. S. Mulla, and K. Vijayamohanan, "Effect of protonation media on chemically and electrochemically synthesized polyaniline," *Polym Int*, vol. 49, pp. 189–196, 2000.

[60] G. F. Li, C. Martinez, J. Janata, J. A. Smith, M. Josowicz, and S. Semancik, "Effect of morphology on the response of polyaniline-based conductometric gas sensors: Nanofibers vs. thin films," *Electrochem Solid St*, vol. 7, pp. H44–H47, 2004.

[61] I. Sasaki, J. Janata, and A. Glezer, "Fast sensing, sampling gas system using integrated synthetic jet actuators," *IEEE Sensors Journal, submitted*.

[62] F. L'Hereec, H. Chen, Z. P. Zhou, and J. Janata, "New platform for testing candidate materials for organic field-effect transistors," *J Phys Chem B*, vol. 108, pp. 9042–9047, 2004.

[63] I. Sasaki, M. Josowicz, and J. Janata, "Photo-induced stabilization of polyaniline matrix for gas sensor applications," *Chem Mater, submitted*.

[64] D. Pede, G. Serra, and D. De Rossi, "Microfabrication of conducting polymer devices by ink-jet stereolithography," *Mat Sci Eng C-Bio S*, vol. 5, pp. 289–291, 1998.

[65] J. Li, J. Janata, and M. Josowicz, "Application of poly(cyclophosphazene) for potentiometric detection of tributyl phosphate vapor," *Electroanal*, vol. 8, pp. 778–783, 1996.

[66] J. A. Smith, M. Josowicz, and J. Janata, "Gold-polyaniline composite - part i. moving electrochemical interface," *Phys Chem Chem Phys*, vol. 7, pp. 3614–3618, 2005.

[67] J. A. Smith, M. Josowicz, M. Engelhard, D. R. Baer, and J. Janata, "Gold-polyaniline composites - part ii. effects of nanometer sized particles," *Phys Chem Chem Phys*, vol. 7, pp. 3619–3625, 2005.

[68] J. M. Kinyanjui, J. Hanks, D. W. Hatchett, A. Smith, and M. Josowicz, "Chemical and electrochemical synthesis of polyaniline/gold composites," *J Electrochem Soc*, vol. 151, pp. D113–D120, 2004.

[69] J. M. Kinyanjui, D. W. Hatchett, J. A. Smith, and M. Josowicz, "Chemical synthesis of a polyaniline/gold composite using tetrachloroaurate," *Chem Mater*, vol. 16, pp. 3390–3398, 2004.

[70] H. Chen, *Thesis*, 2005.